

DECOMPOSITION OF THE SEISMIC SOURCE USING NUMERICAL SIMULATIONS AND OBSERVATIONS OF NUCLEAR EXPLOSIONS

Jeffrey L. Stevens, et al.

**Leidos
10260 Campus Point Drive
San Diego, CA 92121**

31 May 2017

Final Report

APPROVED FOR PUBLIC RELEASE; DISTRIBUTION IS UNLIMITED.



**AIR FORCE RESEARCH LABORATORY
Space Vehicles Directorate
3550 Aberdeen Ave SE
AIR FORCE MATERIEL COMMAND
KIRTLAND AIR FORCE BASE, NM 87117-5776**

DTIC COPY

NOTICE AND SIGNATURE PAGE

Using Government drawings, specifications, or other data included in this document for any purpose other than Government procurement does not in any way obligate the U.S. Government. The fact that the Government formulated or supplied the drawings, specifications, or other data does not license the holder or any other person or corporation; or convey any rights or permission to manufacture, use, or sell any patented invention that may relate to them.

This report was cleared for public release by the RD/RV Communications Office and is available to the general public, including foreign nationals. Copies may be obtained from the Defense Technical Information Center (DTIC) (<http://www.dtic.mil>).

AFRL-RV-PS-TR-2017-0120 HAS BEEN REVIEWED AND IS APPROVED FOR PUBLICATION IN ACCORDANCE WITH ASSIGNED DISTRIBUTION STATEMENT.

//SIGNED//

Dr. Frederick Schult
Program Manager, AFRL/RVBYE

//SIGNED//

Dr. Thomas R. Caudill, Acting Chief
AFRL Battlespace Environment Division

This report is published in the interest of scientific and technical information exchange, and its publication does not constitute the Government's approval or disapproval of its ideas or findings.

REPORT DOCUMENTATION PAGE			Form Approved OMB No. 0704-0188	
Public reporting burden for this collection of information is estimated to average 1 hour per response, including the time for reviewing instructions, searching existing data sources, gathering and maintaining the data needed, and completing and reviewing this collection of information. Send comments regarding this burden estimate or any other aspect of this collection of information, including suggestions for reducing this burden to Department of Defense, Washington Headquarters Services, Directorate for Information Operations and Reports (0704-0188), 1215 Jefferson Davis Highway, Suite 1204, Arlington, VA 22202-4302. Respondents should be aware that notwithstanding any other provision of law, no person shall be subject to any penalty for failing to comply with a collection of information if it does not display a currently valid OMB control number. PLEASE DO NOT RETURN YOUR FORM TO THE ABOVE ADDRESS.				
1. REPORT DATE (DD-MM-YYYY) 31-05-2017		2. REPORT TYPE Final Report		3. DATES COVERED (From - To) 01 May 2014 – 30 Apr 2017
4. TITLE AND SUBTITLE Decomposition of the Seismic Source Using Numerical Simulations and Observations of Nuclear Explosions			5a. CONTRACT NUMBER FA9453-14-C-0257	
			5b. GRANT NUMBER	
			5c. PROGRAM ELEMENT NUMBER 62601F	
6. AUTHOR(S) Jeffrey L. Stevens, Michael O'Brien, and Thomas W. Thompson			5d. PROJECT NUMBER 1010	
			5e. TASK NUMBER PPM00016522	
			5f. WORK UNIT NUMBER EF127002	
7. PERFORMING ORGANIZATION NAME(S) AND ADDRESS(ES) Leidos 10260 Campus Point Drive San Diego, CA 92121			8. PERFORMING ORGANIZATION REPORT NUMBER	
9. SPONSORING / MONITORING AGENCY NAME(S) AND ADDRESS(ES) Air Force Research Laboratory Space Vehicles Directorate 3550 Aberdeen Avenue SE Kirtland AFB, NM 87117-5776			10. SPONSOR/MONITOR'S ACRONYM(S) AFRL/RVBYE	
			11. SPONSOR/MONITOR'S REPORT NUMBER(S) AFRL-RV-PS-TR-2017-0120	
12. DISTRIBUTION / AVAILABILITY STATEMENT Approved for public release; distribution is unlimited. (RDMX-17-13576 dtd 20 Mar 2018)				
13. SUPPLEMENTARY NOTES				
14. ABSTRACT We investigate the effects of explosion depth, tectonic stresses and topography on seismic waves from underground nuclear explosions. We perform three-dimensional calculations for an explosion inside and under a mountain, and then perform four three-dimensional calculations of an explosion at several depths in the topography of the North Korean test site. We also perform a large number of two-dimensional axisymmetric calculations of explosions at depths from 150 to 1000 meters in four earth structures, with compressive and tensile tectonic stresses and with no tectonic stresses. We find that P-waves are not strongly affected by any of these effects because the initial downgoing P-wave is unaffected by interaction with the free surface. Surface waves, however, are strongly affected by all of these effects. There is an optimal depth where surface waves are maximized at the base of a mountain and at or slightly below normal containment depth. At deeper depths, increasing overburden pressure reduces the surface waves. At shallower depths, interaction with the free surface reduces the surface waves. For explosions inside a mountain, displacement of the sides of the mountain reduces surface waves. Compressive prestress reduces surface wave substantially, while tensile prestress increases surface waves. The North Korean explosions appear to be at an optimal depth, in a region of extension, and beneath a mountain, all of which increase surface wave amplitudes. Measurements of Ms from Degelen and Shagan River explosions as small as 1.5 kilotons are consistent with the global average Ms:yield curve, while the North Korean explosions are high by about 0.6 magnitude units.				
15. SUBJECT TERMS nonlinear finite element calculations, nuclear explosion monitoring, topography				
16. SECURITY CLASSIFICATION OF:			17. LIMITATION OF ABSTRACT Unlimited	18. NUMBER OF PAGES 112
a. REPORT Unclassified	b. ABSTRACT Unclassified	c. THIS PAGE Unclassified		
				19b. TELEPHONE NUMBER (include area code)

This page is intentionally left blank.

Table of Contents

1. Summary	1
2. Introduction and Summary	2
3. Technical Approach	5
3.1. The CRAM3D Code	5
3.2. Propagation with the Elastodynamic Representation Theorem	5
3.3. Tectonic Prestress	6
3.4 Topography	6
3.5 Small Explosion Data Set	8
4. Results and Discussion	9
4.1 Analysis of Small Explosions	9
4.2 Numerical Modeling of Seismic Waves from Explosions Beneath a Sloping Surface	12
4.2.1 Results	14
4.2.2 Near Field Motion and Deformation	15
4.2.3 Regional Waveforms	19
4.2.4 Surface waves	23
4.2.5 Body waves	27
4.3 Decomposition of the Seismic Source of Surface Waves in 3D Calculations	30
4.4 Numerical Modeling of Seismic Waves from Explosions at the North Korea Nuclear Test Site	32
4.4.1 Results	35
4.4.2 Near Field Motion and Deformation	36
4.4.3 Regional Waveforms	48
4.4.4 Surface Waves	54
4.4.5 Body Waves	61
4.5 Decomposition of the Seismic Source	65
4.5.1 Earth model with prestress	67
4.5.2 Near field nonlinear deformation	67
4.5.3 Near field nonlinear deformation in a tectonic stress field	70
4.5.4 Propagation using the representation theorem	74
4.5.5 Surface wave results	75
4.5.6 Full Wave Regional Waveforms	82
4.5.7 Far-field Body Waves	86
4.5.8 Conclusions from Seismic Source Decomposition Analysis	90
5. Improvements to CRAM3D Codes	91
6. Conclusions	93
References	95
Appendix-CRAM3D Update and Deliverable	97

List of Figures and Tables

List of Figures

Figure 1. Data set of new measurements together with North Korean events.....	2
Figure 2. Ms-log(Yield) vs. scaled depth.....	2
Figure 3. Ms from axisymmetric calculations in Degelen structure.....	3
Figure 4. Ms from axisymmetric calculations in Shoal structure.....	3
Figure 5. Ms-log(yield) vs. scaled depth for 1D and 3D North Korea calculations.....	4
Figure 6. The CRAM 3D finite element outer grid (left) is rectangular.....	5
Figure 7. Stress regimes vary by region.....	6
Figure 8. From left to right, vertical, eastward and northward displacements caused by topography along a slice 204 meters from the NPE shot point.....	7
Figure 9. Ms vs. Yield for small Semipalatinsk explosions.....	9
Figure 10. Ms vs. Yield for a global data set of explosions from Stevens and Murphy (2001).....	9
Figure 11. Data set of new measurements together with North Korean events.....	10
Figure 12. Ms:mb for small Semipalatinsk and North Korean events.....	10
Figure 13. Left: mb:Yield for small Semi events. Right: mb:Yield with North Korean events.....	11
Figure 14. Left: Ms-log(yield) vs. depth. Right: Ms-log(yield) vs. scaled depth.....	11
Figure 15. Top: Elevation in map view and cross section for the slope calculation.....	12
Figure 16. Shoal calculation. Top row: vertical velocity at 0.1 s (left), vertical velocity at 0.2 s (right). Bottom row: final plastic work (left), final crack strains (right).....	15
Figure 17. Slope 1 calculation. Top row: vertical velocity at 0.1 s (left), vertical velocity at 0.2 s (right). Bottom row: final plastic work (left), final crack strains (right).....	15
Figure 18. Slope 2 calculation. Top row: vertical velocity at 0.1 s (left), vertical velocity at 0.2 s (right). Bottom row: final plastic work (left), final crack strains (right).....	16
Figure 19. Slope 3 calculation. Top row: vertical velocity at 0.1 s (left), vertical velocity at 0.2 s (right). Bottom row: final plastic work (left), final crack strains (right).....	16
Figure 20. Left: vertical velocity at 0.1 seconds for the four runs. Right: vertical velocity at 0.2 second for the four runs. From top to bottom: Shoal, Slope 1, Slope 2, Slope 3..	17
Figure 21. Left: Final plastic work for the four runs. Right: Final crack strains for the four runs. From top to bottom: Shoal, Slope 1, Slope 2, Slope 3.....	18
Figure 22. Regional waveforms at 250 km from the Shoal calculation (top) and Slope 1 calculation (bottom).....	19
Figure 23. Full waveforms at 250 km from the Slope 1 calculation. Left: vertical in 3 directions. Right: Tangential in 3 directions and diagram of direction. (Tangential at 90 degrees is zero).....	20
Figure 24. Full waveforms at 250 km from the Slope 2 calculation. Left: vertical in 3 directions. Right: Tangential in 3 directions and diagram of direction.....	21
Figure 25. Full waveforms at 250 km from the Slope 3 calculation. Left: vertical in 3 directions. Right: Tangential in 3 directions and diagram of direction.....	22
Figure 26. Long period surface waves at 2000 km from the Shoal calculation (top) and Slope 1 calculation (bottom).....	23
Figure 27. Surface waves at 2000 km for the Slope 1 calculation.....	24

Figure 28. Surface waves at 2000 km for the Slope 2 calculation.....	25
Figure 29. Surface waves at 2000 km for the Slope 3 calculation.....	26
Figure 30. Slope 1 P, together with Shoal calculation with no prestress and with compressive and tensile prestress.....	27
Figure 31. Slope 1 SV.....	27
Figure 32. Slope 1 SH.....	27
Figure 33. Slope 2 P.....	28
Figure 34. Slope 2 SV.....	28
Figure 35. Slope 2 SH.....	28
Figure 36. Slope 3 P (Note – this is a 50 kt explosion compared to a 12.5 kt explosion)	29
Figure 37. Slope 3 SV.....	29
Figure 38. Slope 3 SH.....	29
Figure 39. Green’s function stresses for generation of a vertical component Rayleigh wave (third index) in the direction of the X (left) and Y (right) axes at 20 seconds period.....	30
Figure 40. Horizontal displacements normal to the monitoring surface vs. depth for three calculations. Left: back side of the calculation (across mountain). Right: left side of calculation (along mountain).....	31
Figure 41. Topography near the North Korea test site.....	34
Figure 42. South-to-north profiles (through the source) of vertical velocity from 12.5 kt explosion simulations at four depths (100m, 200m, 540m, 800m respectively from the top) under sloping topography at the North Korea test site and the flat Shoal simulation (bottom): Left at 0.1 sec, right at 1.5 seconds.	36
Figure 43. South-to-north profiles (through the source) of log-magnitude of velocity from 12.5 kt explosion simulations at four depths (100m, 200m, 540m, 800m respectively from the top) under sloping topography at the North Korea test site and the flat Shoal simulation (bottom): Left at 0.1 sec, right at 1.5 seconds.....	37
Figure 44. West-to-east profiles (through the source) of vertical velocity (right) and log- magnitude of velocity (left) at 0.2 sec. from 12.5 kt explosion simulations at four depths (100m, 200m, 540m, 800m respectively from the top) under sloping topography at the North Korea test site and the flat Shoal simulation (bottom).....	38
Figure 45. South-to-north profiles (through the source) of plastic work (energy of nonlinear yielding) from 12.5 kt explosion simulations at four depths (100m, 200m, 540m, 800m respectively from the top) under sloping topography at the North Korea test site, and the Shoal simulation (bottom): Left at 0.1 sec, right at 1.5 seconds.....	39
Figure 46. South-to-north profiles (through the source) of crack strain from 12.5 kt explosion simulations at four depths (100m, 200m, 540m, 800m respectively from the top) under sloping topography at the North Korea test site and the Shoal simulation (bottom): Left at 0.1 sec, right at 1.5 sec.	41
Figure 47. Outward displacement on the west monitoring surface at $d_{east} = -1500\text{m}$ from the source for the 3-D simulations of explosions at the North Korea test site with source depths (from top to bottom) of 100, 200, 540, and 800 m.	43
Figure 48. Outward displacement on the east monitoring surface at $d_{east} = 1500\text{m}$ from the source for the 3-D simulations of explosions at the North Korea test site with source depths (from top to bottom) of 100, 200, 540, and 800 m.	44

Figure 49. Outward displacement on the north monitoring surface at $d_{east} = 1500\text{m}$ from the source for the 3-D simulations of explosions at the North Korea test site with source depths (from top to bottom) of 100, 200, 540, and 800 m.....	45
Figure 50. Outward displacement on the south monitoring surface at $d_{north} = -1400\text{m}$ from the source for the 3-D simulations of explosions at the North Korea test site with source depths (from top to bottom) of 100, 200, 540, and 800 m.....	46
Figure 51. Profiles of final outward normal displacement on the monitoring surface faces due west, east, south, and north of the North Korea simulation sources.....	47
Figure 52. Full-waveform radial velocity at 250 km and azimuths of 0, -45, -90, -135 and -180 degrees from the North Korea simulations with source depths of 100, 200, 540 and 800m (red) and the Shoal simulations at 367 m below a flat surface (blue).....	49
Figure 53. Full-waveform vertical velocity at 250 km and azimuths of 0, -45, -90 -135 and -180 degrees from the North Korea simulations with source depths of 100, 200, 540 and 800m (red) and the Shoal simulations at 367 m below a flat surface (blue).....	50
Figure 54. Full-waveform tangential velocity at 250 km and azimuths of 0, -45, -90 -135 and -180 degrees from the North Korea simulations with source depths of 100, 200, 540 and 800m (red) and the Shoal simulations at 367 m below a flat surface (blue).....	51
Figure 55. Full-waveform vertical velocity at 250 km and azimuths of 0, -45, -90 -135 and -180 degrees from the North Korea simulations with source depths of 100, 200, 540 and 800m (red) and the Shoal simulations at 367 m below a flat surface (blue).....	52
Figure 56. Full-waveform vertical velocity at 250 km and azimuths of 0, -45, -90 -135 and -180 degrees from the North Korea simulations with source depths of 100, 200, 540 and 800m (red) and the Shoal simulations at 367 m below a flat surface (blue).....	53
Figure 57. Left: M_s vs depth for calculated surface waves. Right: M_s -log(yield) vs. scaled depth.....	54
Figure 58. Surface wave radial velocity at 2000km.....	55
Figure 59. Surface wave tangential velocity at 2000km.....	56
Figure 60. Surface wave vertical velocity at 2000km.....	57
Figure 61. Surface wave radial velocity at 2000km, low-pass filtered at 15 sec.....	58
Figure 62. Surface wave tangential velocity at 2000km, low-pass filtered at 15 sec....	59
Figure 63. Surface wave vertical velocity at 2000km, low-pass filtered at 15 sec.....	60
Figure 64. Far-field P-wave at 1000km for Shoal and North Korea simulations.....	62
Figure 65. Far-field SH-wave at 1000km for Shoal and North Korea simulations.....	63
Figure 66. Far-field SV-wave at 1000km for Shoal and North Korea simulations.....	64
Figure 67. Explosions were calculated at the depths shown from 150m to 1000m (axisymmetry). Tectonic stresses were simulated by adding a radial tensile or compressive stress.....	65
Figure 68. Strength of materials used in this study. Right: expanded view of low pressure part of strength curves.....	66
Figure 69. Left: Pahute Mesa structure used in depth of burial study (Day et al, 1986) and used over a wider range of depth in the current study. Right: Load/Unload curves for the three layers.....	66
Figure 70. Left: tensile stress state corresponding to a state in balance with normal faulting with a coefficient of friction of 0.6. Right: compressive stress state in balance with thrust faulting with a coefficient of friction of 0.6.....	67

Figure 71. Region of nonlinear deformation for an explosion at 150 meters depth. Top left: Degelen; top right: Shoal; bottom left: Shagan; bottom right: Pahute. The Degelen explosion was 10 kt; the other three 12.5 kt.....	68
Figure 72. Region of nonlinear deformation for an explosion at 300 meters depth. Top left: Degelen; top right: Shoal; bottom left: Shagan; bottom right: Pahute.....	68
Figure 73. Region of nonlinear deformation for an explosion at 600 meters depth. Top left: Degelen; top right: Shoal; bottom left: Shagan; bottom right: Pahute.....	69
Figure 74. Region of nonlinear deformation for an explosion at 1000 meters depth. Top left: Degelen; top right: Shoal; bottom left: Shagan; bottom right: Pahute.....	69
Figure 75. Region of nonlinear deformation for an explosion in a prestress field at 150 meters depth. Left figures are tensile stress fields, right figures are compressive stress fields. Top row: Degelen; second row: Shoal; third row: Shagan; bottom row: Pahute	71
Figure 76. Region of nonlinear deformation for an explosion in a prestress field at 300 meters depth. Left figures are tensile stress fields, right figures are compressive stress fields. Top row: Degelen; second row: Shoal; third row: Shagan; bottom row: Pahute	72
Figure 77. Region of nonlinear deformation for an explosion in a prestress field at 600 meters depth. Left figures are tensile stress fields, right figures are compressive stress fields. Top row: Degelen; second row: Shoal; third row: Shagan; bottom row: Pahute	73
Figure 78. V_p and V_s vs. depth for the four structures used in the calculations.....	74
Figure 79. 20 second surface wave magnitudes from all axisymmetric and spherically symmetric calculations. Left: Degelen granite; Right: Climax stock granite.....	75
Figure 80. 20 second surface wave magnitudes from all axisymmetric and spherically symmetric calculations. Left: Shagan River granite; Right: Pahute Mesa Rhyolite.....	75
Figure 81. Surface waves for an explosion depth of 150 meters in four structures. Top left: Degelen, top right: Shoal, lower left: Shagan, lower right: Pahute.....	76
Figure 82. Surface waves for an explosion depth of 300 meters in four structures. Top left: Degelen, top right: Shoal, lower left: Shagan, lower right: Pahute.....	77
Figure 83. Final horizontal displacement at 200m depth. Left: tensile prestress. Center: no prestress. Right: compressive prestress. Top: Degelen; bottom: Shoal.....	78
Figure 84. Final horizontal displacement at 370m depth. Left: tensile prestress. Center: no prestress. Right: compressive prestress. Top: Degelen; bottom: Shoal.....	79
Figure 85. Final horizontal displacement at 800m depth. Left: tensile prestress. Center: no prestress. Right: compressive prestress. Top: Degelen; bottom: Shoal.....	80
Figure 86. Left: M_s from 1D and 2D “Hard” calculation. Middle: Hard model radial displacement. Right: Degelen Model radial displacement. Both for 150 meters depth...	80
Figure 87. Radial (left) and Vertical (right) displacement field difference between the Degelen and (scaled) Hard models for an explosion at 150 meters depth.....	81
Figure 88. Vectors of displacement difference. Left: Degelen at 150m depth. Right: Shoal at 250m depth.....	81
Figure 89. Example full waveform seismograms for the four earth models.....	82
Figure 90. P-wave amplitudes for each structure.....	83
Figure 91. S-wave amplitudes for each structure.....	84
Figure 92. L_g amplitudes for each structure.....	85
Figure 93. Far-field P and SV waves from 1D and 2D calculations at a depth of 250 meters in the four earth structures.....	86
Figure 94. Far field P-wave amplitudes for each structure.....	87

Figure 95. Far field SV-wave amplitudes for each structure.....	87
Figure 96. Same waveforms as Figure 93 lowpass filtered at 1 Hz.....	88
Figure 97. Far field P-wave amplitudes, low-pass filtered at 1 Hz, for each structure....	89
Figure 98. Far field SV-wave amplitudes, low-pass filtered at 1 Hz, for each structure.	89
Figure 99. Ms-log(Yield) vs. scaled depth. Left: Measurements from East Kazakh and North Korean Data. Right: Calculations for Degelen structure.....	90
Figure 100. Calculations for Shoal structure.....	91
Figure 101. The effects of a dynamically varied damping in reducing simulation time for attaining grid equilibrium.....	92

List of Tables

Table 1. Small Semipalatinsk events with measurable Ms at Borovoye.....	8
Table 2. Slope and Shoal calculations.....	12
Table 3. Earth model used to propagate Shoal and Slope calculations.....	13
Table 4. Summary of simulations of 12.5 kt explosions at North Korea test site.....	32
Table 5. Regional material model surrounding the North Korea test site.....	33

Acknowledgments

The facilities of IRIS Data Services, and specifically the IRIS Data Management Center, were used for access to waveforms, related metadata, and/or derived products used in this study. IRIS Data Services are funded through the Seismological Facilities for the Advancement of Geoscience and EarthScope (SAGE) Proposal of the National Science Foundation under Cooperative Agreement EAR-1261681

This page is intentionally left blank.

1. Summary

We investigate the effects of explosion depth, tectonic stresses and topography on seismic waves from underground nuclear explosions. We perform three-dimensional calculations for an explosion inside and under a mountain, and then perform four three-dimensional calculations of an explosion at several depths in the topography of the North Korean test site. We also perform a large number of two-dimensional axisymmetric calculations of explosions at depths from 150 to 1000 meters in four earth structures, with compressive and tensile tectonic stresses and with no tectonic stresses. We find that P-waves are not strongly affected by any of these effects because the initial downgoing P-wave is unaffected by interaction with the free surface. Surface waves, however, are strongly affected by all of these effects. There is an optimal depth where surface waves are maximized at the base of a mountain and at or slightly below normal containment depth. At deeper depths, increasing overburden pressure reduces the surface waves. At shallower depths, interaction with the free surface reduces the surface waves. For explosions inside a mountain, displacement of the sides of the mountain reduces surface waves. Compressive prestress reduces surface wave substantially, while tensile prestress increases surface waves. The North Korean explosions appear to be at an optimal depth, in a region of extension, and beneath a mountain, all of which increase surface wave amplitudes. Measurements of M_s from Degelen and Shagan River explosions as small as 1.5 kilotons are consistent with the global average M_s :yield curve, while the North Korean explosions are high by about 0.6 magnitude units.

An updated version of CRAM3D is delivered along with this report. The code has an improved procedure for bringing the grid into gravitational equilibrium, which is particularly important for calculations with topography.

2. Introduction and Summary

The objective of this project is to decompose the seismic source to determine which components of the source affect seismic signals. We perform 1D, 2D, and 3D simulations to identify the physical mechanisms operating during the explosion and affecting seismic signals. We focus the data analysis on surface waves from small (< 50 kt) events from hard rock areas in Eurasia. Based on the modeling and data comparison, we assess the importance of the components of the explosion source and their dependence on depth, material properties and tectonic environment, and determine the implications for discrimination and yield estimation.

We start with data analysis by measuring M_s from small explosions at the Semipalatinsk test site. The small event analysis is motivated by the observation that surface waves from the North Korean explosions were larger than expected for their estimated yields. However, these events were also smaller than most explosions in the global M_s :yield data set (e.g. Stevens and Murphy, 2001). A possible explanation for the anomalous yields is therefore that the M_s :yield curve has a non-unity slope for small explosions which would imply that M_s is generally larger for smaller events. We test this hypothesis by calculating M_s for explosions with yields as small as 1.4 kilotons. As shown in Figure 1 and Figure 2, M_s from these small events are very consistent with the global M_s : yield curve, while the North Korean surface waves are well above the curve.

We perform a large number of two-dimensional axisymmetric calculations of explosions over a range of depths from 150 to 1000 meters in four earth structures with and without tectonic stresses. We calculate surface waves, body waves and regional seismograms from all of these calculations. We assess the effects of depth, tectonic stress state and material properties on generation of seismic phases. As can be seen in Figure 3, the effect of the nonlinear interaction with the free surface is to reduce surface wave amplitudes for shallow explosions. Surface waves also decrease with increasing depth because of increasing overburden pressure, causing a peak

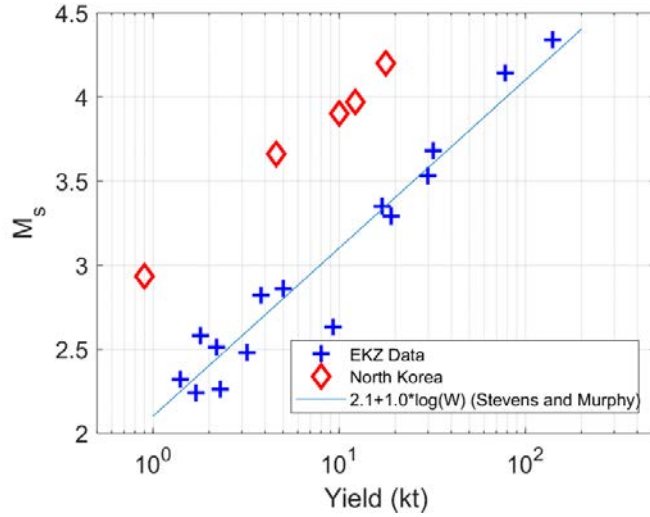


Figure 1. Data set of new measurements together with North Korean events.

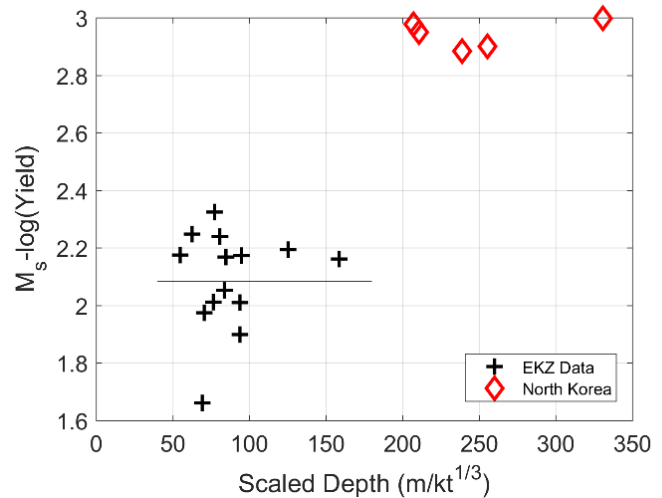


Figure 2. M_s -log(Yield) vs. scaled depth. Measurements from East Kazakh and North Korean Data.

amplitude at about $150 \text{ m/kt}^{1/3}$. Compressive tectonic stresses reduce, and sometimes reverse, surface wave amplitudes, while tensile tectonic stresses increase surface waves, although the effect is smaller. Also as can be seen by comparing Figure 2 with Figure 3, the new measurements from Semipalatinsk are very consistent with the Degelen calculations, particularly for a compressive stress state, while the North Korean surface waves are larger than predicted, even for a tensile tectonic stress state.

Figure 4 shows similar calculations for the Shoal material model and earth structure. Because it is a weaker granite model, the surface waves are about 0.2 magnitude units larger for the same yield, and at shallow depths in tectonic compression some of the surface waves are polarity-reversed.

We then look at the effects of topography by performing calculations of an explosion beneath a sloping surface on a mountainside. This topic is motivated by the fact that many explosions occur in mountainous areas, and a common way to ensure containment is to tunnel into the side of a mountain. This has occurred at North Korea, Novaya Zemlya, Degelen Mountain and other locations. What does the presence of the mountain do to the seismic waves generated by the explosion and to corresponding yield estimates? To address this problem, we perform three 3D calculations of an explosion beneath a steep slope. The first, Slope 1, is placed beneath the mountain; the second, Slope 2, is higher and inside the mountain; while the third, Slope 3, is inside the mountain with the yield increased by a factor of 4. All three are performed using the same earth structure previously used for calculations of Shoal (Stevens and Thompson, 2015), and the Shoal calculations provide a baseline reference model for this series of calculations. We find that surface waves from explosions inside the mountain are substantially reduced because of horizontal stress release by the sides of the mountain, however surface waves from explosions under the mountain are increased.

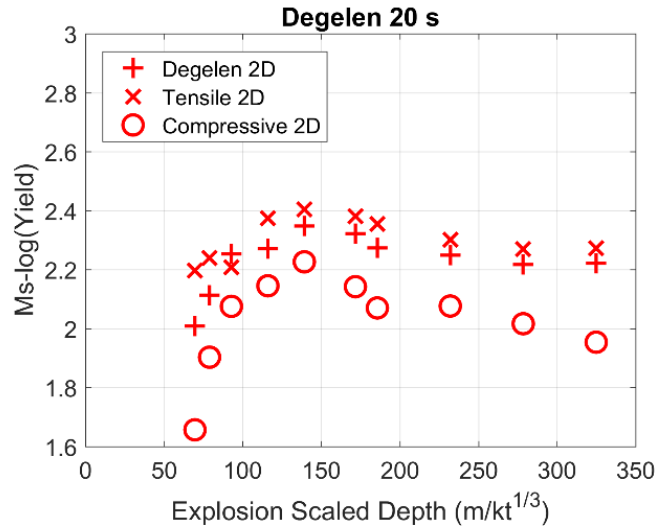


Figure 3. Ms from axisymmetric calculations in Degelen structure.

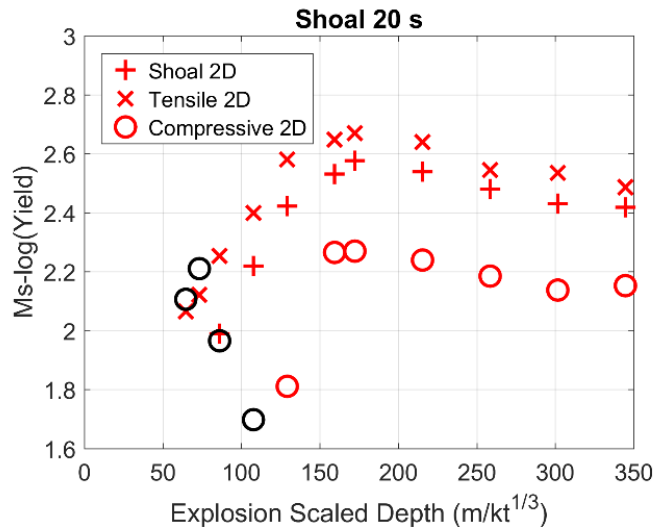


Figure 4. Ms from axisymmetric calculations in Shoal structure. *Black circles indicate polarity-reversed Rayleigh waves.*

We perform four large 3D calculations of explosions at the North Korean test site using the actual topography of the test site and at depths from 100 meters to 800 meters. Again we used the Shoal material model. As shown in Figure 5, the amplification of surface waves below the mountain is substantial, and in fact generates surface waves almost as large as those observed for North Korea. This effect is primarily due to the lower overburden pressure and reduced horizontal stresses caused by the mountain relative to the same depth in a flat layered medium. Comparing with Figure 4, the mountain base amplification effect with no tectonic stresses is larger than the plane-layered medium with tensile tectonic release, and in fact the physical mechanism is similar since both produce reduced pressure and reduced horizontal stresses.

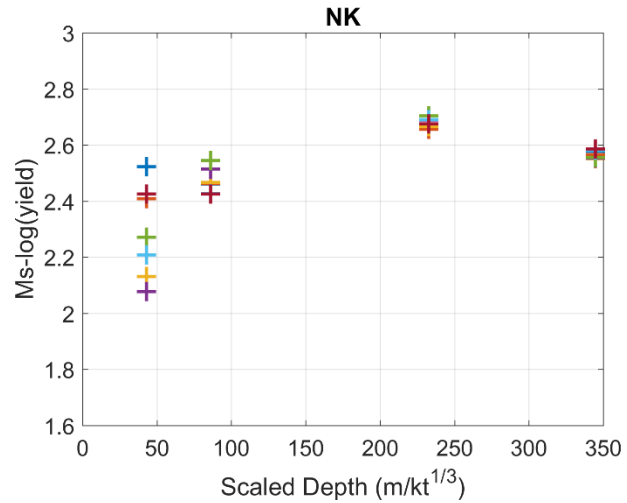


Figure 5. Ms-log(yield) vs. scaled depth for 3D North Korea calculations. *Compare with Figure 2. Multiple points at each depth correspond to different azimuths of observation. Surface waves from explosions inside the mountain are both reduced in amplitude and increased in variability, while surface waves from explosions beneath the mountain are amplified.*

3. Technical Approach

3.1. The CRAM3D Code

CRAM 3D is an explicit three-dimensional Lagrangian finite element code designed to run on multiple processors (Stevens et al, 2011, 2014a). For an explosion simulation, the cavity is placed near the center of the grid and is enclosed by a spider grid which facilitates applying the pressure boundary condition and rezoning elements (Figure 6). The well-tested nonlinear material models from CRAM 2D have been implemented in CRAM 3D. The code includes gravity and so includes the important effects that result from variation of overburden pressure with depth. Gravitational equilibrium is established by running an initial calculation with no source, followed by a second calculation including the explosion source. CRAM3D also has the capability to include tectonic prestress in the calculations.

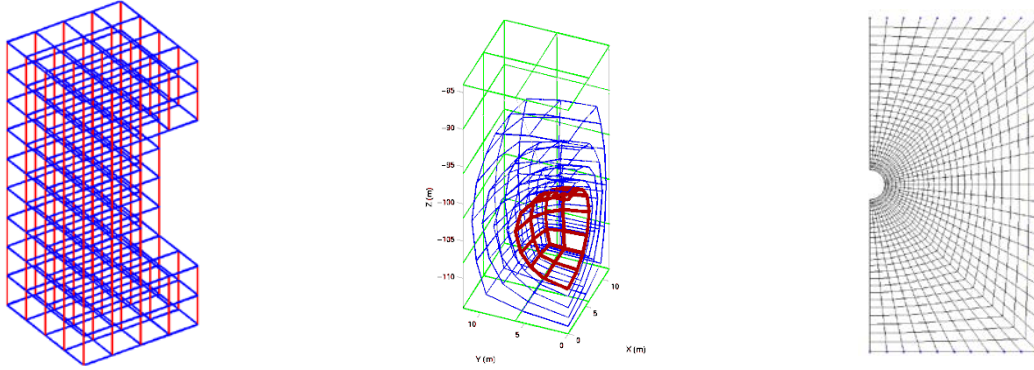


Figure 6. The CRAM 3D finite element outer grid (left) is rectangular. *The inner grid (center) is shaped to match the shape of the explosion shock wave. CRAM2D uses a similar axisymmetric spider grid (right) in the region around the explosion.*

3.2. Propagation with the Elastodynamic Representation Theorem

The representation theorem allows us to perform arbitrarily complex nonlinear calculations in the source region, and then propagate them with an appropriate Green's function. The representation theorem is exact. That is, no matter how complex the 3D motion is on the source region boundary, it will be correctly propagated by the representation theorem. The only exception is that it will not calculate the interaction of backscattered waves reflected from outside the source region with complexities of the source region.

In the three-dimensional numerical finite difference calculations, we save displacements and stresses due to the seismic source on a monitoring surface on the boundary of a rectangle (5 planar surfaces, excluding the upper surface), and calculate Green's functions from each point on the monitoring surface to the receiver and so the synthetic seismogram at the receiver point X outside of the monitoring surface is obtained by integrating over the monitoring surface S_M

$$u_i(X) = \int_{S_M} \left\{ G_j^i(\xi; X) * T_j^M(\xi) - u_j^M(\xi) * S_{jk}^i(\xi; X) n_k \right\} dA$$

in the frequency domain, where $G_j^i(\xi; X)$ and $S_{jk}^i(\xi; X)$ are the Green's function and the stress tensor on the monitoring surface due to a unit impulsive force at X in direction i , T_j^M is the traction on the monitoring surface due to the seismic source, u is the displacement on the monitoring surface, and n is the normal to the monitoring surface. The operator $*$ denotes convolution and the summation convention is assumed.

We use a plane-layered Green's function outside the source region. The Green's functions for the complete seismograms are derived from an algorithm based on the work of Luco and Apsel (1983) and Apsel and Luco (1983). The technique used for surface waves is similar to the method of Bache et al. (1982). The Green's functions for body waves are generated by a procedure similar to that described by Bache and Harkrider (1976) using a saddle point approximation to calculate a far-field plane wave for a given takeoff angle from a source in a plane-layered medium. Although the full waveform Green's functions generate the complete waveform, the other Green's functions provide additional insight into the source and waveform generation.

3.3. Tectonic Prestress

Performing a calculation of tectonic release requires an estimate of the stress state in the earth. While the stress state varies between regions, considerable work has also been done on this subject (e.g., Zoback, 2010). In general the vertical stress is equal to the overburden weight of the material above at any given point. The horizontal stresses may be larger or smaller than this value up to the point where failure due to frictional sliding or rock fracturing relieves the stress. In most of the world tectonic stresses are applied continuously, and so the prestress is in general close to equilibrium with frictional sliding. The ratio of maximum to minimum principal stress, both reduced by pore pressure, is given by

$\left[\mu + (\mu^2 + 1)^{\frac{1}{2}} \right]^2$ where μ is the coefficient of friction. For a typical coefficient of friction of

0.6, this ratio is 3.1, so the difference between principal stresses can be substantial and the effect on seismic waves potentially large. In our calculations, we calculate the overburden weight to determine the vertical stress, and then modify the horizontal stresses to some fraction of the frictional limit. This is the initial stable state of the calculation prior to introduction of the explosion. Note that although the vertical stress is still equivalent to the overburden weight, the pressure is not, and it may be either increased or reduced by the tectonic stresses. Since material strength increases with pressure, this also can substantially affect the seismic source. In general, normal faulting regimes will amplify seismic signals, while reverse faulting regimes will decrease seismic signals; strike-slip regimes could do either (Figure 7).

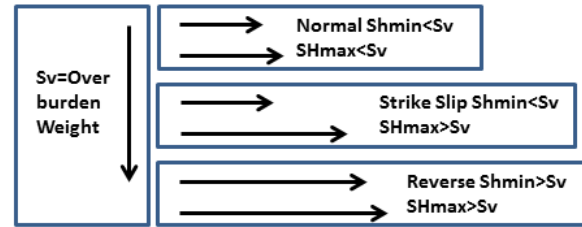


Figure 7 Stress regimes vary by region. *Horizontal stresses may be substantially larger or smaller than the vertical stress.*

3.4 Topography

CRAM3D incorporates topography by gradually distributing offsets of the grid from top to bottom so that change in cell dimensions is gradual rather than abrupt at the surface. The main difficulty in implementing topography is establishing gravitational equilibrium. The variation in overburden pressure with depth is very important in nonlinear calculations because strength is pressure

dependent and so material becomes much weaker at shallow depths. Because of this we need to bring the grid into gravitational equilibrium before running an explosion calculation. As mentioned above, this is done by starting with an approximate solution for overburden pressure in the grid and then running an initial calculation without the explosion. While this can be accomplished relatively easily for a plane-layered structure, bringing the grid to gravitational equilibrium in a structure with significant topography is much more difficult. While the calculation will eventually come to equilibrium, adding topography is the equivalent of dropping a mountain onto the free surface, and so it can take quite a long time to come to equilibrium.

The calculated displacements caused by topography close to the NPE calculation (Stevens et al, 2014a) are shown in Figure 8.

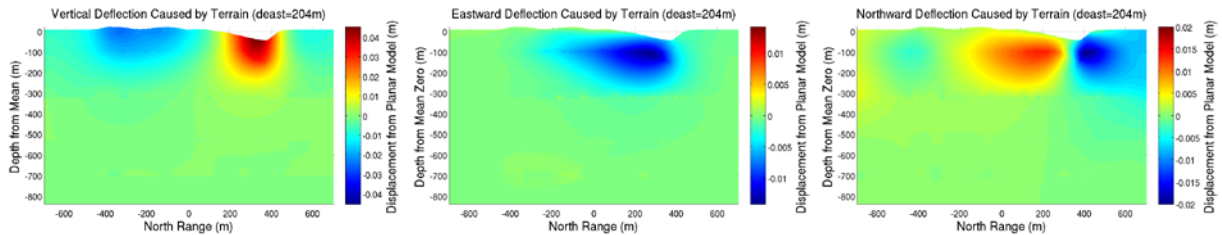


Figure 8. From left to right, vertical, eastward and northward displacements caused by topography along a slice 204 meters from the NPE shot point.

During this project we have made three significant improvements to calculations with topography that greatly improve the speed of the equilibrium run and also improve the stability of equilibrium in the restart run. The first improvement is to separate the equilibrium run into two stages. In the first stage we freeze the inner grid and let the outer grid come to approximate equilibrium first. This speeds up the equilibrium run dramatically because the time step for each cycle is then determined by the minimum grid size in the outer grid, which is much larger than the small zones near the cavity in the inner grid. In the second stage, we release the inner grid and let it come to equilibrium with the outer grid. The time step in the second stage is much shorter, but the outer grid is already close to equilibrium.

The second improvement is to save the body forces on the bottom and sides of the grid at the end of the equilibrium run and then to apply these body forces in the restart run. This guarantees that the equilibrium state will be maintained. Previously a more approximate solution was used to stabilize the grid, but in the project we are modeling much larger topographic variations, so the approximate solution was no longer adequate.

The third improvement is to use a starting model that is much closer to equilibrium. See section 5.1 for a description.

3.5 Small Explosion Data Set

We acquired data from the Borovoye station for 15 Semipalatinsk nuclear tests. We used Russell's (Russell, 2006) technique to measure M_s . Table 1 lists the parameters of these events together with the measured M_s at 10 seconds and the maximum and minimum M_s measured over the recoverable frequency band. The best quality data was near 10s period.

Table 1. Small Semipalatinsk events with measurable M_s at Borovoye.

Event	Date	Time	Yield (kt)	Lat	Lon	mb	Depth (m)	Instrument	M_s (10 s)	M_s (max)	M_s (min)
STS_414	12/16/1974	6:23:00	3.8	49.768	78.082	4.94	126	DS(8-15)	2.82	2.94	2.63
STS_482	3/26/1978	3:57:00	30	49.762	77.983	5.69	260	DS(8-25)	3.53	3.61	3.38
STS_555	9/25/1980	6:21:13	2.2	49.783	78.081	4.83	110	DS(8-13)	2.51	2.64	2.31
STS_574	7/17/1981	2:37:18	9.3	49.801	78.131	5.07	146	DS(8-11)	2.63	2.75	2.59
STS_605	12/25/1982	4:23:08	1.7	49.781	78.035	4.47	112	DS(8-25)	2.24	2.43	2.16
STS_650	10/18/1984	4:57:08	1.4	49.729	78.086	4.25	106	DS(9-15)	2.32	2.33	2.23
STS_676	5/6/1987	4:02:08	32	49.776	78.012	5.6	174	SKD(8-25)	3.68	3.69	3.42
STS_680	7/17/1987	1:17:09	78	49.776	78.020	5.8	267	SKD(8-25)	4.14	4.18	4.08
STS_690	12/20/1987	2:55:09	3.2	49.776	78.012	4.8	104	DS(8-13)	2.48	2.64	2.41
STS_695	4/22/1988	9:30:09	2.3	49.790	78.107	4.9	124	DS(10-13)	2.26	2.28	2.18
STS_698	6/14/1988	2:27:09	5	50.019	78.961	4.8	271	DS(8-25)	2.86	2.92	2.83
STS_701	9/14/1988	4:00:00	140	49.878	78.823	6.03	651	DS(8-25)	4.34	4.42	4.30
STS_703	11/12/1988	3:30:06	17	50.043	78.969	5.24	0	DS(8-25)	3.35	3.43	3.29
STS_704	11/23/1988	3:57:09	19	49.779	78.037	5.4	204	DS(9-16)	3.29	3.30	3.24
STS_713	10/4/1989	11:29:57	1.8	49.748	78.009	4.6	94	DS(8-16)	2.58	2.70	2.40

4. Results and Discussion

4.1 Analysis of Small Explosions

As discussed in the previous section, we measured M_s from Semipalatinsk explosions with yields as low as 1.4 kilotons. The motivation for this was to see if the slope of the M_s :yield curve changed significantly for small explosions. The results show that at least for this data set, it does not (Figure 9) and in fact M_s for these events is remarkably consistent with the global data set (Figure 10).

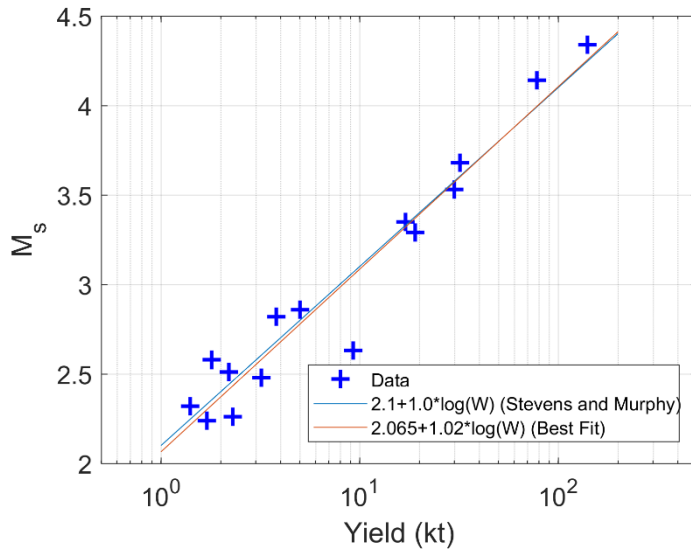


Figure 9. M_s vs. Yield for small Semipalatinsk explosions.

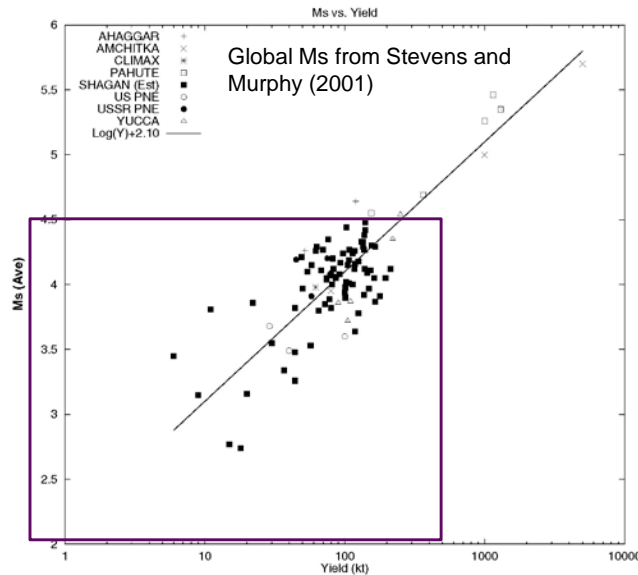


Figure 10. M_s vs. Yield for a global data set of explosions from Stevens and Murphy (2001). *The box shows the area of the new measurements in Figure 9.*

In contrast, the M_s :yield relation of the North Korean events is very different. Figure 11 shows the five North Korean nuclear tests on the same plot with the small Semipalatinsk events. Here we have used the yield estimates from Murphy et al (2013). M_s for the North Korean events is almost

a full magnitude larger at the same yield compared to this new data set. Ms:mb shows a similar anomaly (Figure 12).

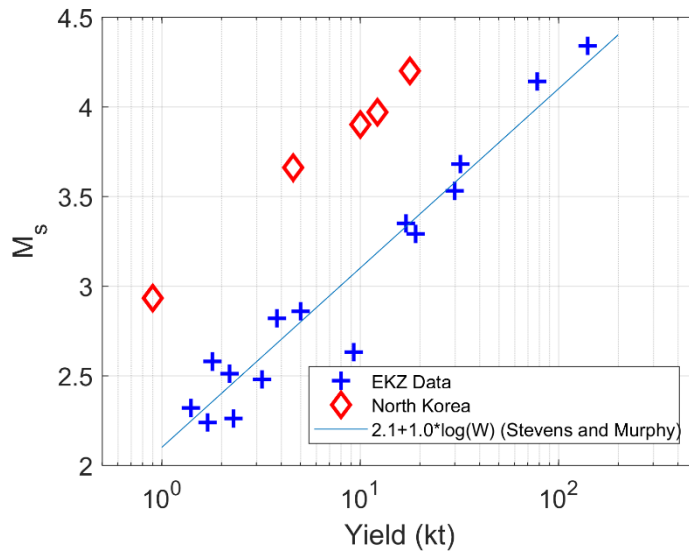


Figure 11. Data set of new measurements together with North Korean events.

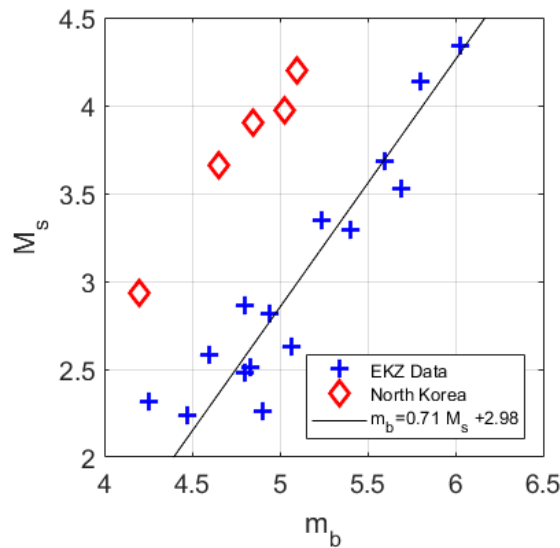


Figure 12. Ms:mb for small Semipalatinsk and North Korean events.

Figure 13 shows mb:yield for the small Semipalatinsk events together with the best fit mb:yield curve, which is very close to the mb:yield curve from Murphy (1995). There is no mb anomaly comparable to the Ms anomaly, although we should state that the yield estimates are derived from mb and we have no independent confirmation of yields. Figure 14 shows Ms-log(yield) vs. depth and scaled depth and there is no apparent dependence on either. Again, the North Korean events are very different.

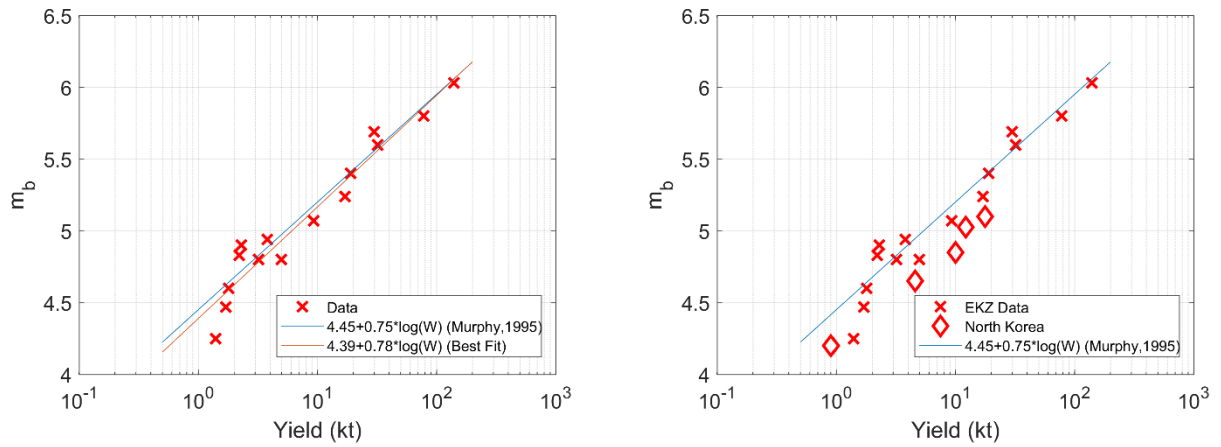


Figure 13. Left: m_b :Yield for small Semi events. Right: m_b :Yield with North Korean events.

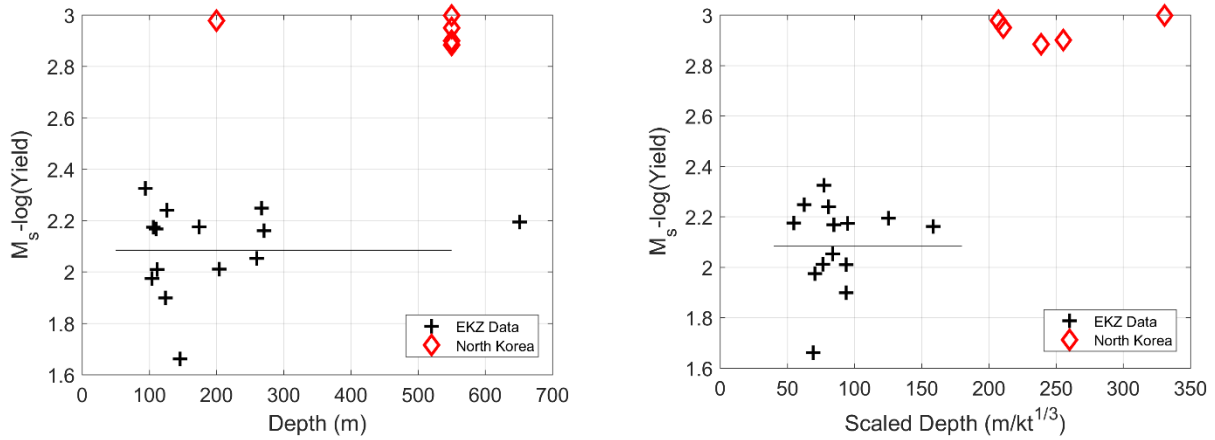


Figure 14. Left: $M_s - \log(\text{yield})$ vs. depth. Right: $M_s - \log(\text{yield})$ vs. scaled depth.

In conclusion, M_s from the small Semipalatinsk events is very consistent with the global data set of surface wave magnitudes from explosions, and with an $M_s - \log(\text{yield})$ slope of 1.0, but very inconsistent with the much larger surface waves of the five North Korean explosions.

4.2 Numerical Modeling of Seismic Waves from Explosions Beneath a Sloping Surface

Many explosions take place in mountainous areas and may be adjacent to or beneath steep slopes. We model this problem through a set of 3D finite difference calculations. These four calculations are described in Table 2. All were performed in the same uniform granite structure except for the topographic deformation. The depths and yields were chosen to cover a range of depths and scaled depths that are likely to be affected by the sloping surface.

Table 2. Slope and Shoal calculations.

Name	Surface	Depth Below Surface Vertical/Closest (m)	Explosion Yield (kt)	Scaled Depth $m/kt^{1/3}$	Comments
Shoal	Flat	367 / 367	12.5	158	Baseline case
Slope 1	Sloped	458 / 410	12.5	197 / 177	2:1 slope
Slope 2	Sloped	207 / 185	12.5	89 / 80	2:1 slope
Slope 3	Sloped	207 / 185	50	56 / 50	2:1 slope

The elevation profile used in the slope calculations is shown in Figure 15. Figure 15 also shows a blow-up of the inner grid and the final cavity within the outer grid that is used in the calculation. The explosion depth depends on whether the depth is relative to the closest point on the surface or the point vertically above the explosion. Both numbers are given in Table 2.

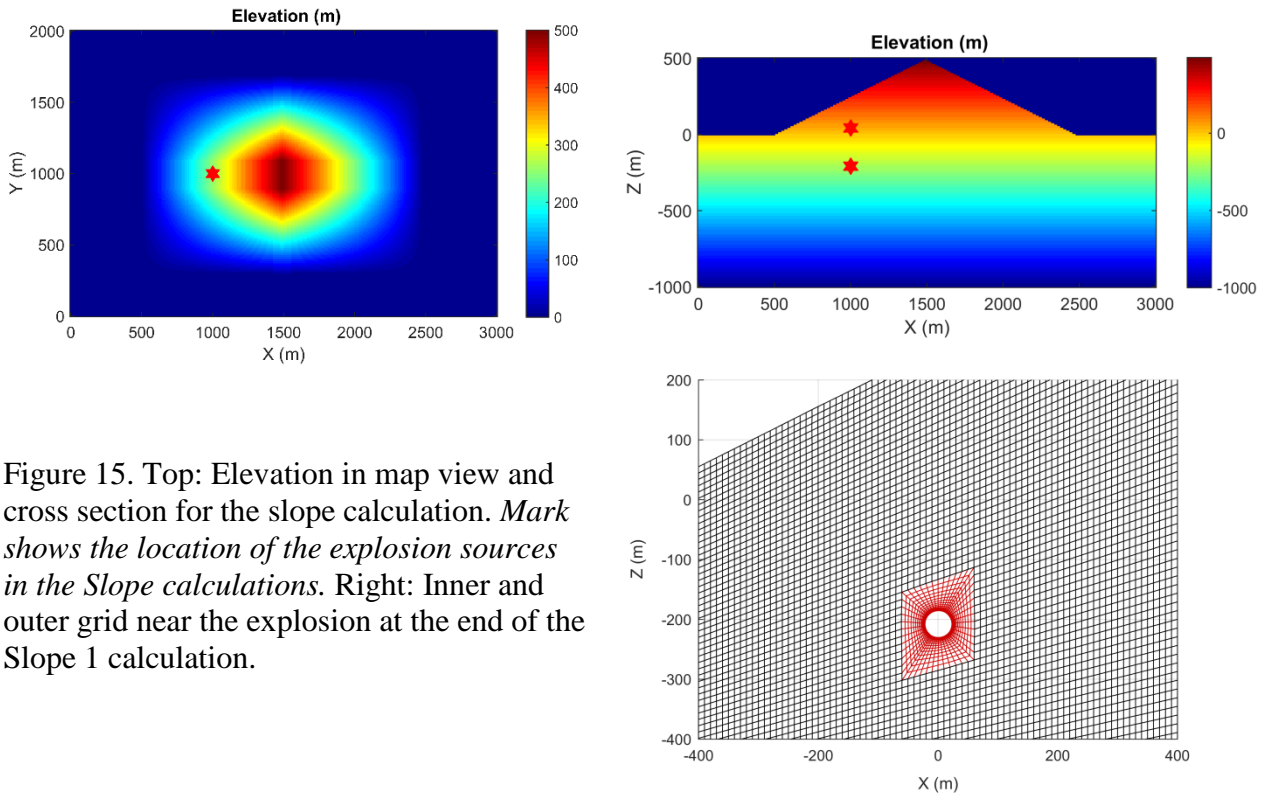


Figure 15. Top: Elevation in map view and cross section for the slope calculation. *Mark shows the location of the explosion sources in the Slope calculations.* Right: Inner and outer grid near the explosion at the end of the Slope 1 calculation.

The earth model used with the representation theorem to propagate the solution to regional and teleseismic distances is shown in Table 3. It is based on a model for the Climax stock area of the Nevada Test Site.

Table 3. Earth model used to propagate Shoal and Slope calculations

Depth km	Thickness km	Vp km/s	Vs km/s	Density g/cm ³	Q
2.0	2.0	5.175	3.025	2.600	100
3.0	1.0	5.500	3.200	2.650	100
4.0	1.0	5.900	3.400	2.750	100
8.0	4.0	5.960	3.520	2.780	350
12.0	4.0	5.960	3.520	2.780	350
16.0	4.0	6.110	3.610	2.800	375
21.0	5.0	6.110	3.610	2.800	375
31.0	10.0	6.370	3.760	2.840	400
45.0	14.0	7.900	4.420	3.200	650
55.0	10.0	8.050	4.500	3.300	600
65.0	10.0	8.050	4.500	3.300	600
∞	∞	8.100	4.500	3.300	600

4.2.1 Results

The figures on the following pages show the results of these calculations. They are divided into 4 sections – near field results, regional full-waveform seismograms, fundamental mode surface waves and far-field body waves. The near field results are divided into two sections showing all data types for each event and all events for each data type. Following is a summary of results:

1. The reflected pP and pS waves are distorted relative to the flat model. This causes a reduction in the dominant pS phase although there is additional S energy generated by the slope. The distortion of the pP phase causes a reduction in pP interference which actually generates a larger observable pP phase.
2. Regional P and S phases are slightly larger for the explosion in the mountain than beneath it, especially for paths that go across the mountain. Otherwise, there is little difference in regional phases between the flat (Shoal) and topographic (Slope 1 and Slope 2) calculations.
3. In the Slope 1 calculation where the explosion is beneath the mountain, long period surface waves show a modest increase in amplitude compared to the flat (Shoal) calculation.
4. For Slope 2 and Slope 3, where the explosion is above the surrounding terrain, surface waves are reduced significantly. This is caused by a reduction in the long period surface wave due to horizontal stress relief by the slope. Stevens et al (1993) showed that this could occur, although it requires close proximity to a steep slope.
5. Far field SH waves which do not exist for the flat surface, and are quite small even in the presence of tectonic strain release, are comparable in amplitude to SV for the mountain cases.

Note that the coordinate system used for the representation theorem calculations differs from the coordinate system used for the Cram3D calculations. In the Cram3D calculations X is east (along the mountain), Y is north (across the mountain) and Z is up. In the representation theorem calculations X (zero degrees) is north (across the mountain), Y (90 degrees) is east (along the mountain) and Z is down. See section 3 of the Cram3D User Manual (Stevens et al, 2014a) for a more detailed explanation.

4.2.2 Near Field Motion and Deformation

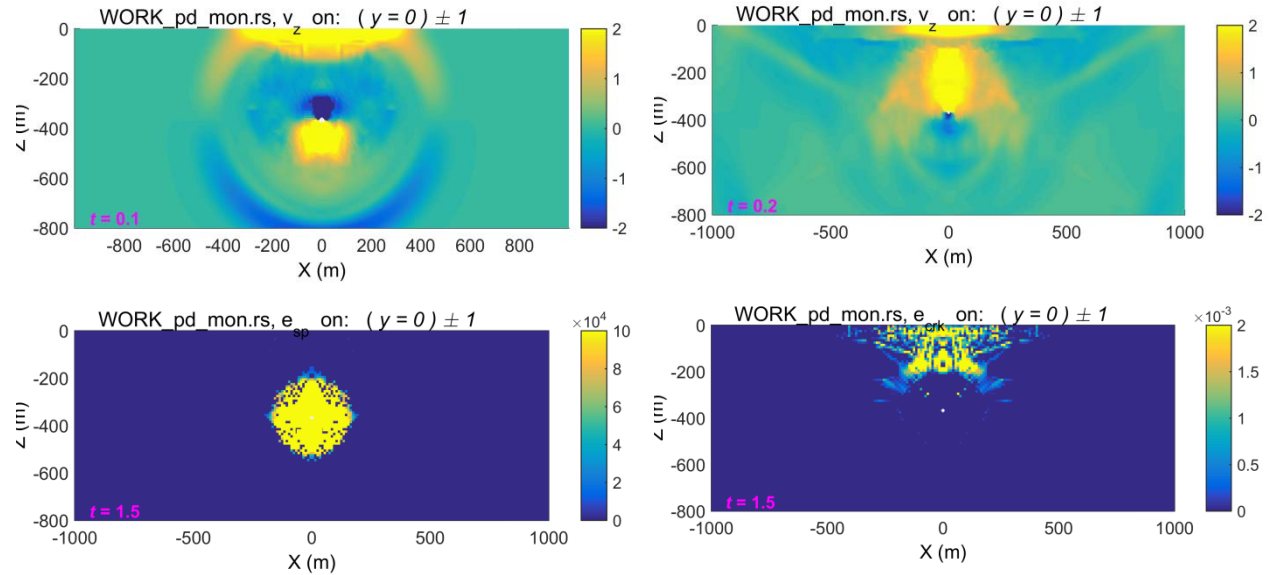


Figure 16. Shoal calculation. Top row: vertical velocity at 0.1 s (left), vertical velocity at 0.2 s (right). Bottom row: final plastic work (left), final crack strains (right).

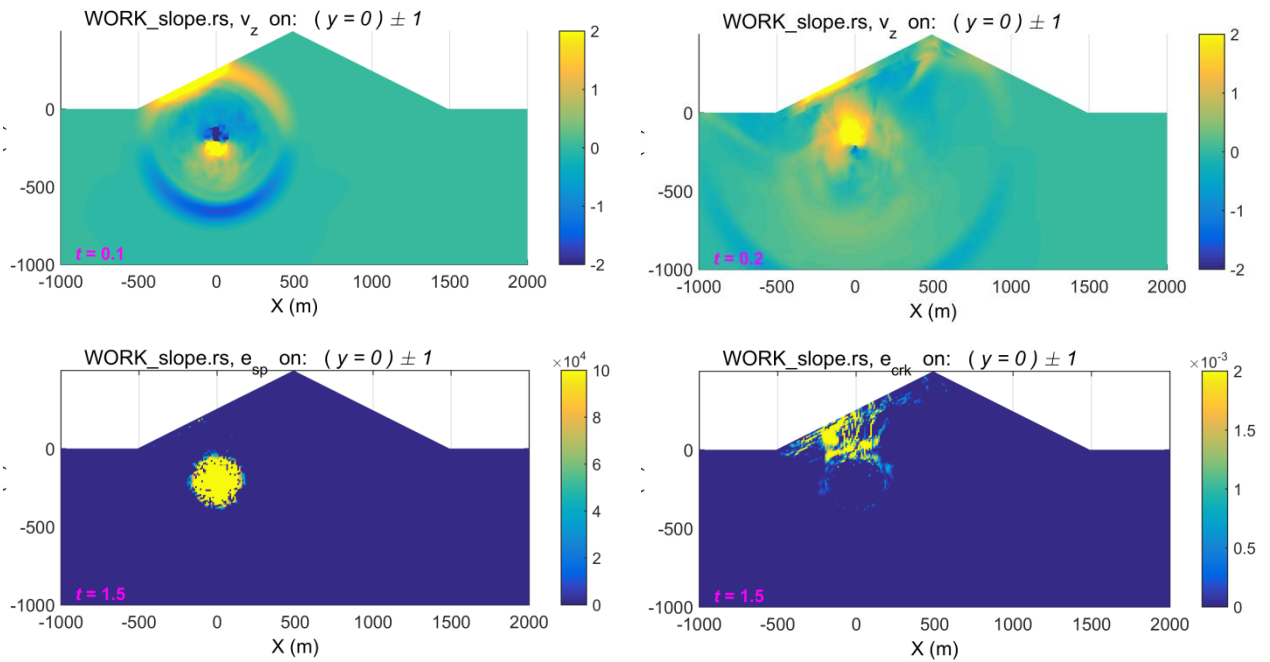


Figure 17. Slope 1 calculation. Top row: vertical velocity at 0.1 s (left), vertical velocity at 0.2 s (right). Bottom row: final plastic work (left), final crack strains (right).

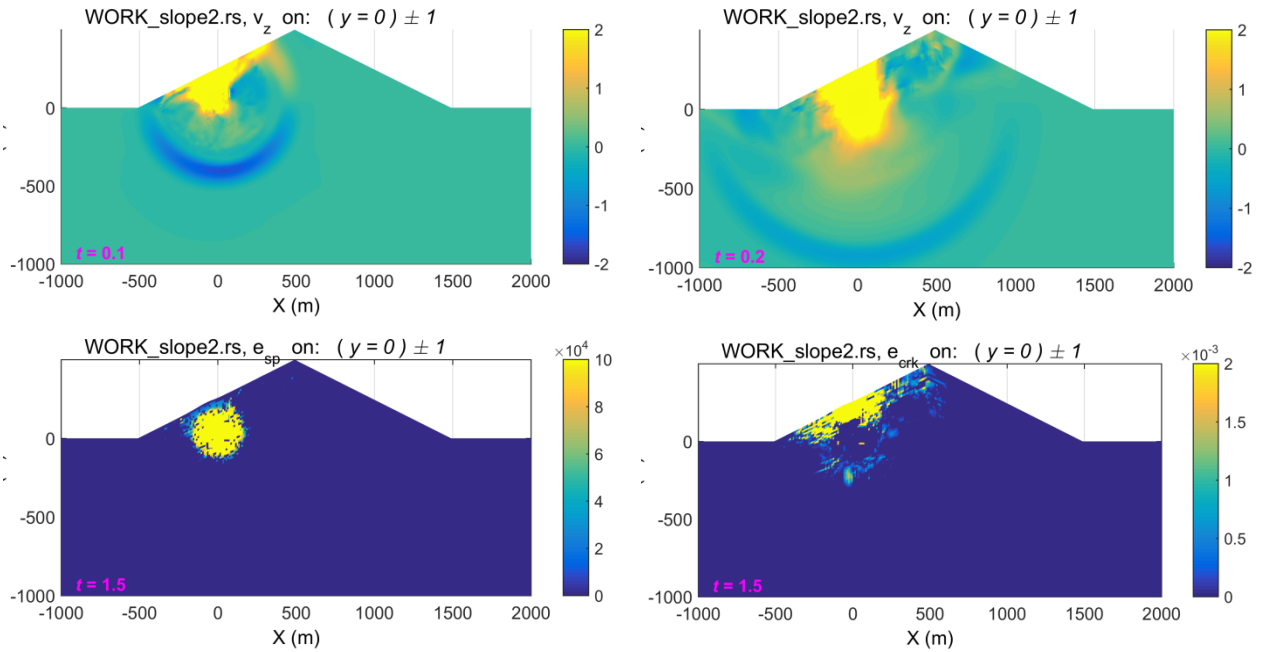


Figure 18. Slope 2 calculation. Top row: vertical velocity at 0.1 s (left), vertical velocity at 0.2 s (right). Bottom row: final plastic work (left), final crack strains (right).

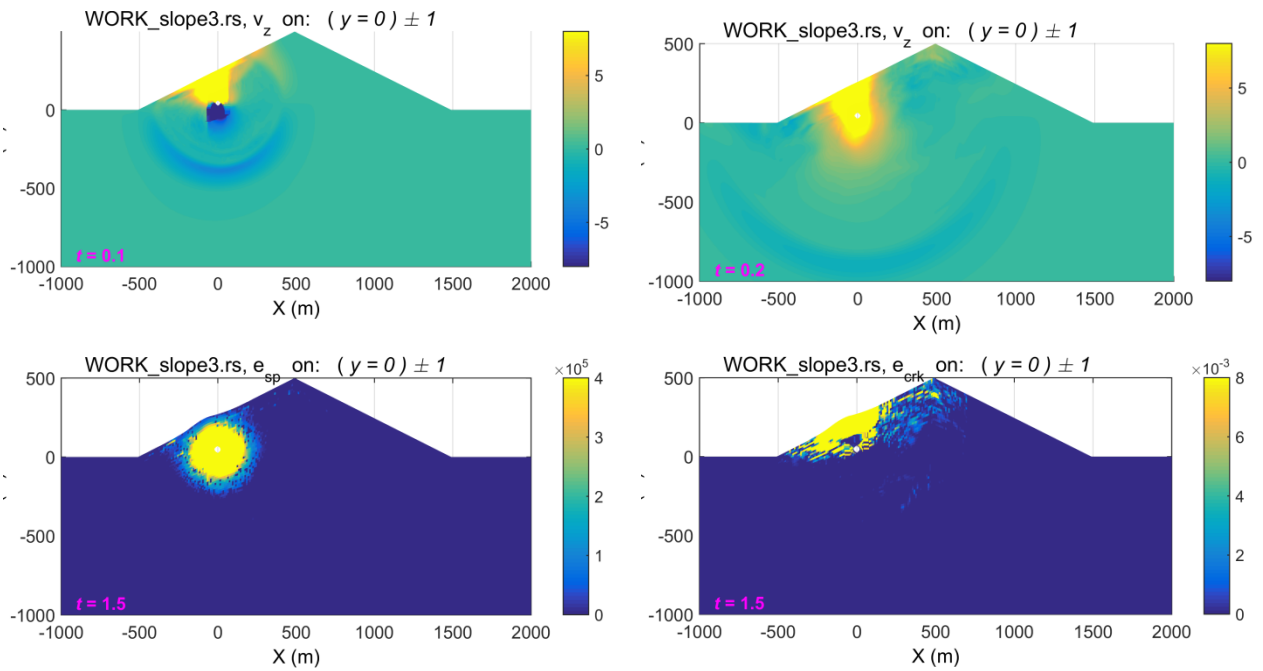


Figure 19. Slope 3 calculation. Top row: vertical velocity at 0.1 s (left), vertical velocity at 0.2 s (right). Bottom row: final plastic work (left), final crack strains (right).

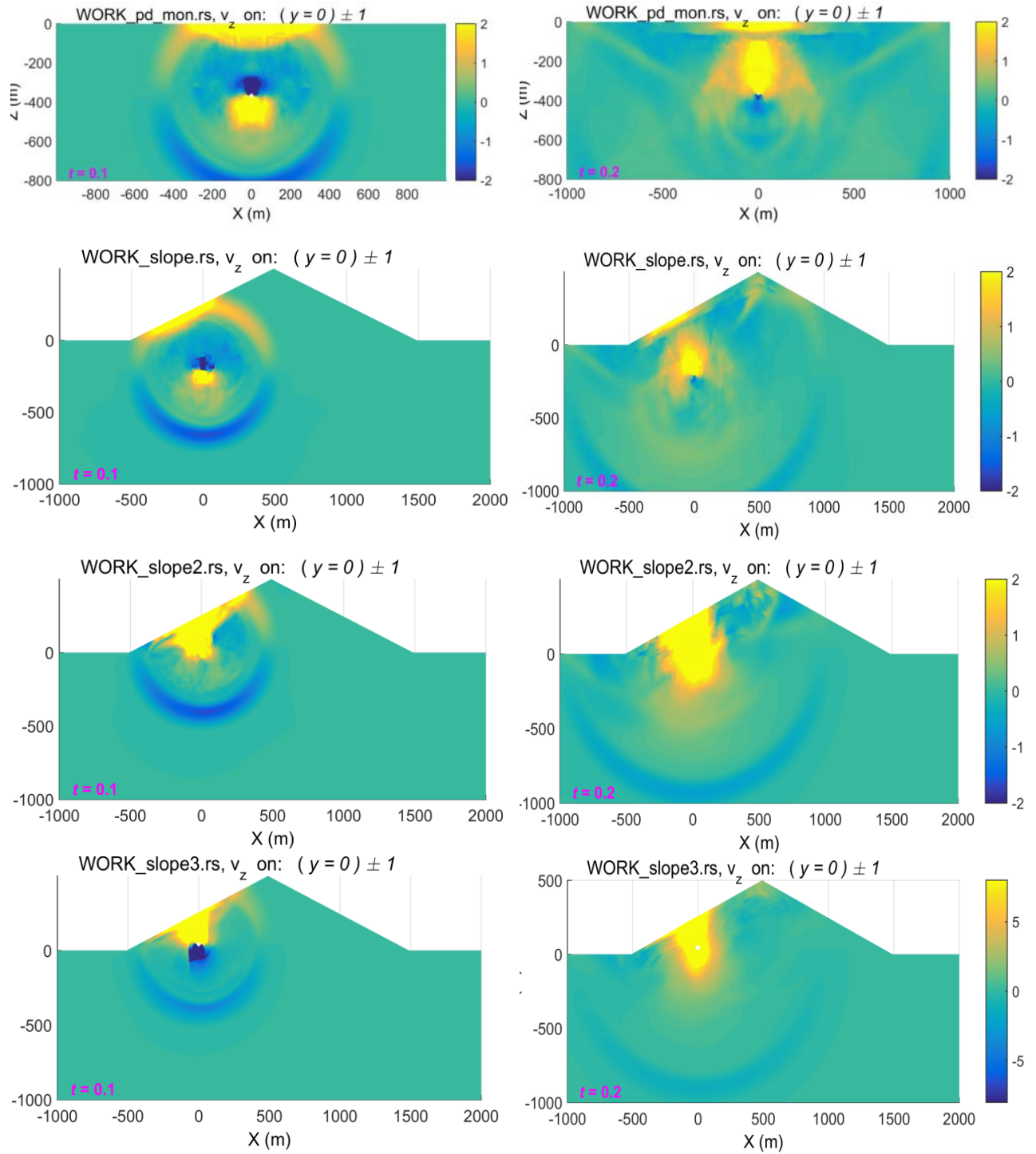


Figure 20. Left: vertical velocity at 0.1 seconds for the four runs. Right: vertical velocity at 0.2 second for the four runs. From top to bottom: Shoal, Slope 1, Slope 2, Slope 3.

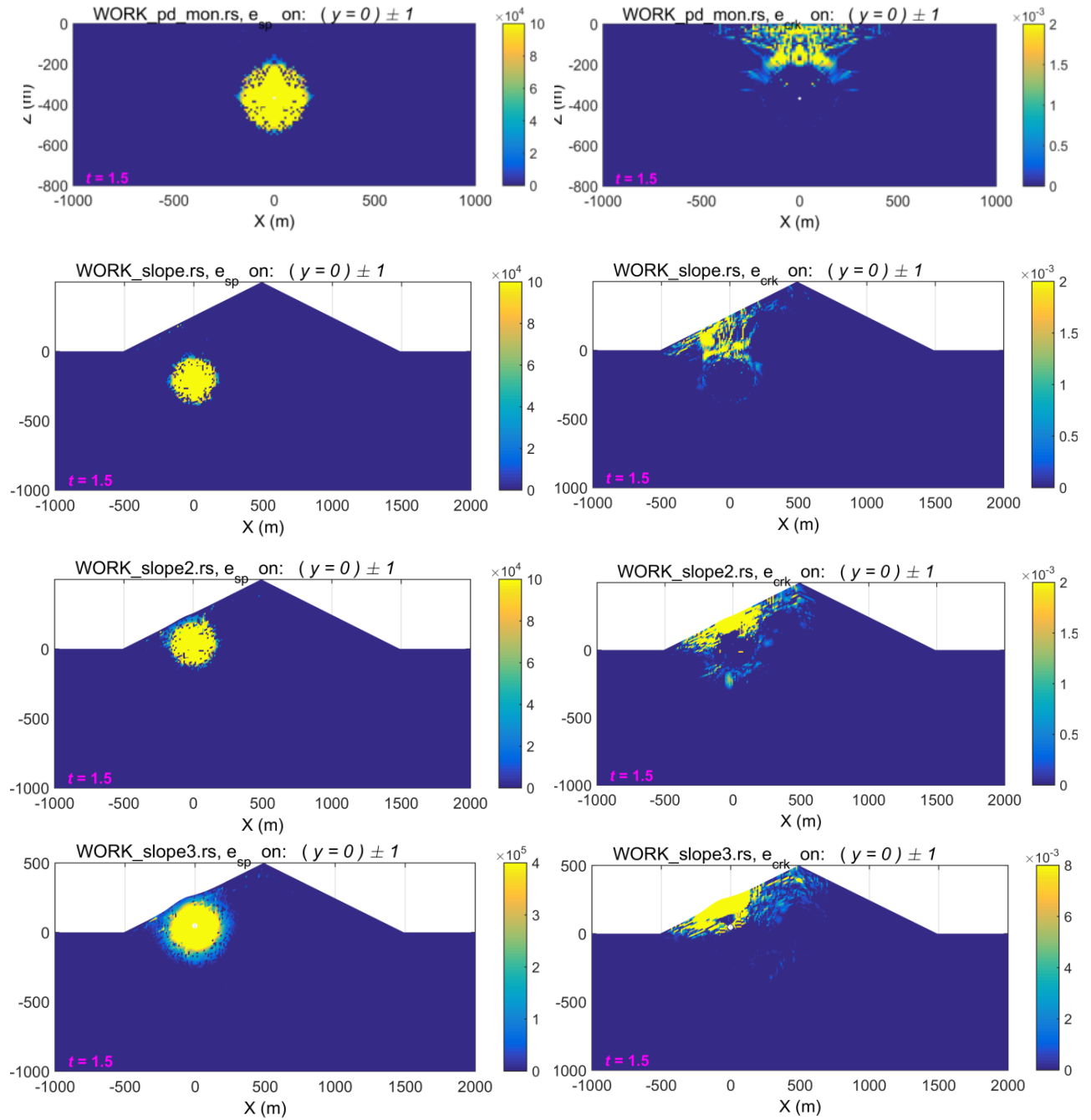


Figure 21. Left: Final plastic work for the four runs. Right: Final crack strains for the four runs. From top to bottom: Shoal, Slope 1, Slope 2, Slope 3.

4.2.3 Regional Waveforms

In this section we show comparisons of regional waveforms at 250 km distance from the Shoal and Slope calculations. Figure 22 shows a comparison of the regional waveforms from the Shoal and Slope 1 calculations, and a comparison with a 1D model. The 1D calculation is a full waveform seismogram from a point explosion source at a depth of 367 meters scaled to the moment of a 12.5 kiloton Mueller-Murphy (Murphy, 1977) source (4.21×10^{15} N-m). The 1D comparison for the Slope 2 and Slope 3 calculations are for a point source at 167 meters depth (moment 5.48×10^{15} N-m), and for Slope 3 the moment is increased to the moment of a 50 kiloton Mueller-Murphy source (1.83×10^{16} N-m).

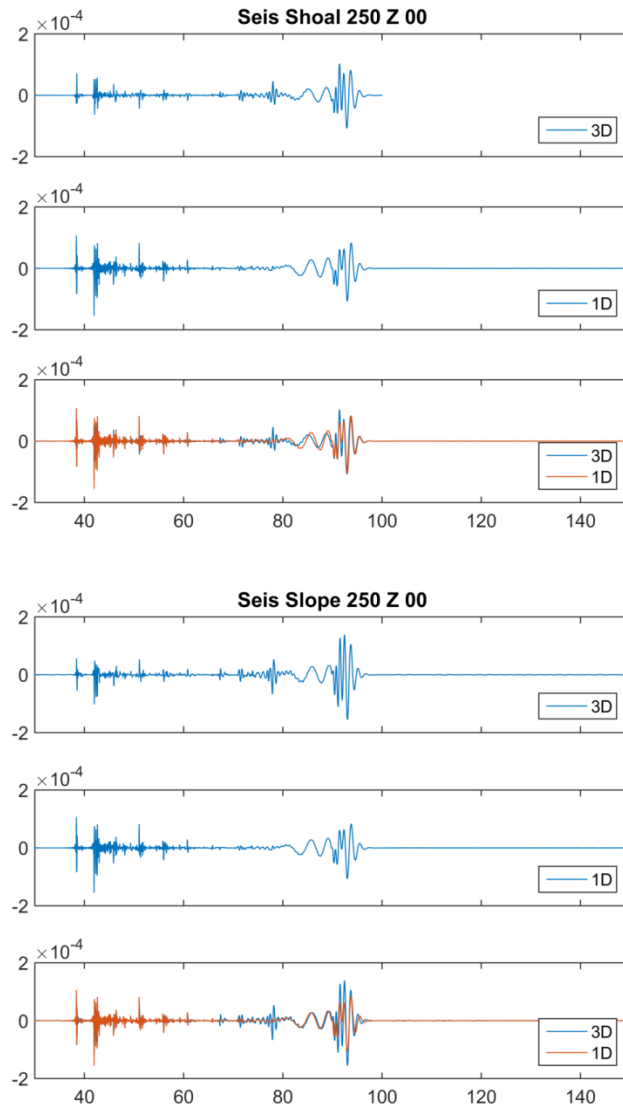


Figure 22. Regional waveforms at 250 km from the Shoal calculation (top) and Slope 1 calculation (bottom). *Waveforms from Slope 1 are slightly larger than for Shoal, and waveforms for Shoal are slightly smaller than the 1D calculation.*

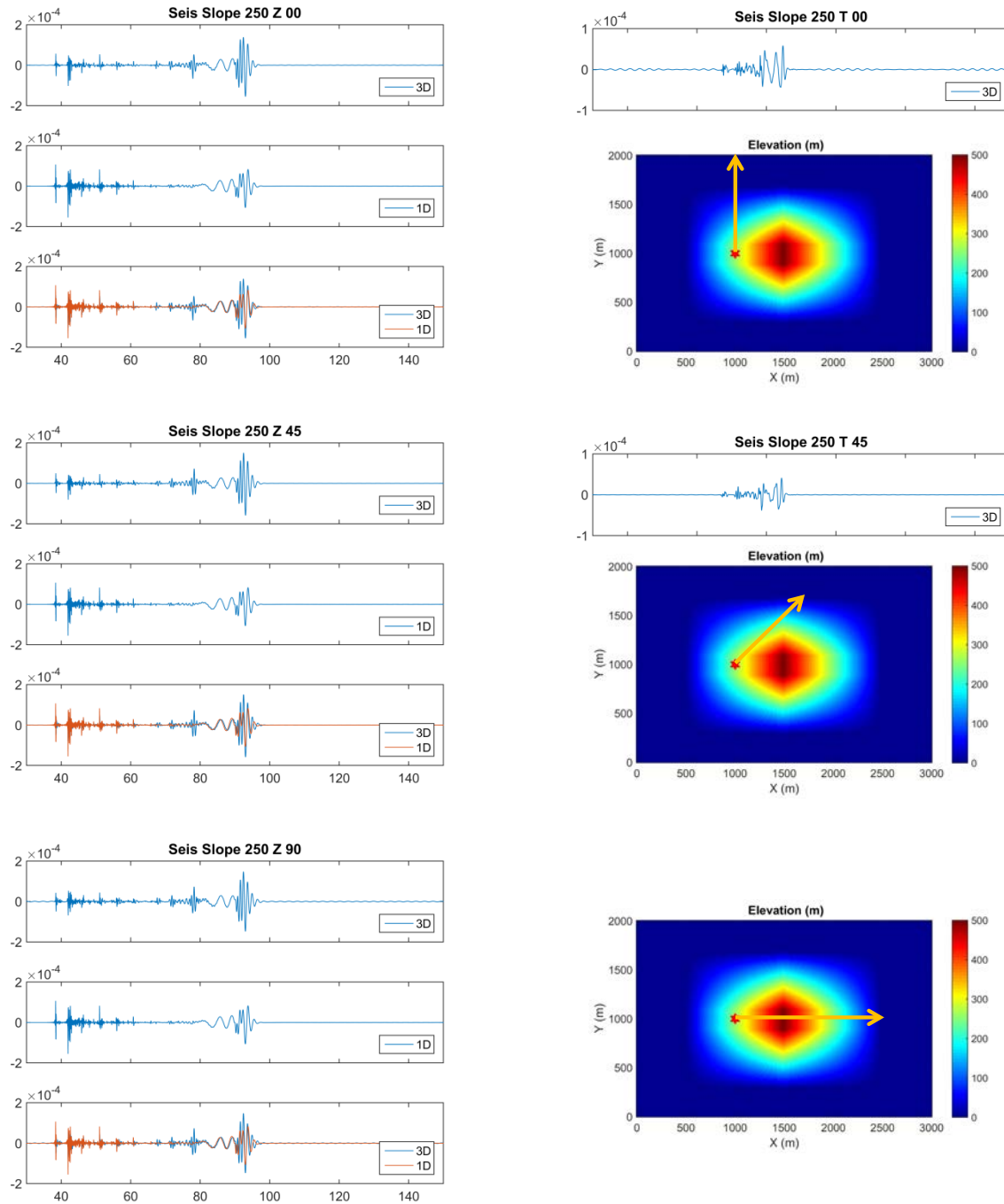


Figure 23. Full waveforms at 250 km from the Slope 1 calculation. Left: vertical in 3 directions. Right: Tangential in 3 directions and diagram of direction. (Tangential at 90 degrees is zero).

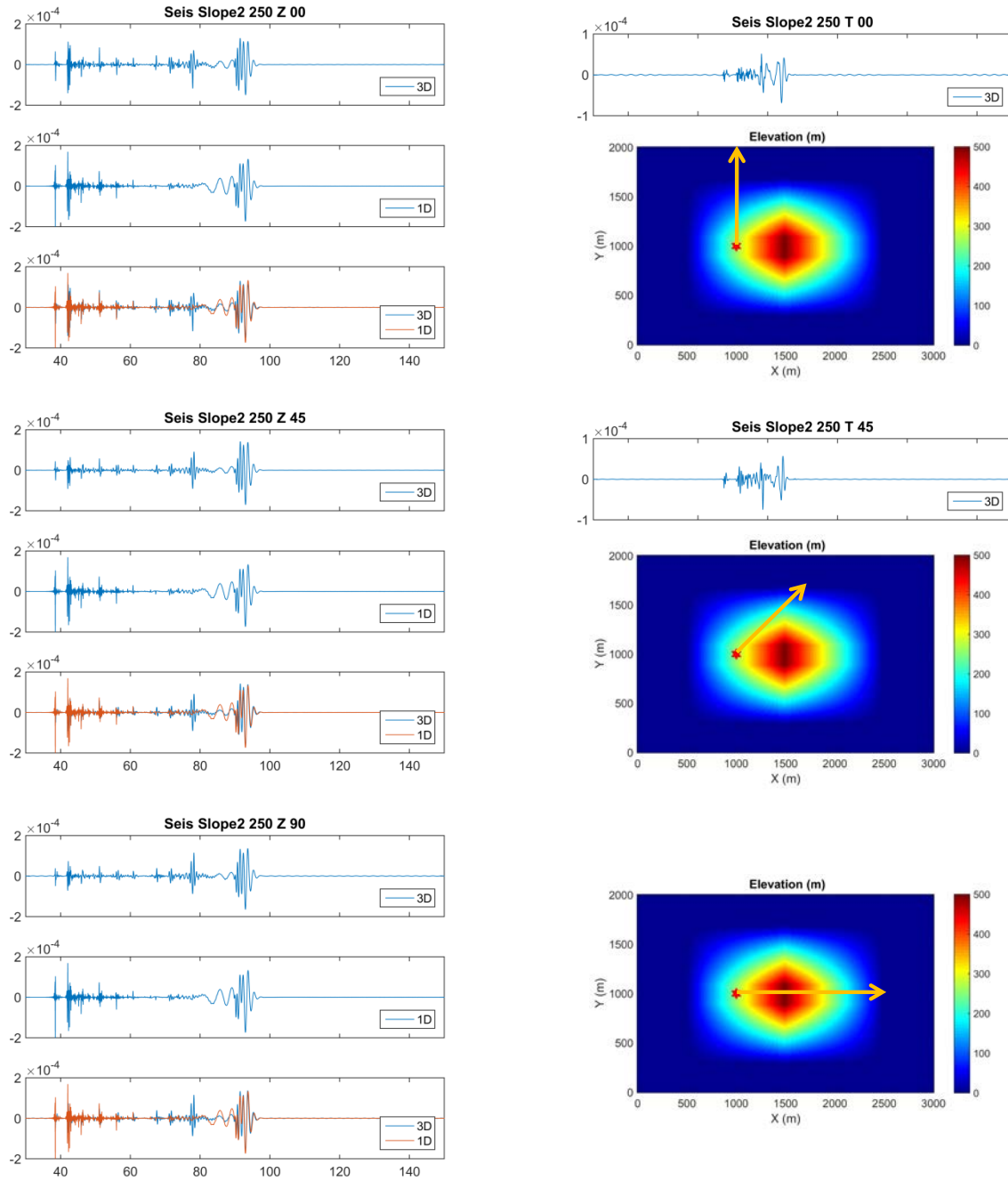


Figure 24. Full waveforms at 250 km from the Slope 2 calculation. Left: vertical in 3 directions. Right: Tangential in 3 directions and diagram of direction.

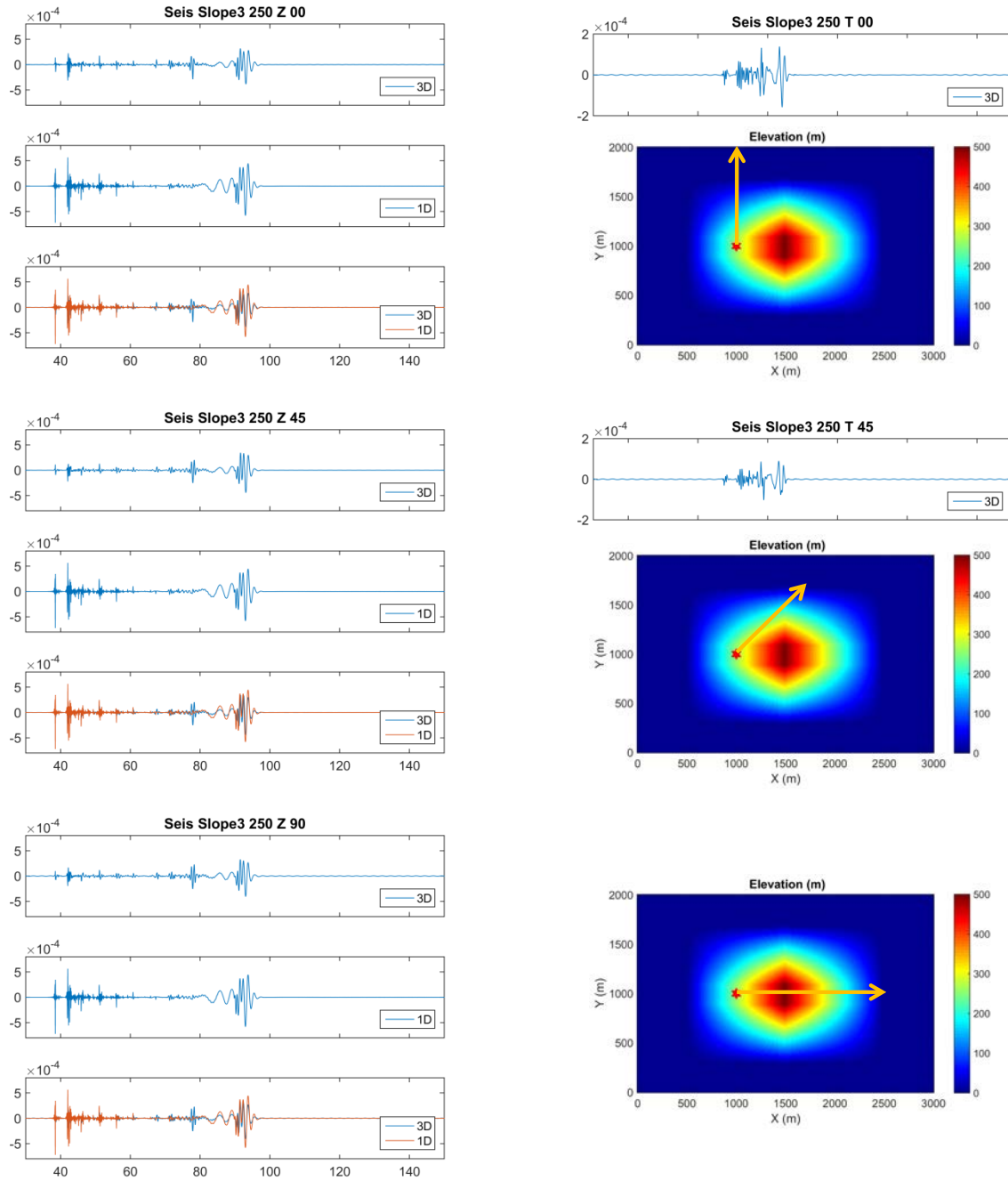


Figure 25. Full waveforms at 250 km from the Slope 3 calculation. Left: vertical in 3 directions. Right: Tangential in 3 directions and diagram of direction.

4.2.4 Surface waves

In this section we show comparisons of long period fundamental mode surface waves (Rayleigh and Love) at 2000 km distance from the Shoal and Slope calculations. Figure 22 shows a comparison of Rayleigh waves from the Shoal and Slope 1 calculations, and a comparison with a 1D model. The 1D calculation is a fundamental mode Rayleigh wave seismogram from a point explosion source at a depth of 367 meters convolved with a 12.5 kiloton Mueller-Murphy source. The 1D comparison for the Slope 2 and Slope 3 calculations are for a point source at 167 meters depth, and for Slope 3 the yield is increased to 50 kilotons.

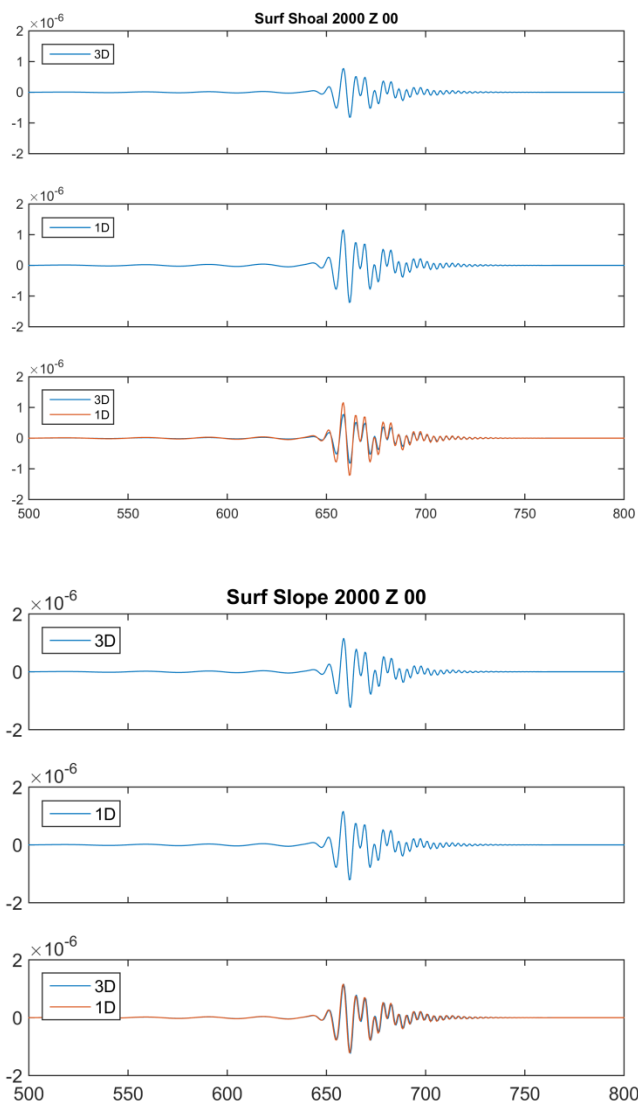


Figure 26. Long period surface waves at 2000 km from the Shoal calculation (top) and Slope 1 calculation (bottom). *Waveforms from Slope 1 are slightly larger than for Shoal, and waveforms for Shoal are slightly smaller than the 1D calculation.*

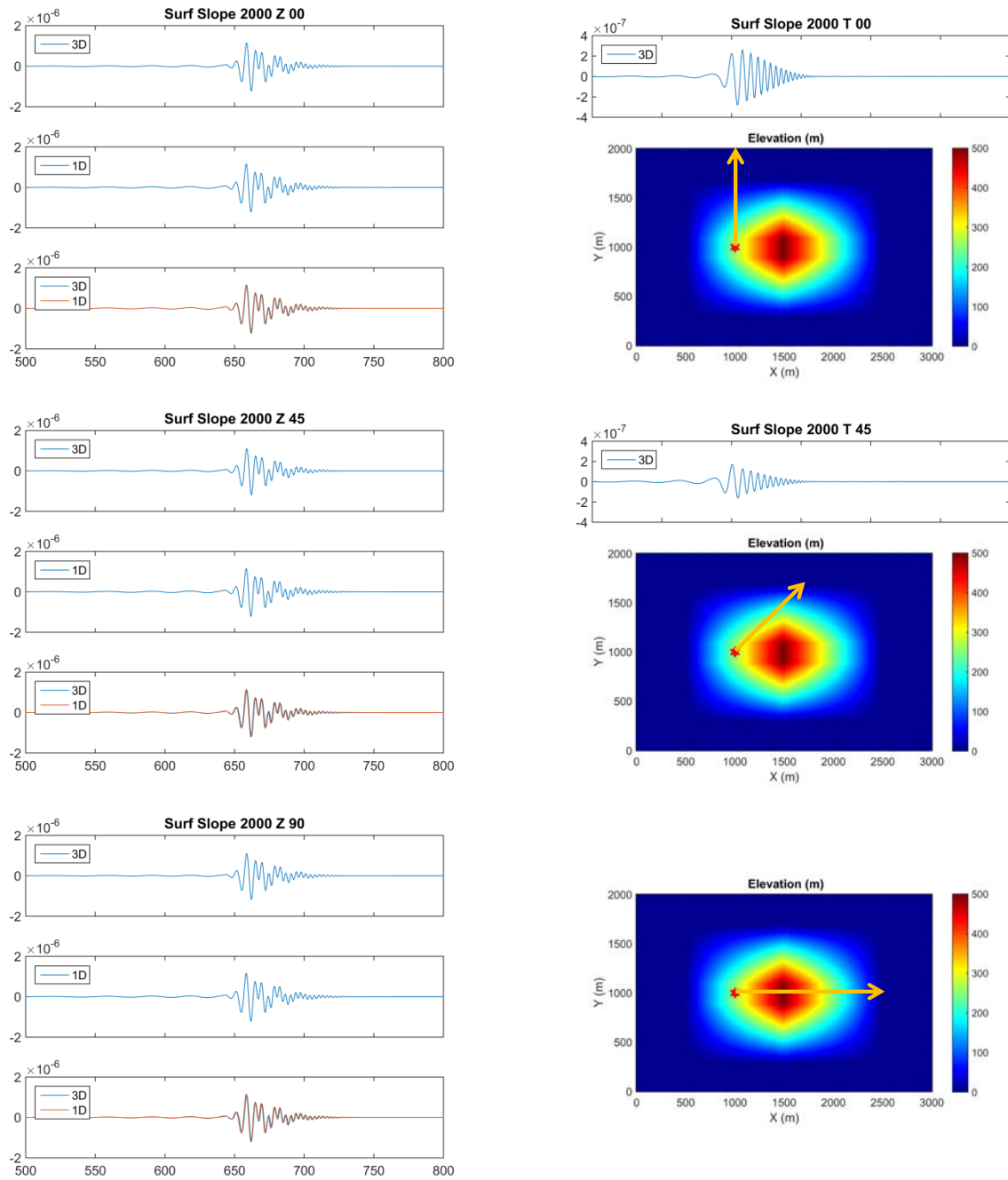


Figure 27. Surface waves at 2000 km for the Slope 1 calculation.

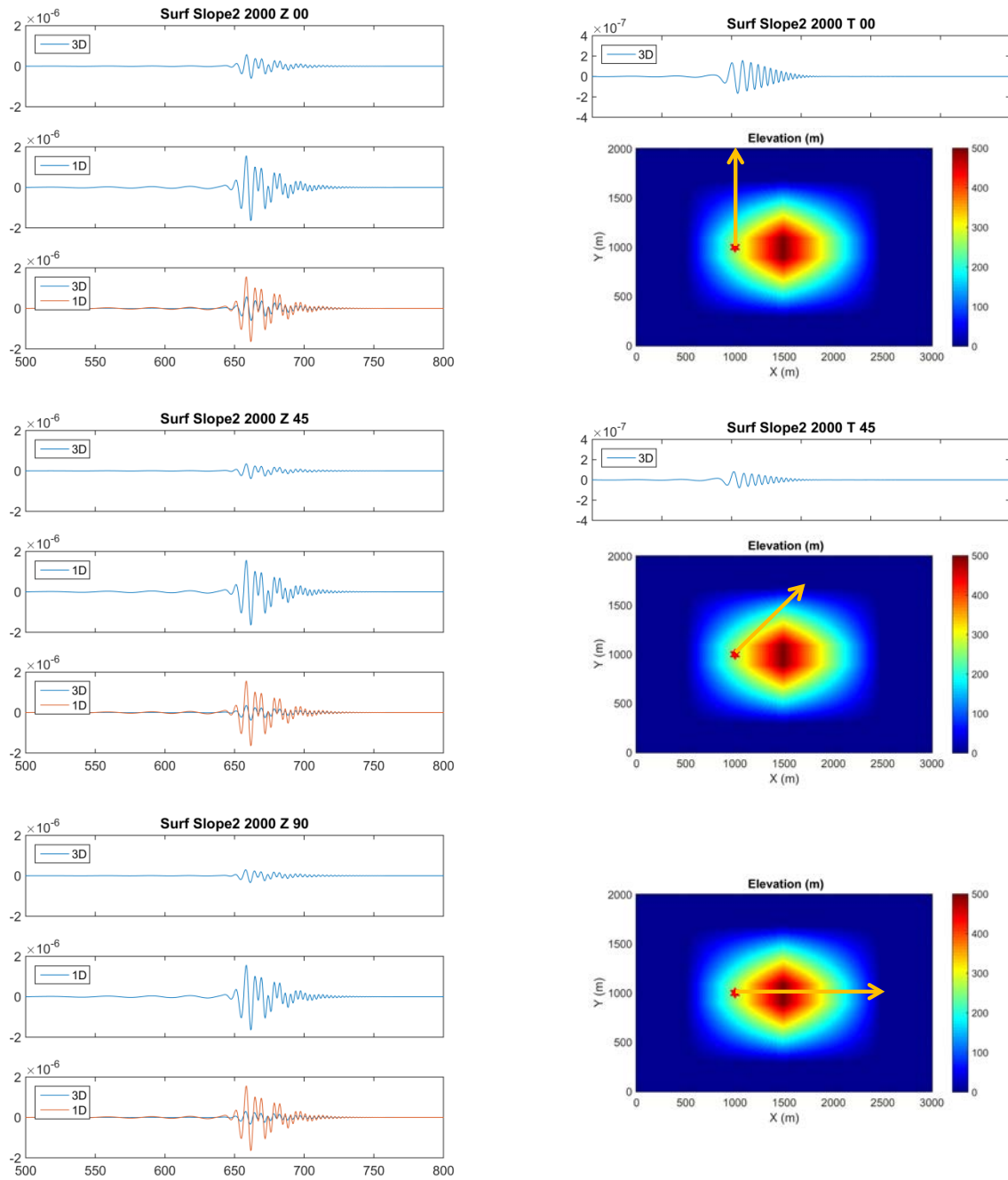


Figure 28. Surface waves at 2000 km for the Slope 2 calculation.

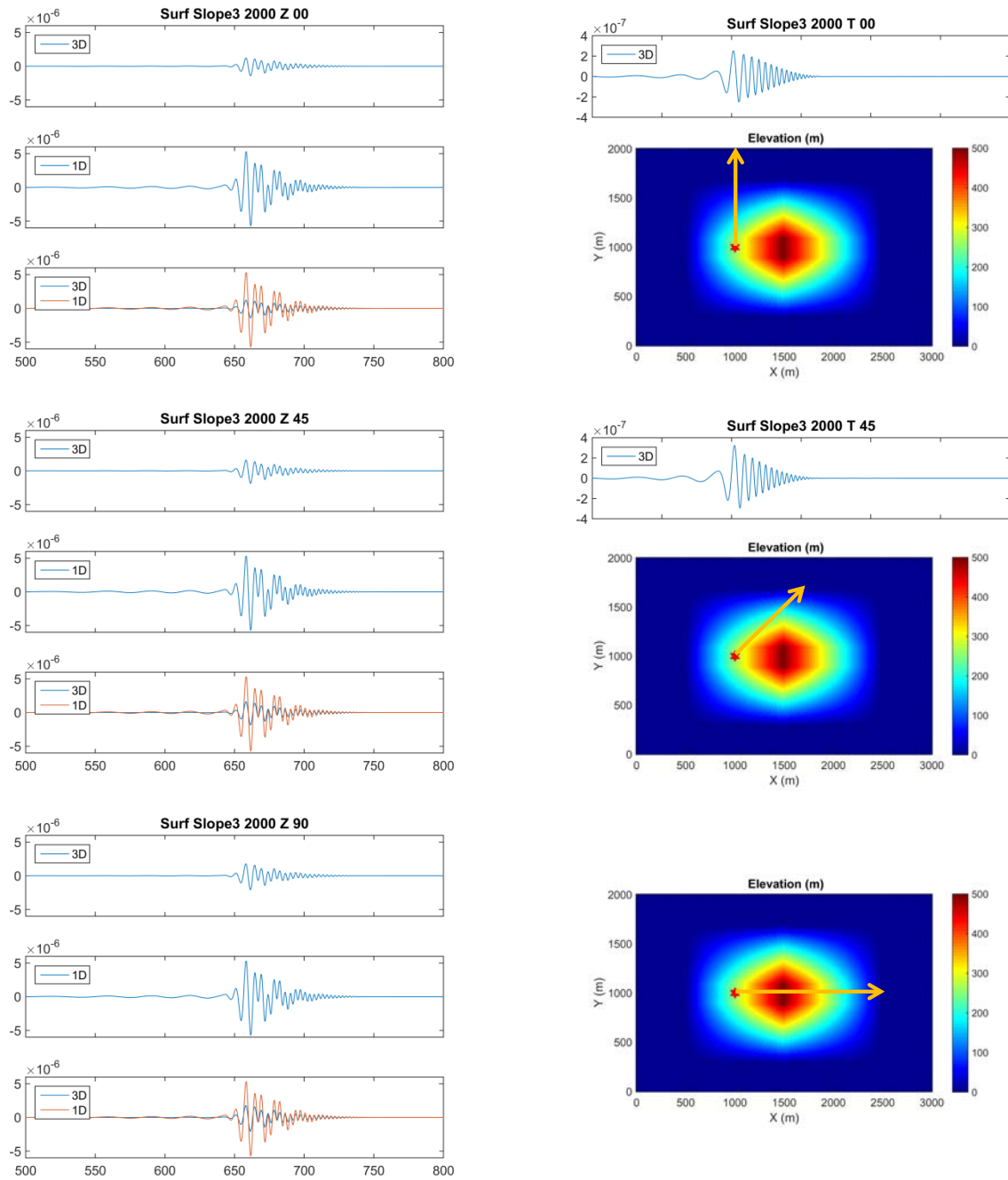


Figure 29. Surface waves at 2000 km for the Slope 3 calculation.

4.2.5 Body waves

In this section we show far field P and S body waves from the Shoal and Slope calculations calculated for a uniform structure 1000 km below the source. For comparison, we also show body waves from the Shoal calculations with tensile and compressive prestress (Stevens et al, 2014). P and SV waves are all shown for a takeoff angle of 30° while SH waves are shown for three takeoff angles of 10, 20 and 30 degrees.

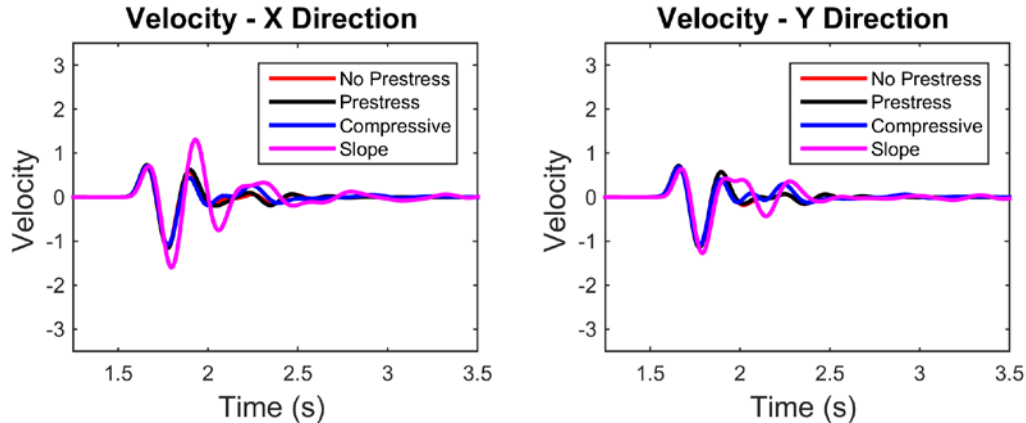


Figure 30. Slope 1 P, together with Shoal calculation with no prestress and with compressive and tensile prestress. *Similar plots follow for the other cases.*

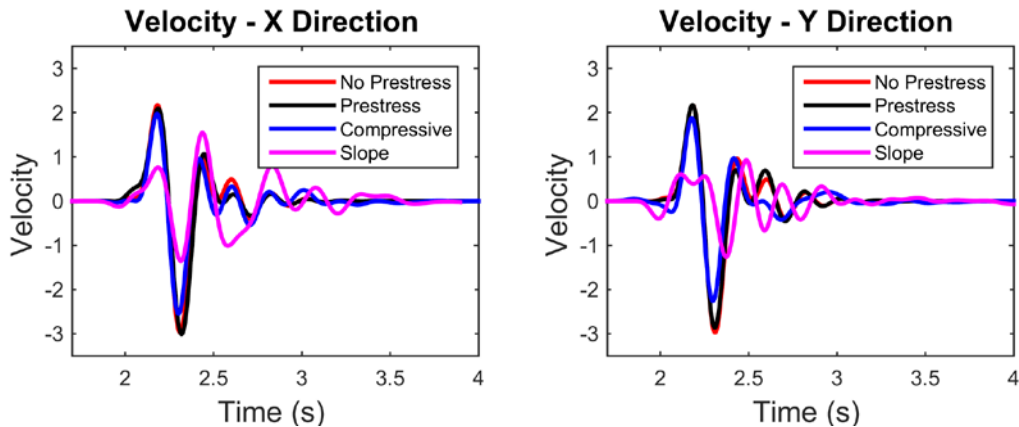


Figure 31. Slope 1 SV.

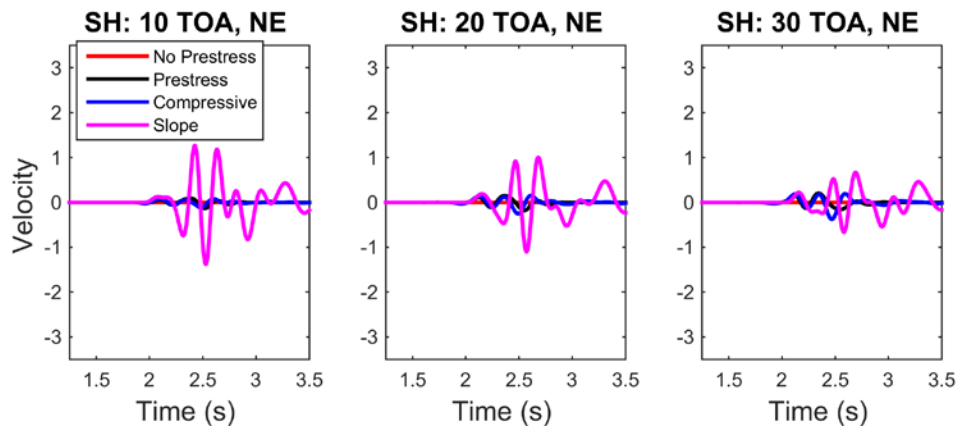


Figure 32. Slope 1 SH.

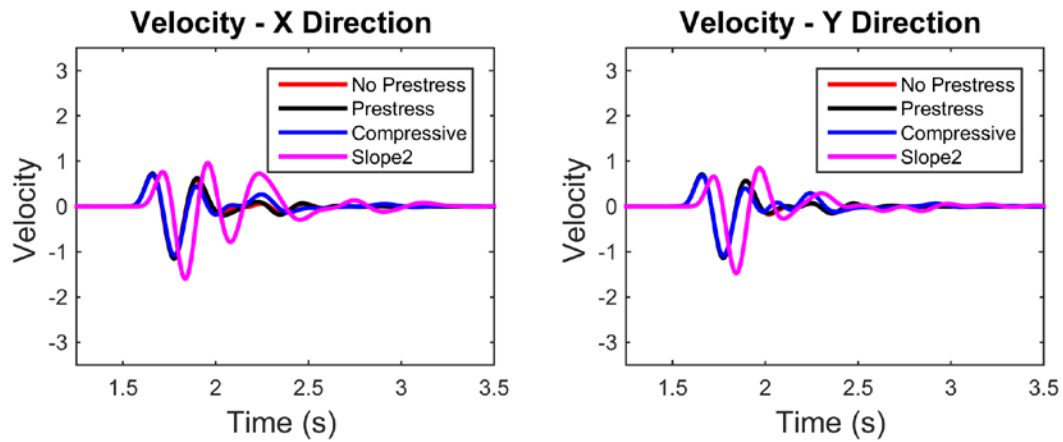


Figure 33. Slope 2 P.

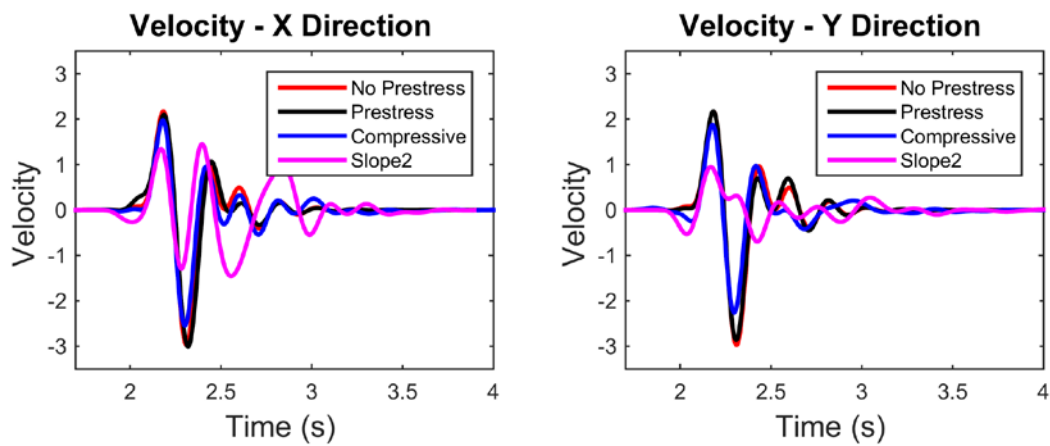


Figure 34. Slope 2 SV.

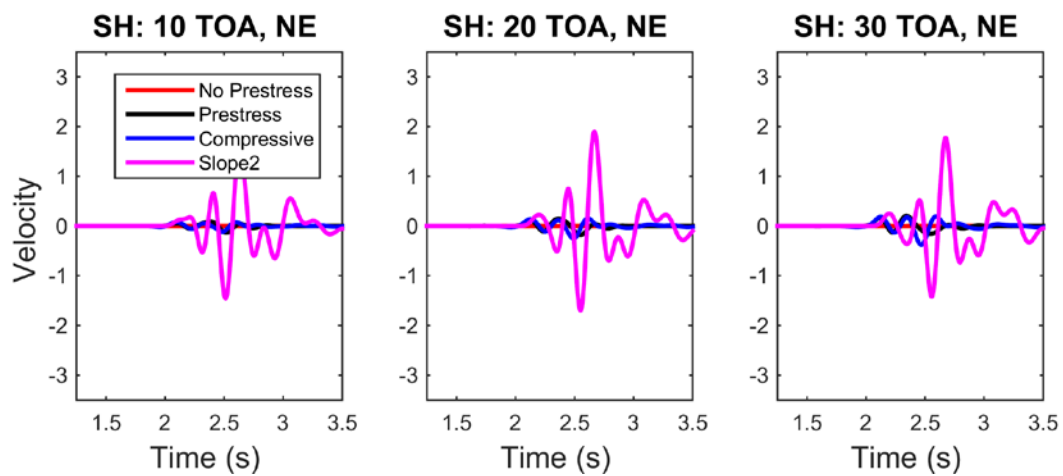


Figure 35. Slope 2 SH.

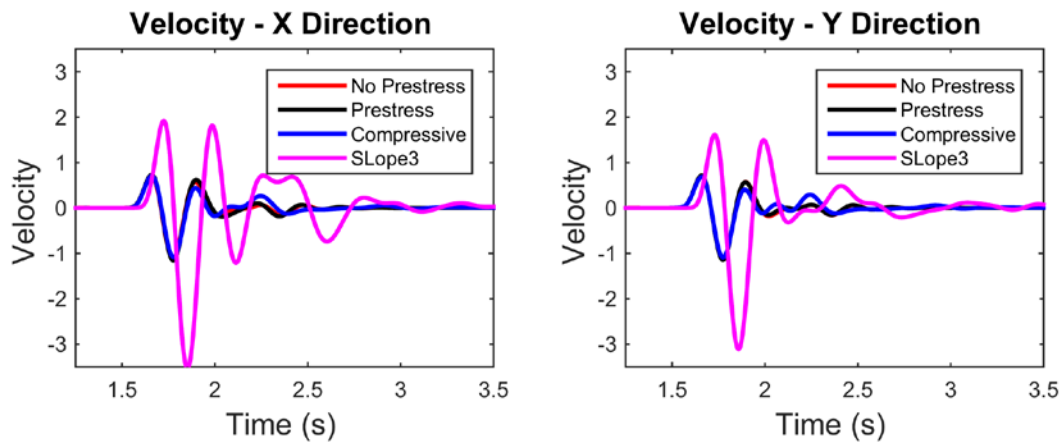


Figure 36. Slope 3 P (Note – this is a 50 kt explosion compared to a 12.5 kt explosion).

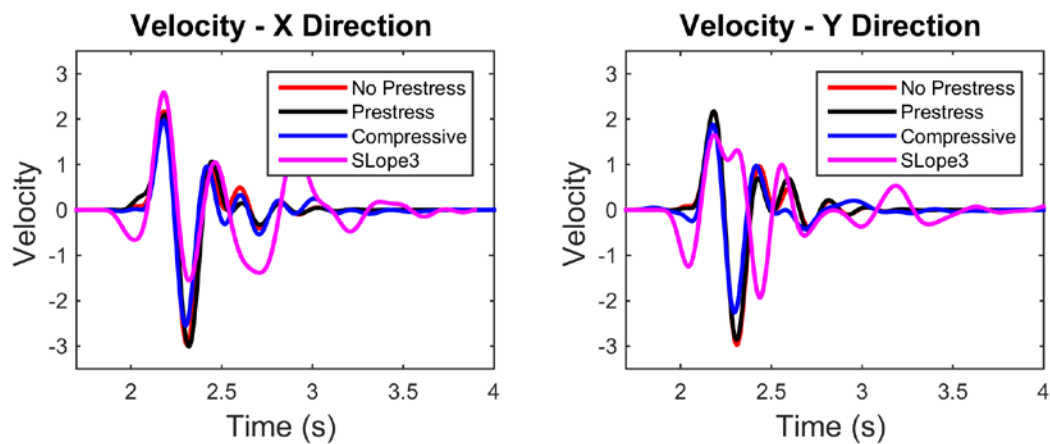


Figure 37. Slope 3 SV.

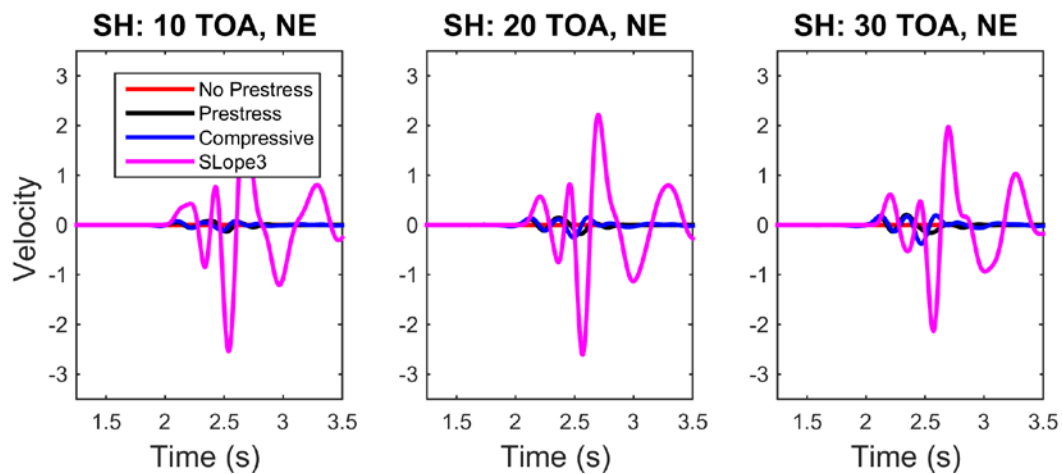


Figure 38. Slope 3 SH.

4.3 Decomposition of the Seismic Source of Surface Waves in 3D Calculations

In the previous section we looked at the effect of source location within and under a mountain. Now we examine what those variations do to the seismic signals. We first look at how surface waves are generated by examining the Green's functions and displacements on the monitoring surface. In section 3.2, we showed that the synthetic seismogram at the receiver point X outside of the monitoring surface can be obtained by integrating over the monitoring surface S_M using the following formula:

$$u_i(X) = \int_{S_M} \left\{ G_j^i(\xi; X) * T_j^M(\xi) - u_j^M(\xi) * S_{jk}^i(\xi; X) n_k \right\} dA$$

where $G_j^i(\xi; X)$ and $S_{jk}^i(\xi; X)$ are the Green's function and the stress tensor on the monitoring surface due to a unit impulsive force at X in direction i , T_j^M is the traction on the monitoring surface due to the seismic source, u is the displacement on the monitoring surface, and n is the normal to the monitoring surface. Because both the force and impulse integrated over the monitoring surface must vanish in the late time/low frequency limits, the integral over the Green's function at long periods is very small (making sure this happens is in fact one of the more difficult problems with numerical modeling of surface waves as a tiny amount of residual force or impulse can generate a large, spurious surface wave). The long period surface wave is therefore generated by the static displacement multiplied by the Green's function stresses integrated over the monitoring surface. Because of the free surface boundary condition, the Green's function stresses for vertical displacements are small at shallow depths and long periods, so the surface waves are primarily generated by the static horizontal displacements. This can be seen in Figure 39 which shows the numerical value of the Green's function stresses at 20 seconds from the surface to 600 meters depth. The first two indices in the tensor correspond to the normal direction to the surface and the component of displacement at the surface point. So, for example, in the direction of the X axis the surface wave is primarily generated by the final displacement in the X direction and secondarily by the final displacement in the Y direction with only a small contribution from the final vertical displacements.

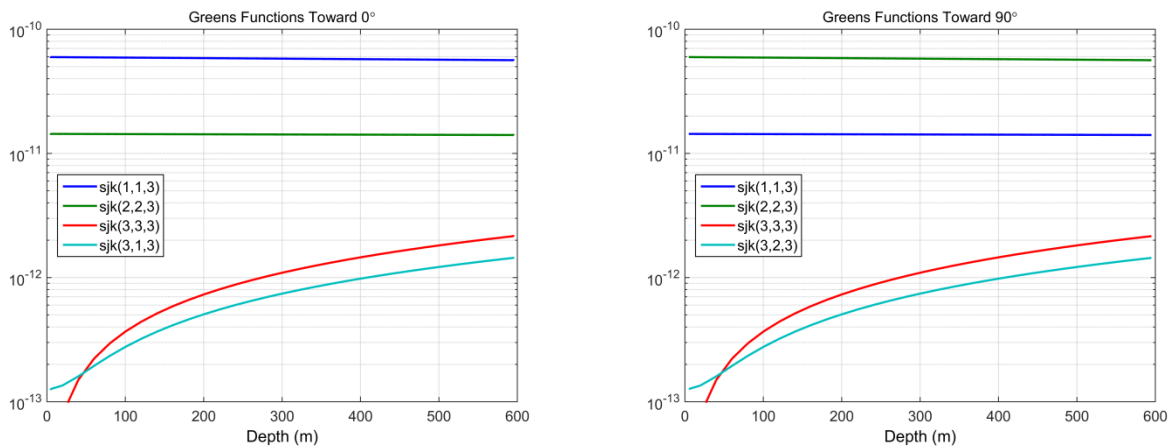


Figure 39. Green's function stresses for generation of a vertical component Rayleigh wave (third index) in the direction of the X (left) and Y (right) axes at 20 seconds period. *Long period surface waves are primarily generated by the static horizontal displacements.*

The Green's functions on the monitoring surface are the same for all four of the calculations, but the final static displacement is not, and the differences between them are interesting. Figure 40 shows the horizontal displacement normal to the monitoring surface in two orthogonal directions. The most notable difference is the reduced displacement in Slope 2, which leads to the reduced surface wave amplitudes shown earlier. However, the Slope 1 calculation has larger displacement than Shoal, also consistent with the surface waves shown earlier. It is not clear why the displacement and surface wave amplitudes for Slope 1 are increased. One possible explanation is that the reduced pressure under the mountain compared to a flat surface at the same depth causes some additional dynamic deformation near the source. Another possibility is that the explosion and mountain together cause more near-surface horizontal displacement than a more deeply buried source with a flat surface. The effect of the mountain on the near field displacements is largest along the direction of the mountain causing more displacement in Slope 1 and less in Slope 2 in that direction.

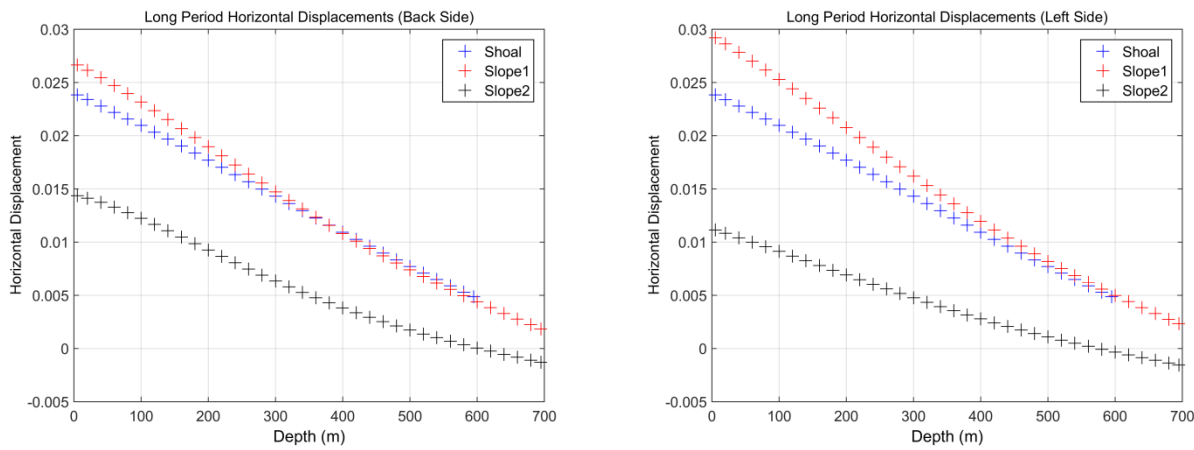


Figure 40. Horizontal displacements normal to the monitoring surface vs. depth for three calculations. Left: back side of the calculation (across mountain). Right: left side of calculation (along mountain).

4.4 Numerical Modeling of Seismic Waves from Explosions at the North Korea Nuclear Test Site

We perform calculations of nuclear explosions at the North Korean Test Site, an area with substantial topography and where explosions have generated anomalously large surface waves. We performed the four 3-D calculations described in Table 2 with the source at a single horizontal grid location but at different depths. The best estimate of the source depth of the 2009 North Korean test is 540 meters (Murphy et al, 2013), and the other source depths are selected to model a range of depths from shallower to deeper. An explosion yield of 12.5 kilotons was used in all calculations, allowing direct comparison with the laterally homogeneous Shoal simulation as a baseline. Table 2 lists the actual depths of burial, the minimum distance to surface and the depths of equal overburden pressure in the layered model bounding the grid, denoted as “pressure” depth in columns 4 and 7. Note that the pressure is lower in all cases than the same depth in a comparable flat surfaced model, and so the “pressure depth” is shallower.

Table 4. Summary of simulations of 12.5 kt explosions at North Korea test site.

Name	Source Depth (m)			Scaled Source Depth (m/kt ^{1/3})			Comments
	Vertical	Min to Surface	Pressure	Vertical	Min to Surface	Pressure Depth	
NK-100	100	93	32	43	40	14	-
NK-200	200	187	65	86	81	28	-
NK-540	540	506	196	233	218	84	Estimated depth of 2009 event
NK-800	800	744	457	345	320	197	-

The grid was uniformly filled with the same granite material model used for the Shoal and Slope calculations. The regional earth model used for propagation with the representation theorem is specified in Table 5. This is the earth model at the location of the North Korean test site from Stevens et al (2005), with the 2 km surface layer replaced with the properties of the granite model used in the nonlinear calculations. Q was set to a uniform value of 400 in the crust and upper mantle from 4 to 80 km depth.

Table 5. Regional material model surrounding the North Korea test site

Depth km	Thickness km	Vp km/s	Vs km/s	Density g/cm ³	Q
2.0	2.0	5.175	3.025	2.600	200
4.0	2.0	5.356	3.100	2.625	300
6.0	2.0	5.538	3.170	2.650	400
8.0	2.0	5.719	3.240	2.675	400
11.0	3.0	5.900	3.312	2.700	400
22.0	11.0	6.402	3.593	2.736	400
32.0	10.0	7.016	3.938	2.960	400
48.0	16.0	8.031	4.508	3.330	400
64.0	16.0	7.736	4.343	3.223	400
80.0	16.0	7.431	4.171	3.111	400
100.0	20.0	7.434	4.173	3.112	75
120.0	20.0	7.587	4.259	3.168	75
142.5	22.5	7.733	4.341	3.221	76
165.0	22.5	7.828	4.394	3.256	76
187.5	22.5	7.929	4.450	3.293	77
210.0	22.5	8.110	4.553	3.359	78
235.0	25.0	8.366	4.696	3.453	134
260.0	25.0	8.586	4.820	3.533	135
∞	∞	8.742	4.832	3.541	137

The simulation grid used the actual topography from the North Korea test site. We located the source horizontally at the epicenter estimated by Zhang and Wen (2013) of the 2009 test event, illustrated in Figure 41, Panel (a), along with other proposed locations for that event. The black box in Panel (a) shows the boundaries of the simulation. This topography was tapered to a uniform elevation to construct a simulation-grid topography, shown in Panel (b), that allows for application of the representation theorem to propagate motion to farther distances. Panels (c) and (d) show south-to-north (S-N) and west-to-east (W-E) pressure profiles through the source for an isostatically compensated earth, which was our starting equilibrium. The source is located midway down the long sloping south face of the mountain, so that there is significant topographic asymmetry about vertical W-E plane through the source. In contrast there is much less asymmetry about the vertical S-N through the source. The effective overburden is substantially reduced within or just below the mountain compared to sources at the same depth under the layered-earth structure that bounds the grid as indicated in the Table 4. The “pressure” depth under the source epicenter is reduced by a factor of 2 near the surface and by almost a factor of 2 at 800m actual depth.

Grid nodes were spaced 10m horizontally ranging from 1600m south to 1400 m north and 1700m west to 1700 m east of the source epicenter, and vertically every 5m at the grid edges.

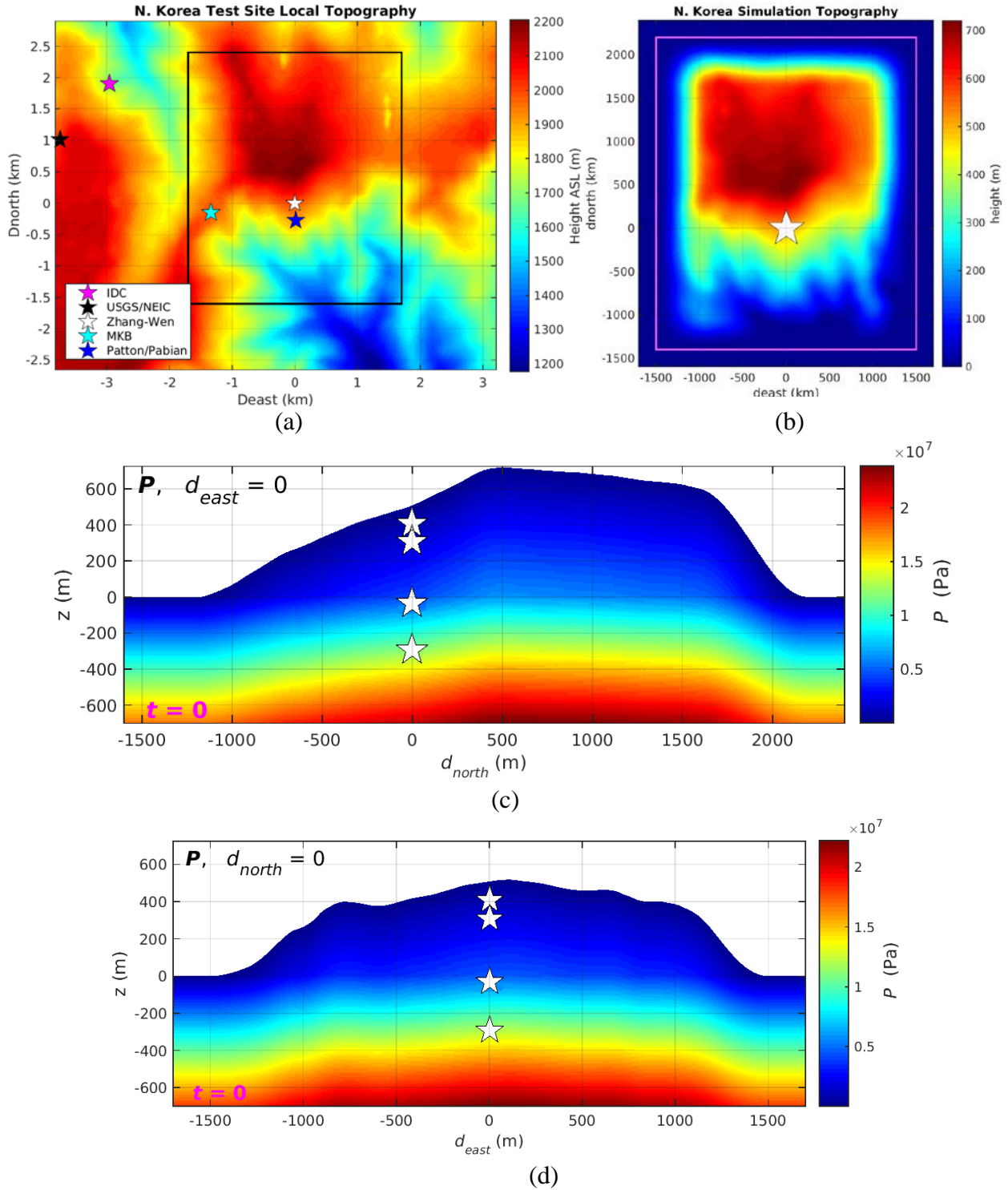


Figure 41. Topography near the North Korea test site. (a) shows the local topography in the area of the test site together with several estimated epicenters for the 2009 test. The location of Zhang and Wen (2013) is used for our simulations. The black line denotes the simulation area. Panel (b) shows the actual tapered topography used in the simulation. Panels (c) and (d) show south-north and west-east pressure profiles through the source epicenter.

4.4.1 Results

The figures on the following pages show the results of these calculations. They are divided into 4 sections – near field results, regional full-waveform seismograms, fundamental mode surface waves and far-field body waves. The near field results include snapshots of velocity in N-S and E-W cross-section, and regions of nonlinear deformation and cracking. Also included for each calculation are plots of outward final displacement on each vertical surface of the monitoring surface. As noted in section 4.3, these displacements are primarily responsible for surface wave generation.

Following is a summary of results from these calculations:

1. Regional P and S phases are affected by the mountain topography, causing amplification relative to the flat-layered case in the N-S directions and reduction relative to the flat-layered case in the E-W directions. For the shallowest two depths, regional P and S waves are reduced at azimuths near 45° , and are as large as or larger than the flat-layered case in other directions. Average difference in amplitude is small, but may be as large as a factor of two for some azimuths.
2. Long period surface waves are significantly affected by both topography and depth. In particular, surface waves are decreased substantially for shallow source depths, but increased significantly at the base of the mountain. This is strictly a long period effect, easily visible when waveforms are low-pass filtered at 15 seconds, but much less apparent for broadband waveforms.
3. Love waves are largest for the 100 meter depth, and there is also more Rayleigh wave variability for the 100 meter depth case.
4. Except for the moveout in pP arrival time, far-field P-waves are affected very little by either the NK topography or source depth. There is a slight reduction in P-wave amplitude at some azimuths for the shallowest two depths.
5. Topography causes generation of far-field SH comparable in amplitude to SV, and causes more variability in SV. SV is larger to the north for the shallowest two depths, and comparable to or smaller than SV from the planar model for other depths and directions.

4.4.2 Near Field Motion and Deformation

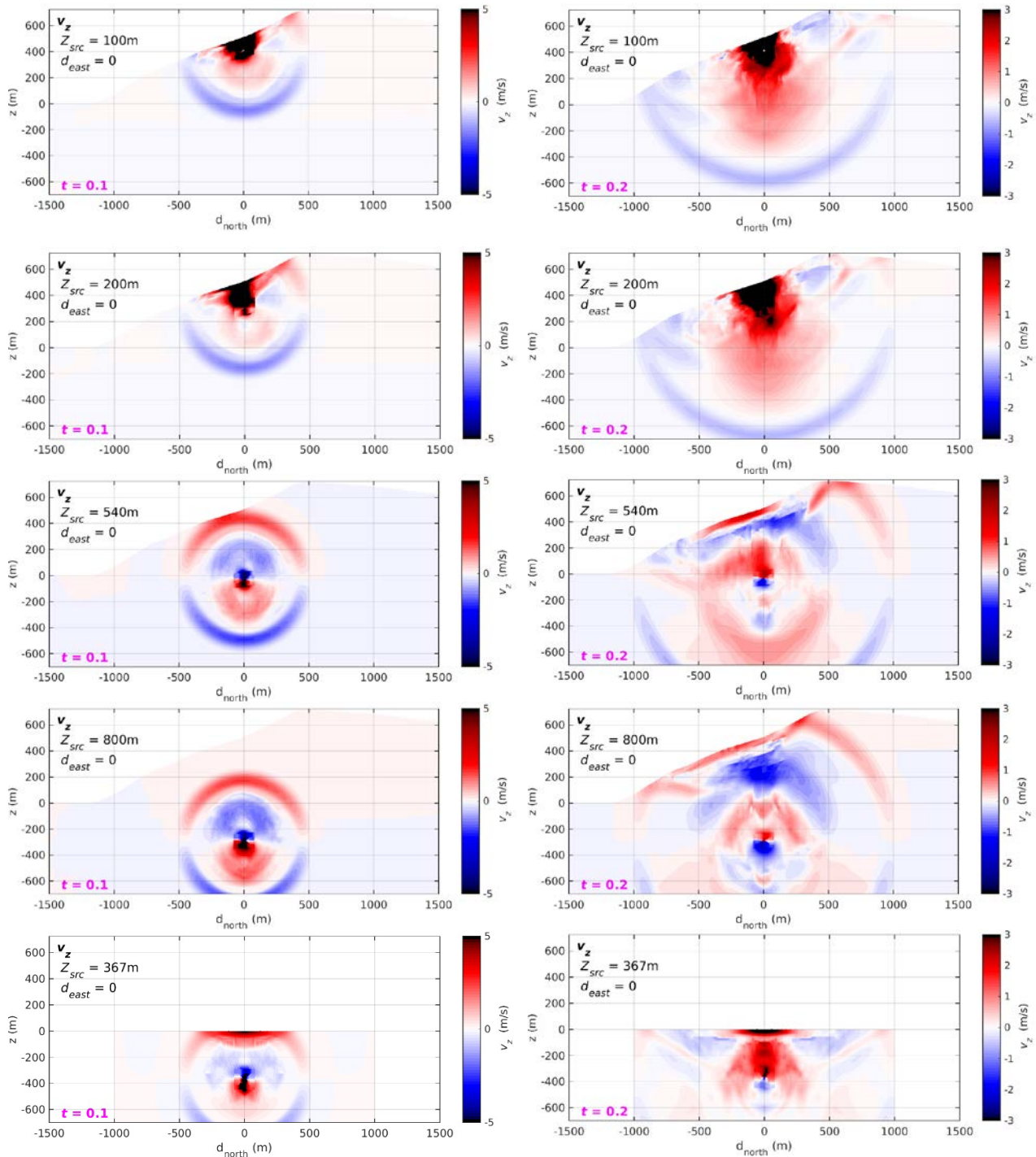


Figure 42. South-to-north profiles (through the source) of vertical velocity from 12.5 kt explosion simulations at four depths (100m, 200m, 540m, 800m respectively from the top) under sloping topography at the North Korea test site and the flat Shoal simulation (bottom): Left at 0.1 sec, right at 1.5 seconds.

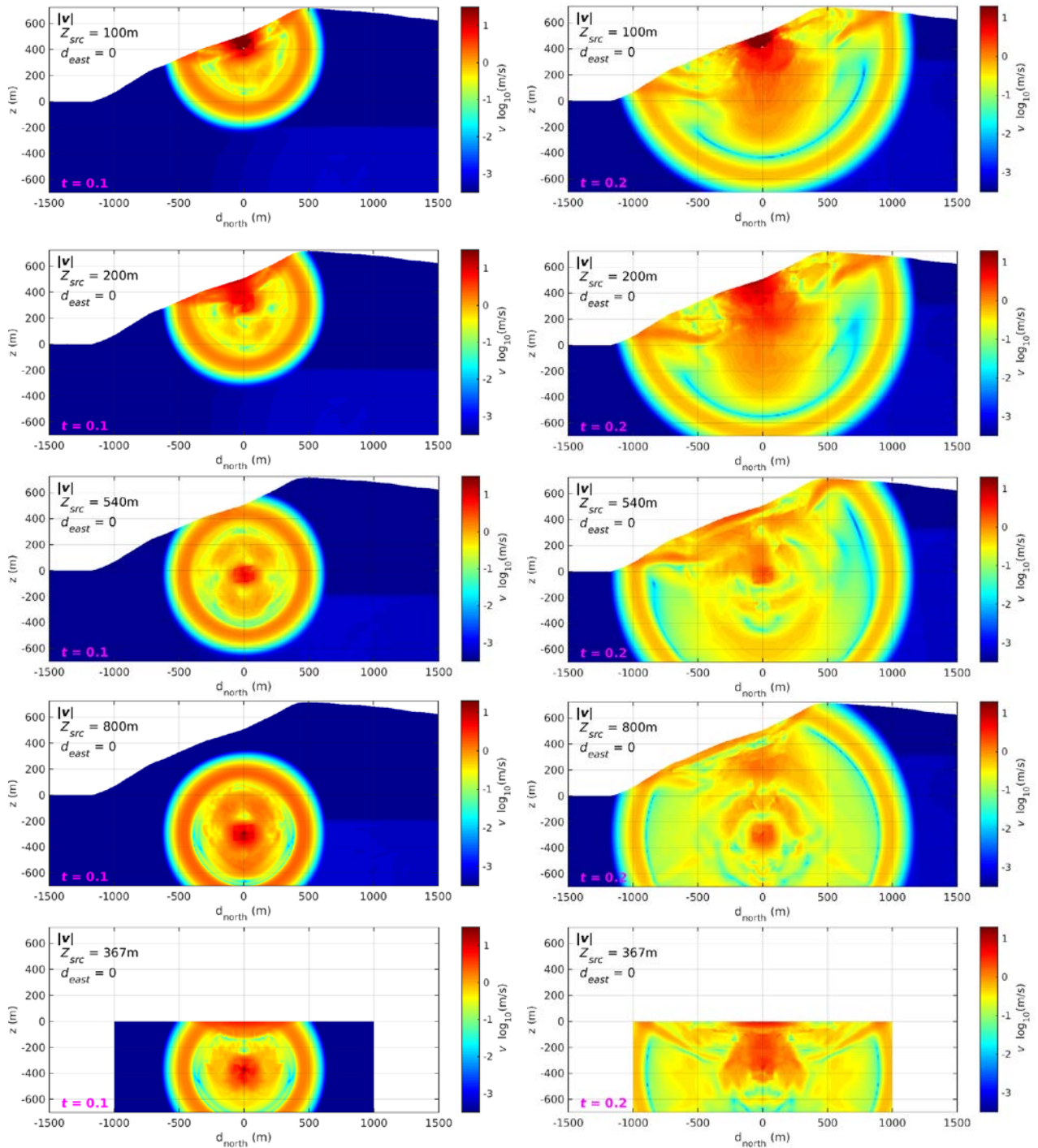


Figure 43. South-to-north profiles (through the source) of log-magnitude of velocity from 12.5 kt explosion simulations at four depths (100m, 200m, 540m, 800m respectively from the top) under sloping topography at the North Korea test site and the flat Shoal simulation (bottom): Left at 0.1 sec, right at 1.5 seconds.

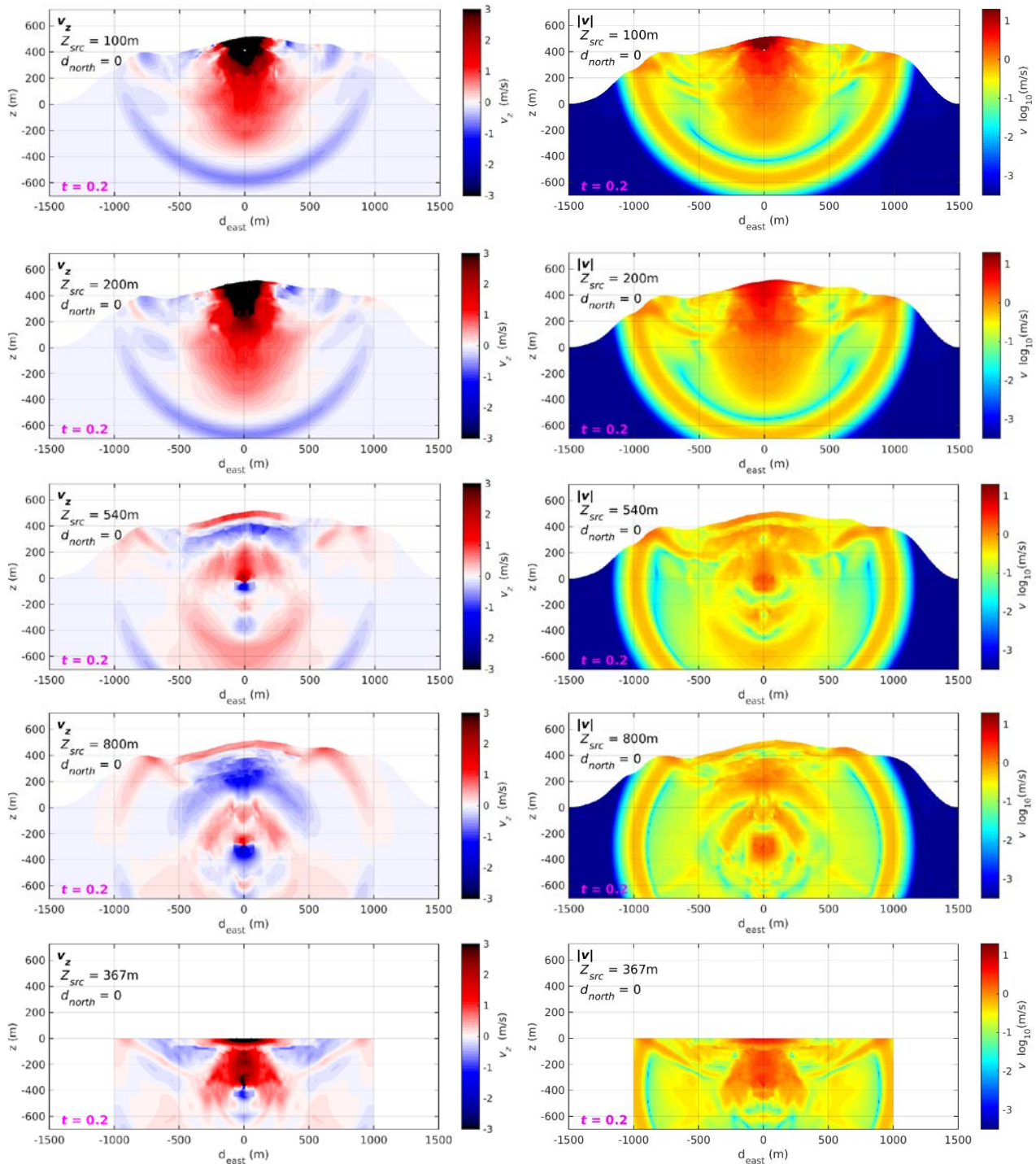


Figure 44. West-to-east profiles (through the source) of vertical velocity (left) and log-magnitude of velocity (right) at 0.2 sec. from 12.5 kt explosion simulations at four depths (100m, 200m, 540m, 800m respectively from the top) under sloping topography at the North Korea test site and the flat Shoal simulation (bottom).

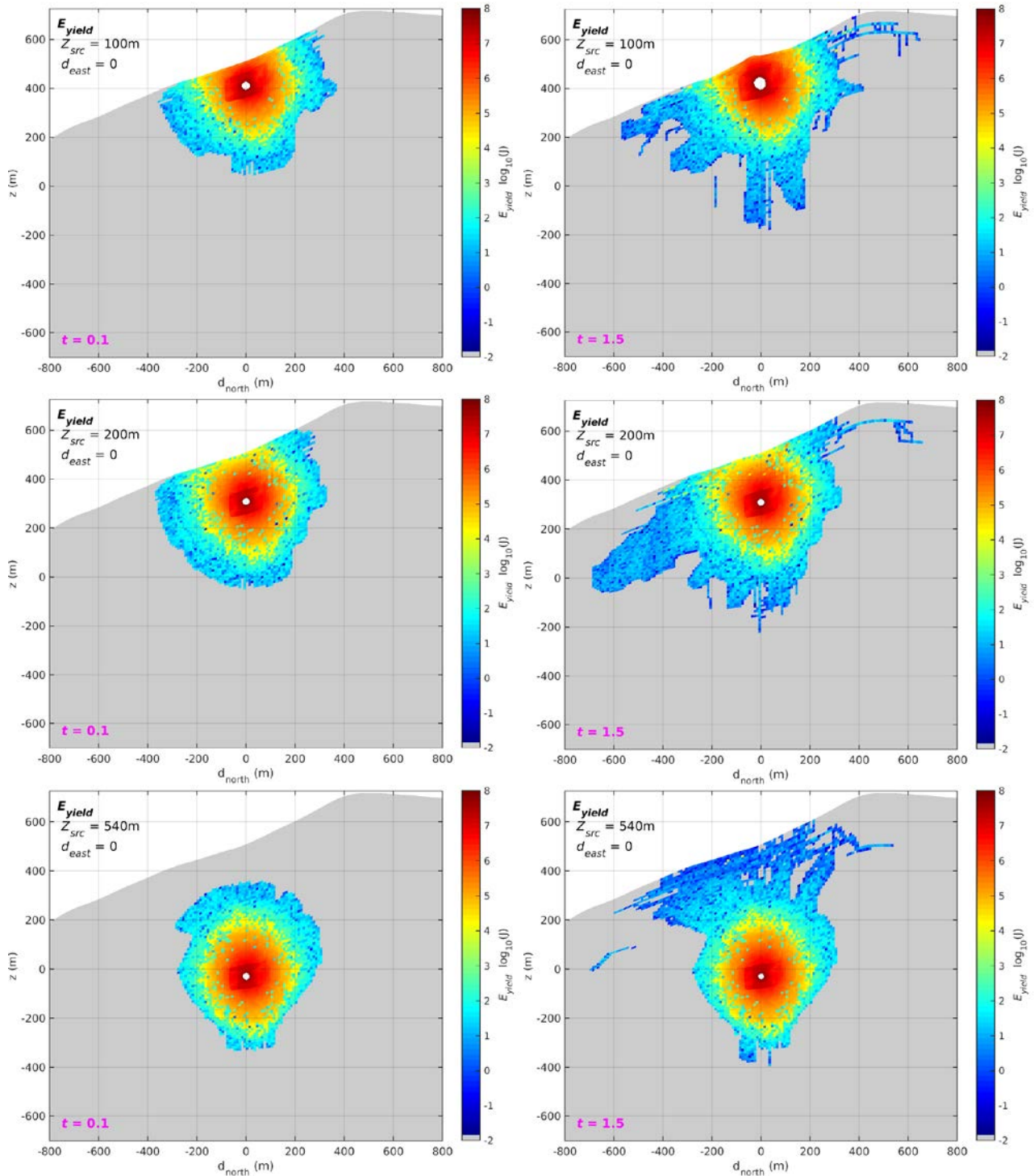


Figure 45. South-to-north profiles (through the source) of plastic work (energy of nonlinear yielding) from 12.5 kt explosion simulations at four depths (100m, 200m, 540m, 800m respectively from the top) under sloping topography at the North Korea test site, and the Shoal simulation (bottom): Left at 0.1 sec, right at 1.5 seconds.

Panel rows 1-3 on this page; panel rows 4 and 5 continued on the next page.

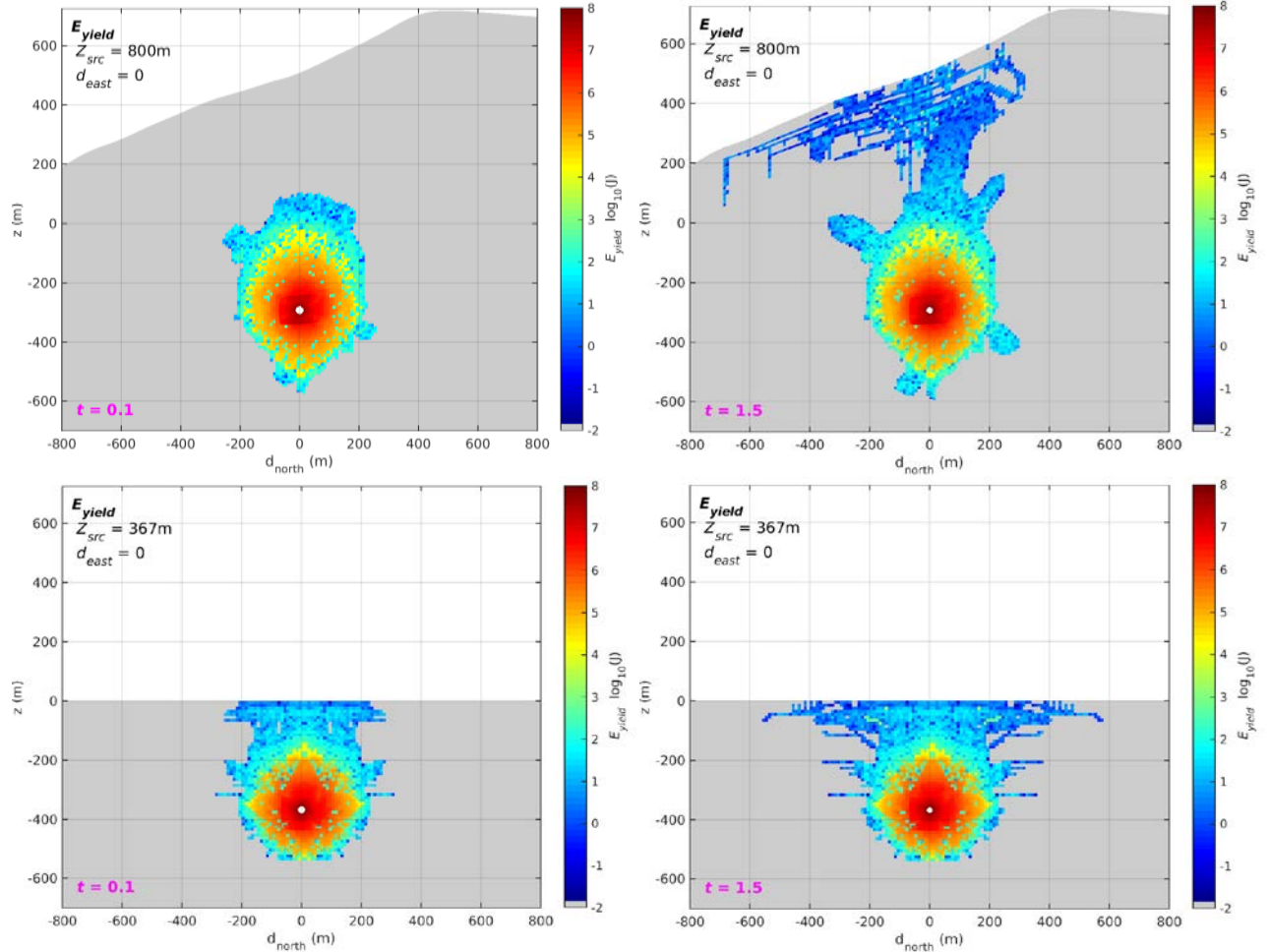


Figure 45. South-to-north profiles (through the source) of plastic work (energy of nonlinear yielding) from 12.5 kt explosion simulations at four depths (100m, 200m, 540m, 800m respectively from the top) under sloping topography at the North Korea test site, and the Shoal simulation (bottom): Left at 0.1 sec, right at 1.5 seconds. *Panel rows 4 and 5 on this page; panel rows 1-3 on the previous page.*

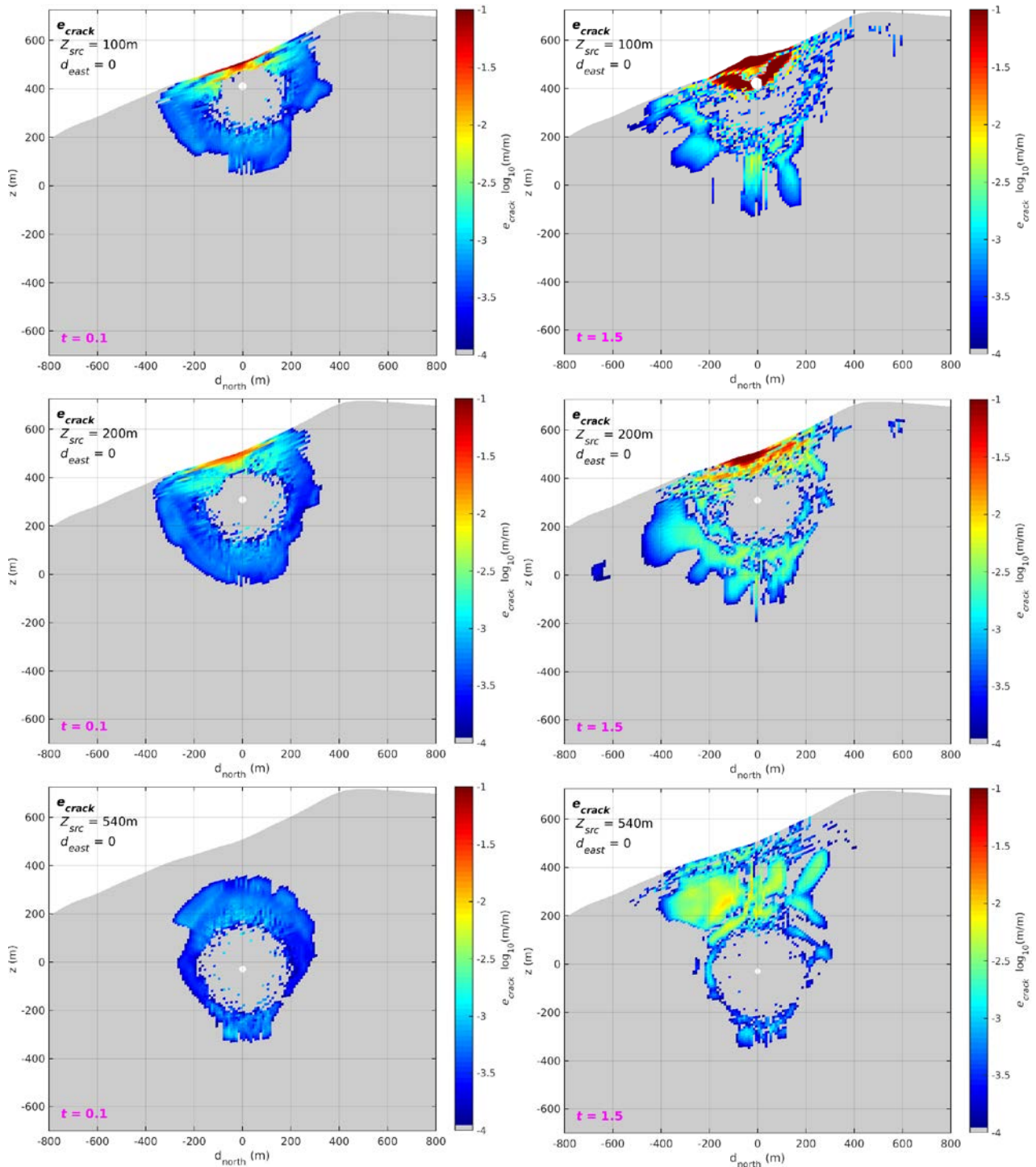


Figure 46. South-to-north profiles (through the source) of crack strain from 12.5 kt explosion simulations at four depths (100m, 200m, 540m, 800m respectively from the top) under sloping topography at the North Korea test site and the Shoal simulation (bottom): Left at 0.1 sec, right at 1.5 sec.

Panel rows 1-3 on this page; panel rows 4 and 5 continued on the next page.

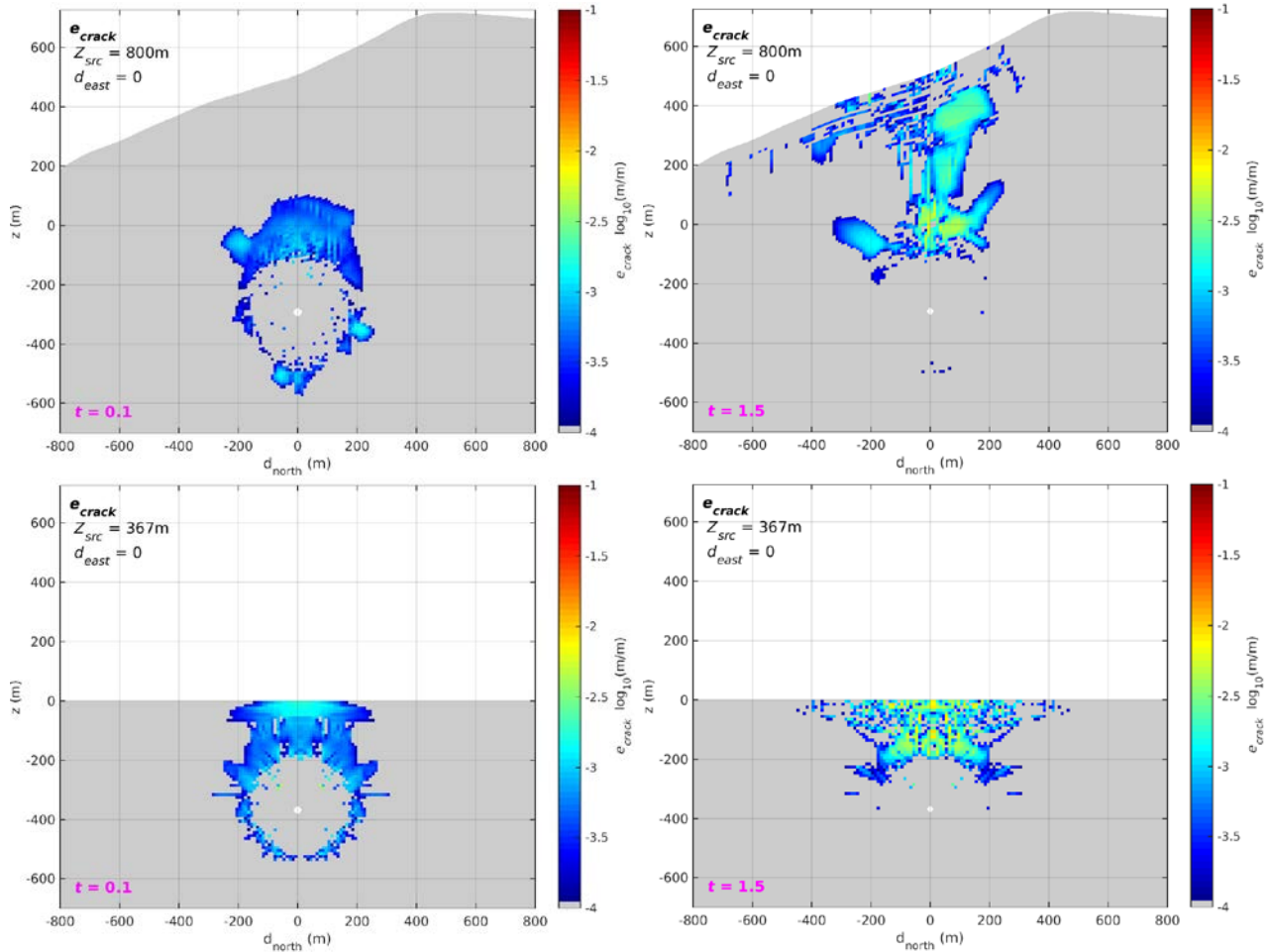


Figure 46. South-to-north profiles (through the source) of crack strain from 12.5 kt explosion simulations at four depths (100m, 200m, 540m, 800m respectively from the top) under sloping topography at the North Korea test site and the Shoal simulation (bottom): Left at 0.1 sec, right at 1.5 sec. *Panel rows 4 and 5 on this page; panel rows 1-3 on the previous page.*

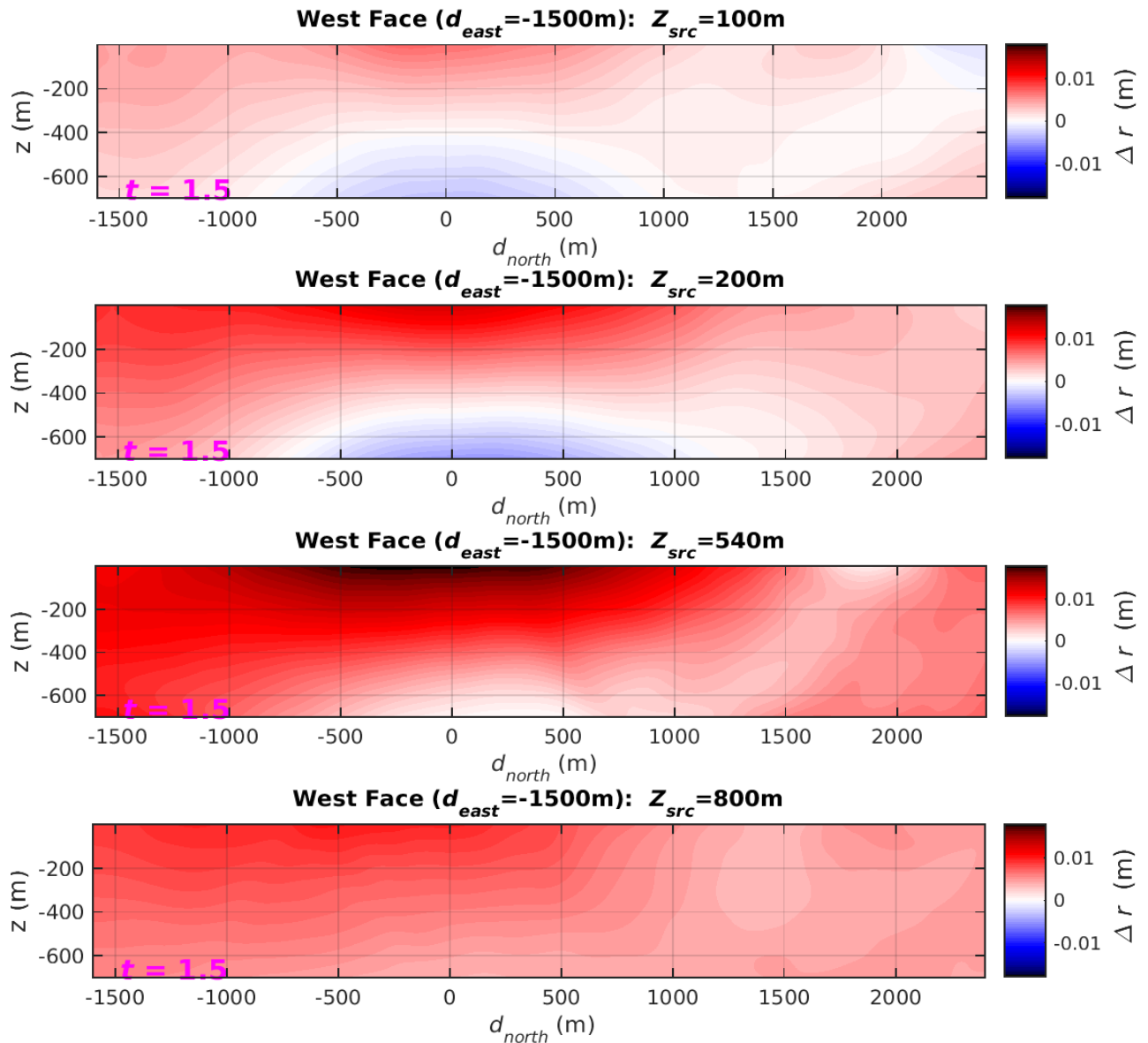


Figure 47. Outward displacement on the west monitoring surface at $d_{east} = -1500\text{m}$ from the source for the 3-D simulations of explosions at the North Korea test site with source depths (from top to bottom) of 100, 200, 540, and 800 m.

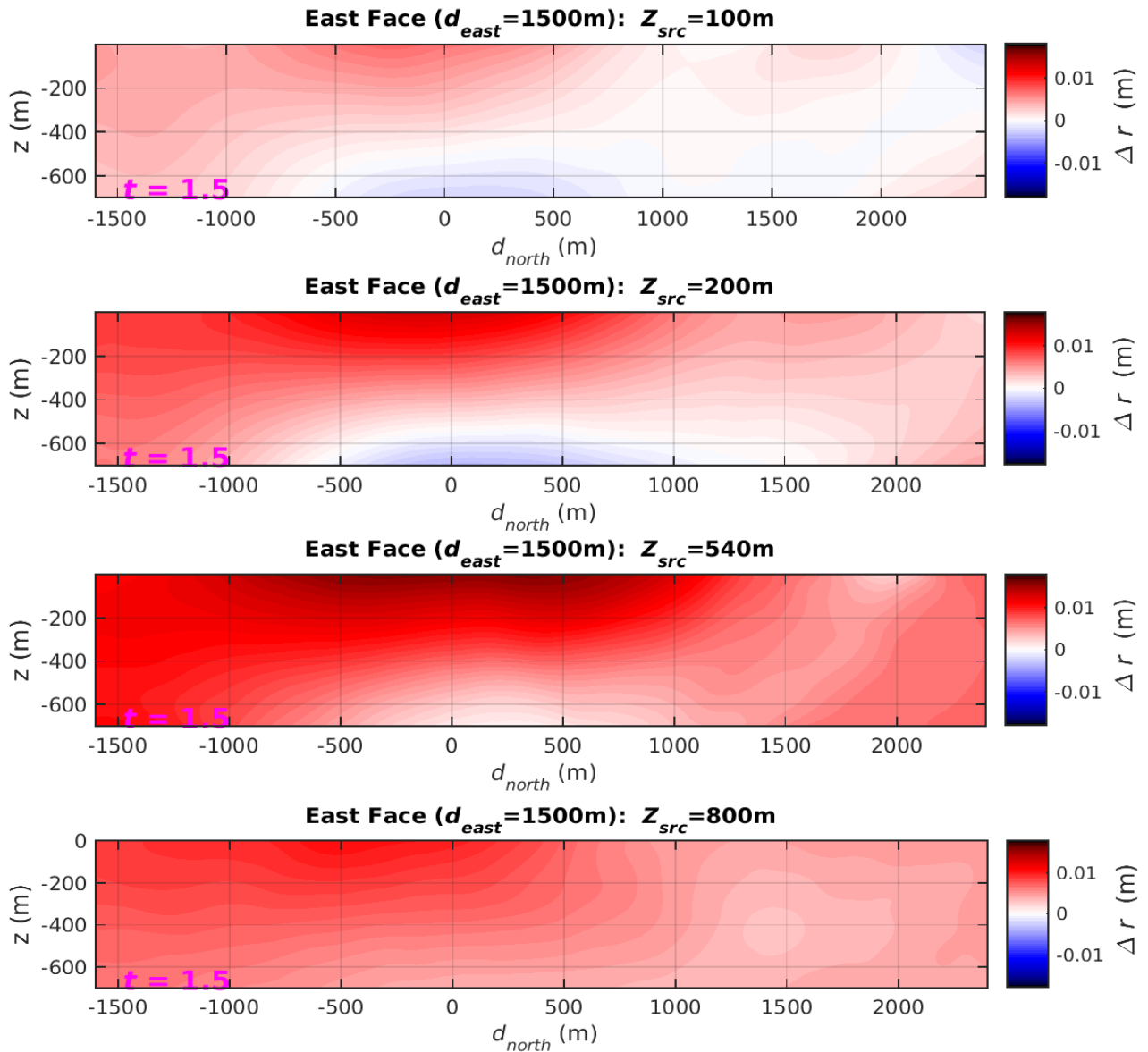


Figure 48. Outward displacement on the east monitoring surface at $d_{east} = 1500\text{m}$ from the source for the 3-D simulations of explosions at the North Korea test site with source depths (from top to bottom) of 100, 200, 540, and 800 m.

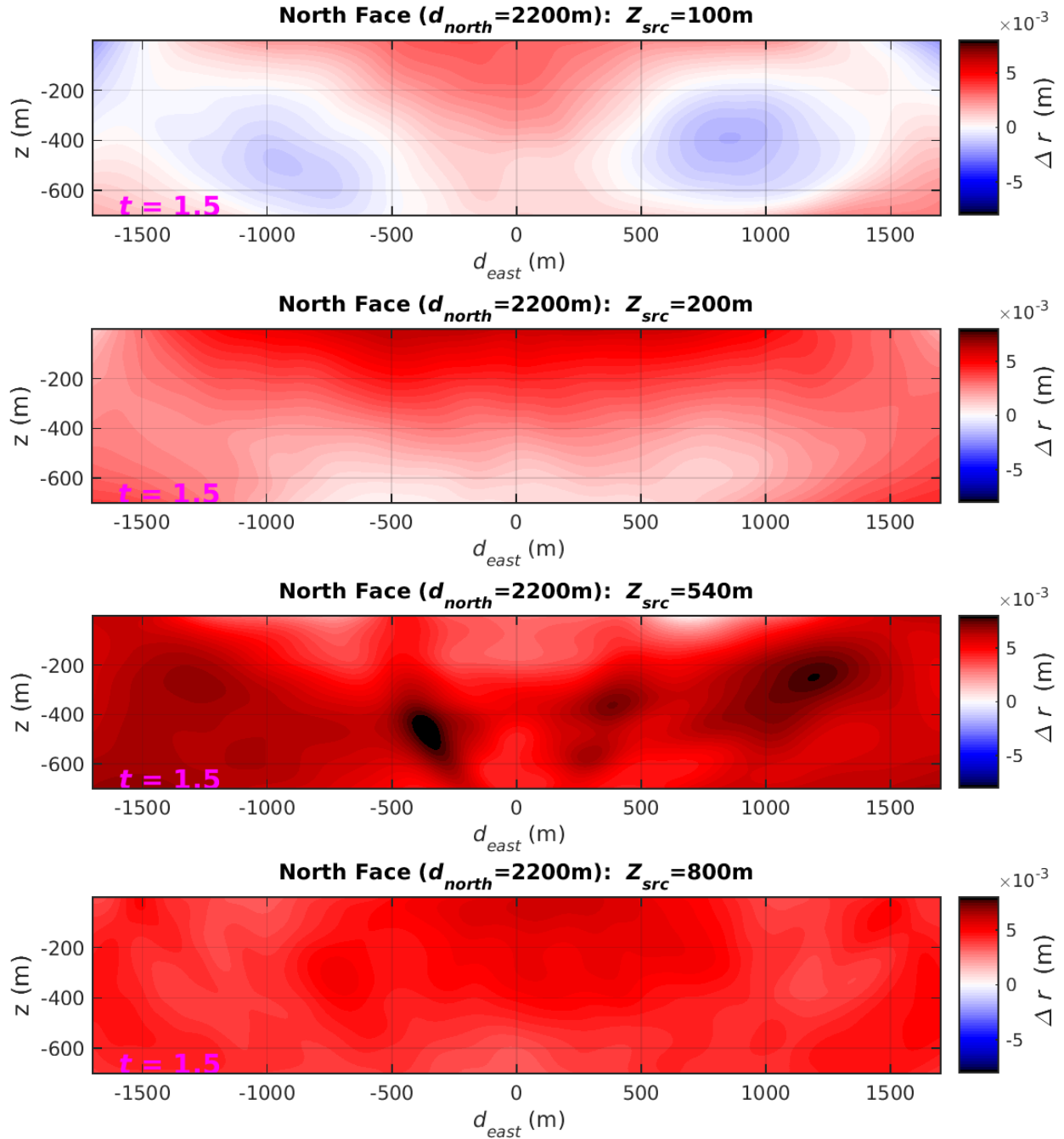


Figure 49. Outward displacement on the north monitoring surface at $d_{east} = 1500\text{m}$ from the source for the 3-D simulations of explosions at the North Korea test site with source depths (from top to bottom) of 100, 200, 540, and 800 m.

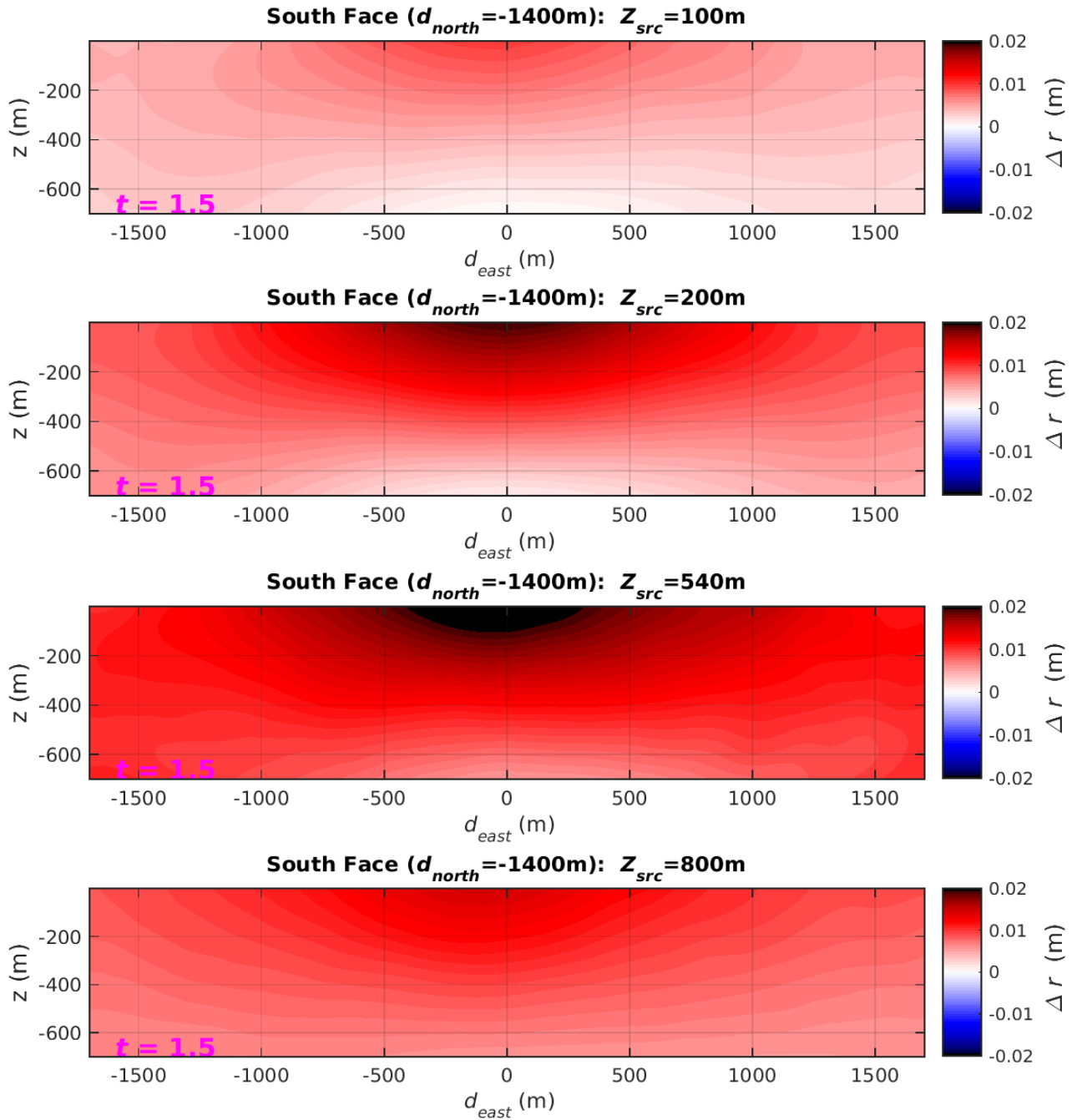


Figure 50. Outward displacement on the south monitoring surface at $d_{north} = -1400$ m from the source for the 3-D simulations of explosions at the North Korea test site with source depths (from top to bottom) of 100, 200, 540, and 800 m.

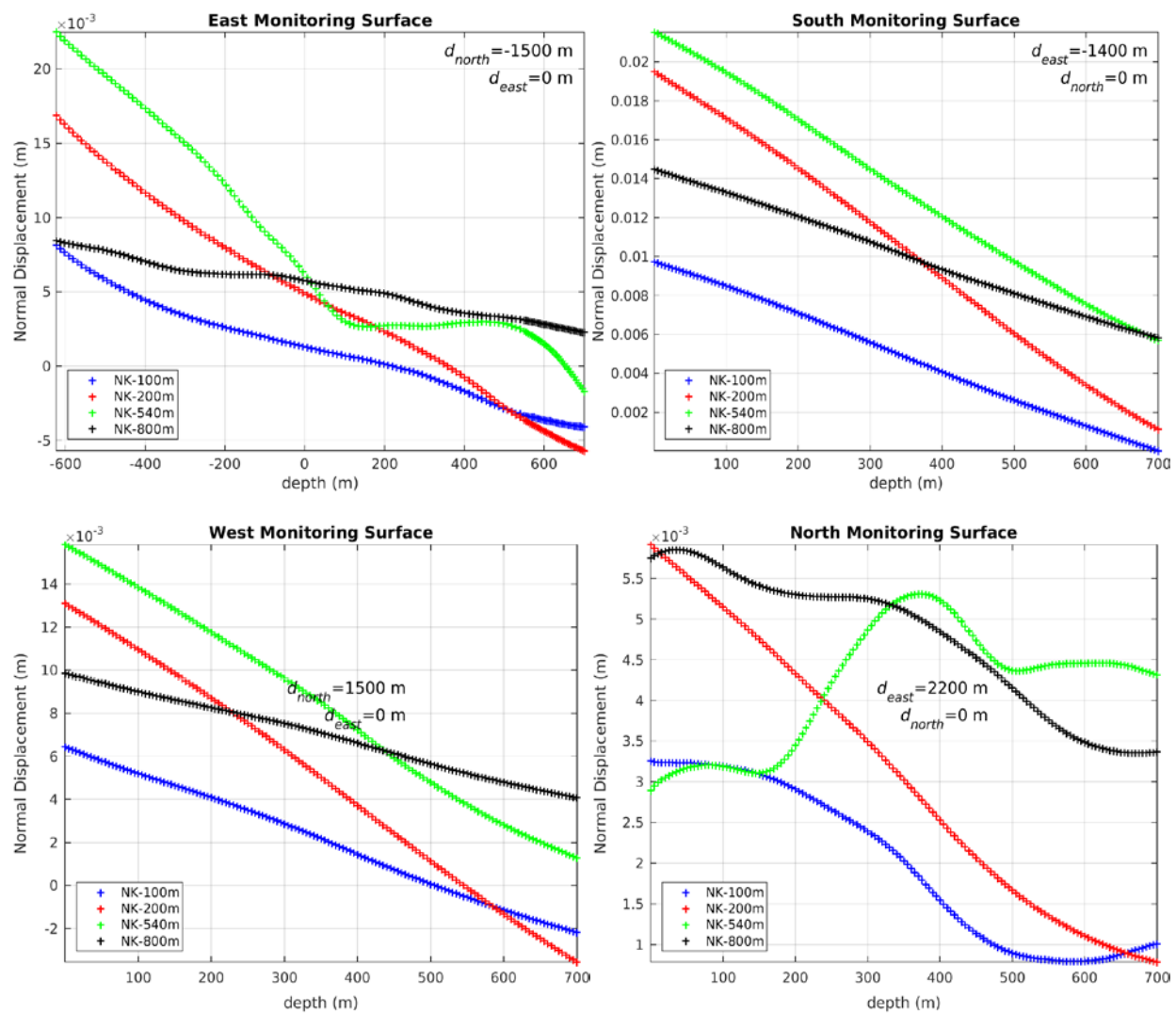


Figure 51. Profiles of final outward normal displacement on the monitoring surface faces due west, east, south, and north of the North Korea simulation sources.

4.4.3 Regional Waveforms

In this section we show comparisons of regional waveforms at 250 km distance from the North Korea and Shoal calculations. Figure 52 to Figure 56 show a comparison of the regional waveforms from the Shoal and North Korea calculations. Note that both the Shoal and North Korea calculations shown here were propagated with the North Korea structure listed in Table 5 rather than the Western US structure used earlier for the Shoal and Slope calculations. In all of these calculations, the azimuth shown is true azimuth measured clockwise from North (Figure 41).

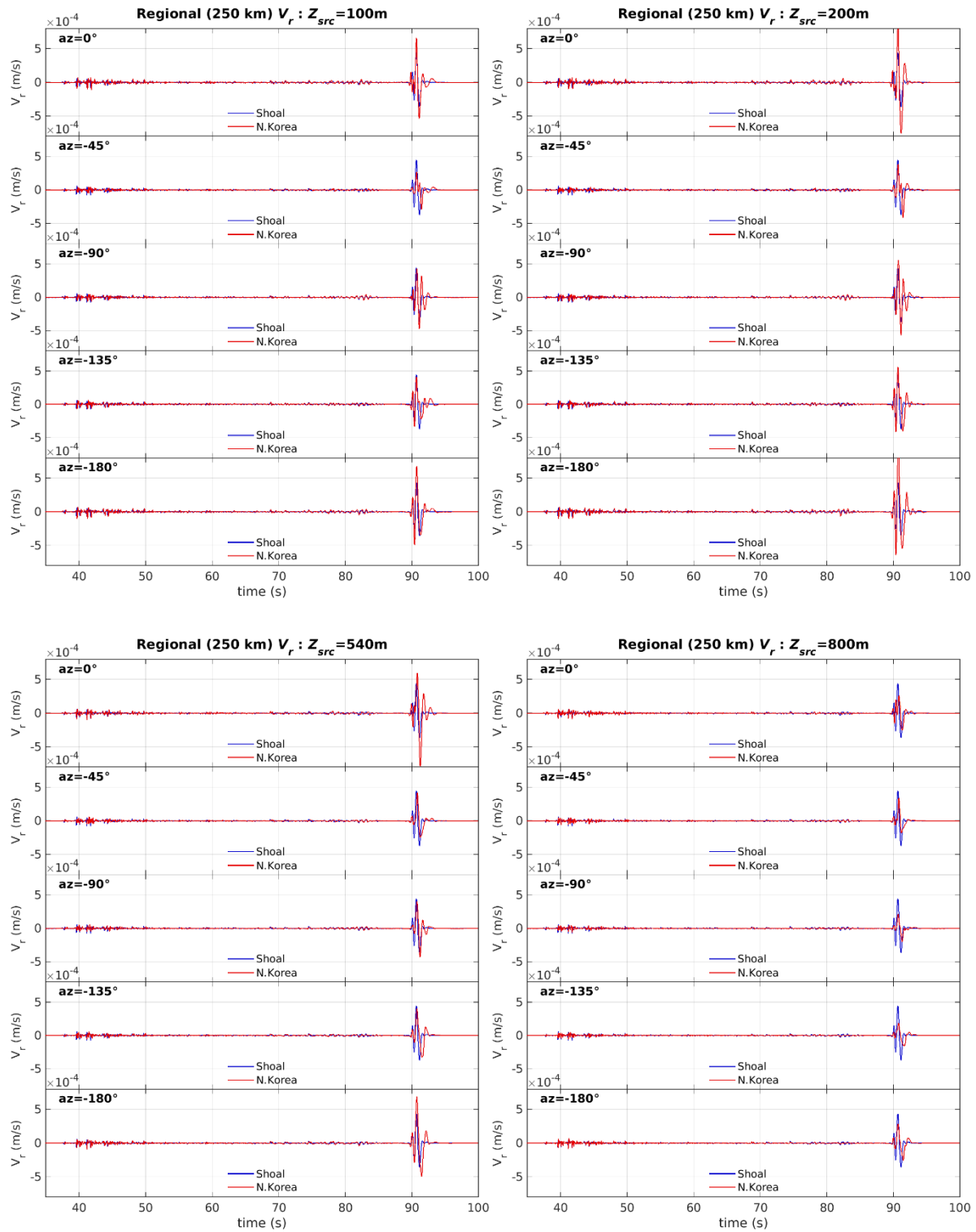


Figure 52. Full-waveform radial velocity at 250 km and azimuths of 0, -45, -90, -135 and -180 degrees from the North Korea simulations with source depths of 100, 200, 540 and 800m (red) and the Shoal simulations at 367 m below a flat surface (blue).

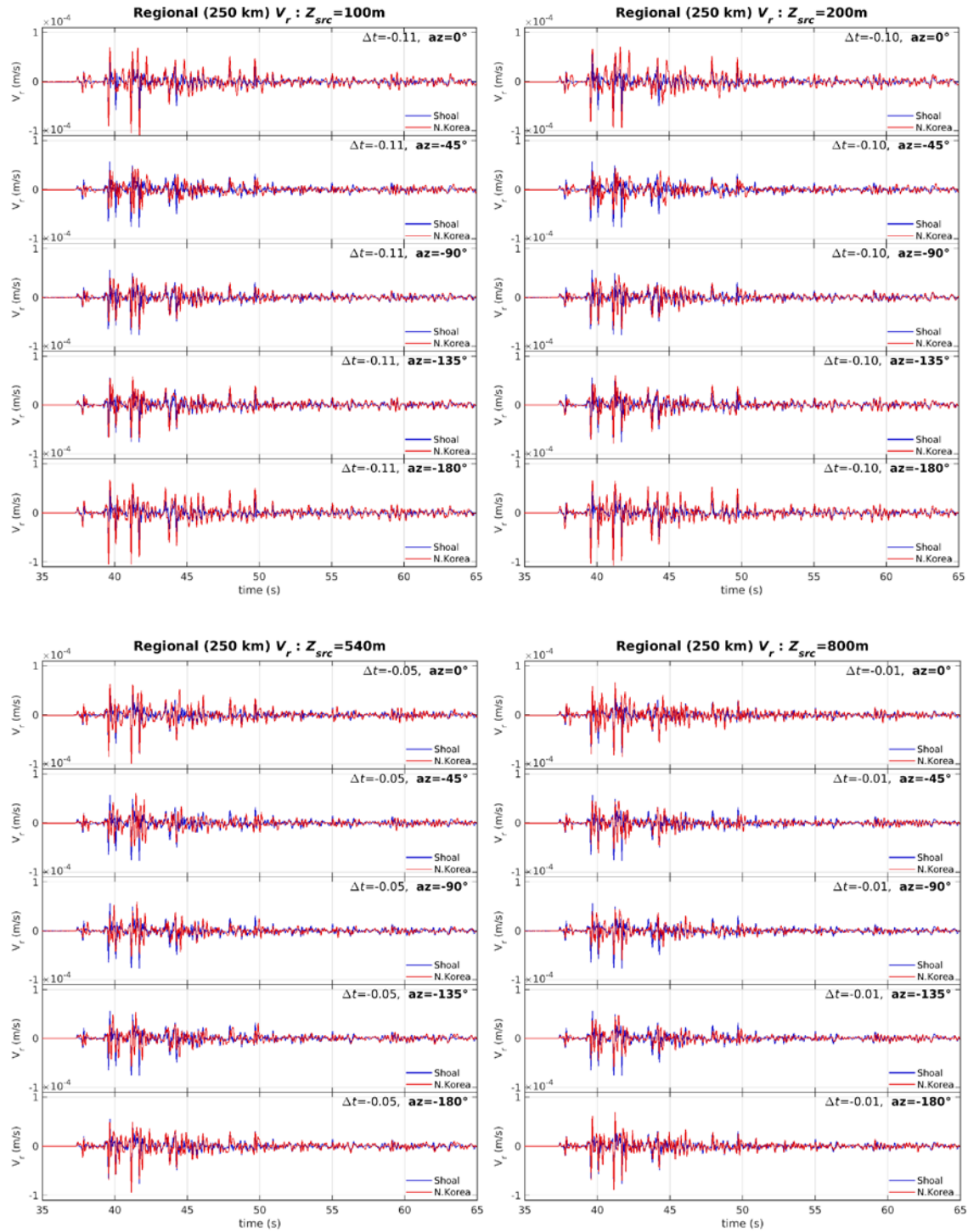


Figure 53. Full-waveform vertical velocity at 250 km and azimuths of 0, -45, -90 -135 and -180 degrees from the North Korea simulations with source depths of 100, 200, 540 and 800m (red) and the Shoal simulations at 367 m below a flat surface (blue). *NK travel times were reduced by amounts indicated at the top right of each frame to attain time alignment with the Shoal waveforms. This figure shows the early part of the Figure 52 waveforms.*

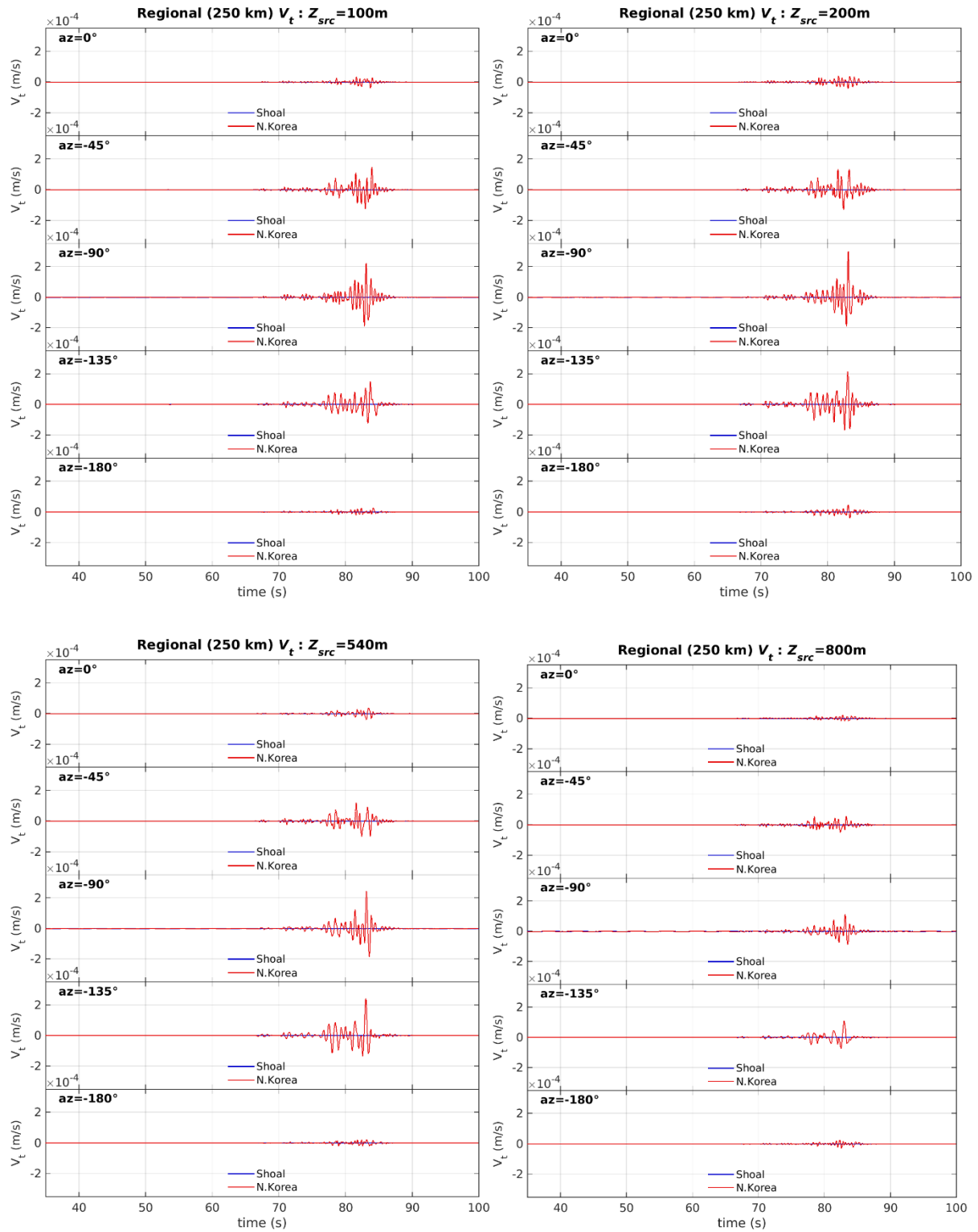


Figure 54. Full-waveform tangential velocity at 250 km and azimuths of 0, -45, -90 -135 and -180 degrees from the North Korea simulations with source depths of 100, 200, 540 and 800m (red) and the Shoal simulations at 367 m below a flat surface (blue).

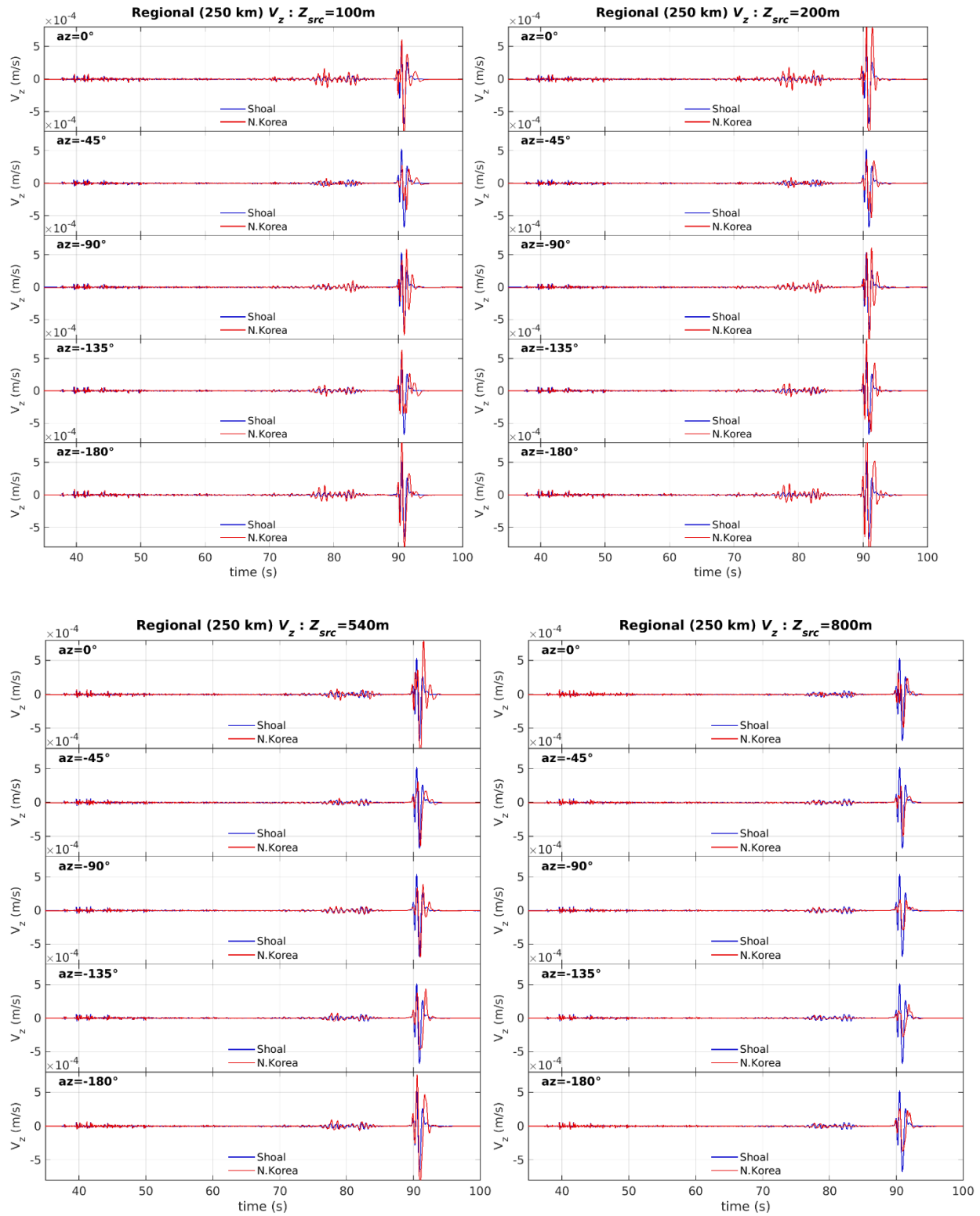


Figure 55. Full-waveform vertical velocity at 250 km and azimuths of 0, -45, -90 -135 and -180 degrees from the North Korea simulations with source depths of 100, 200, 540 and 800m (red) and the Shoal simulations at 367 m below a flat surface (blue).

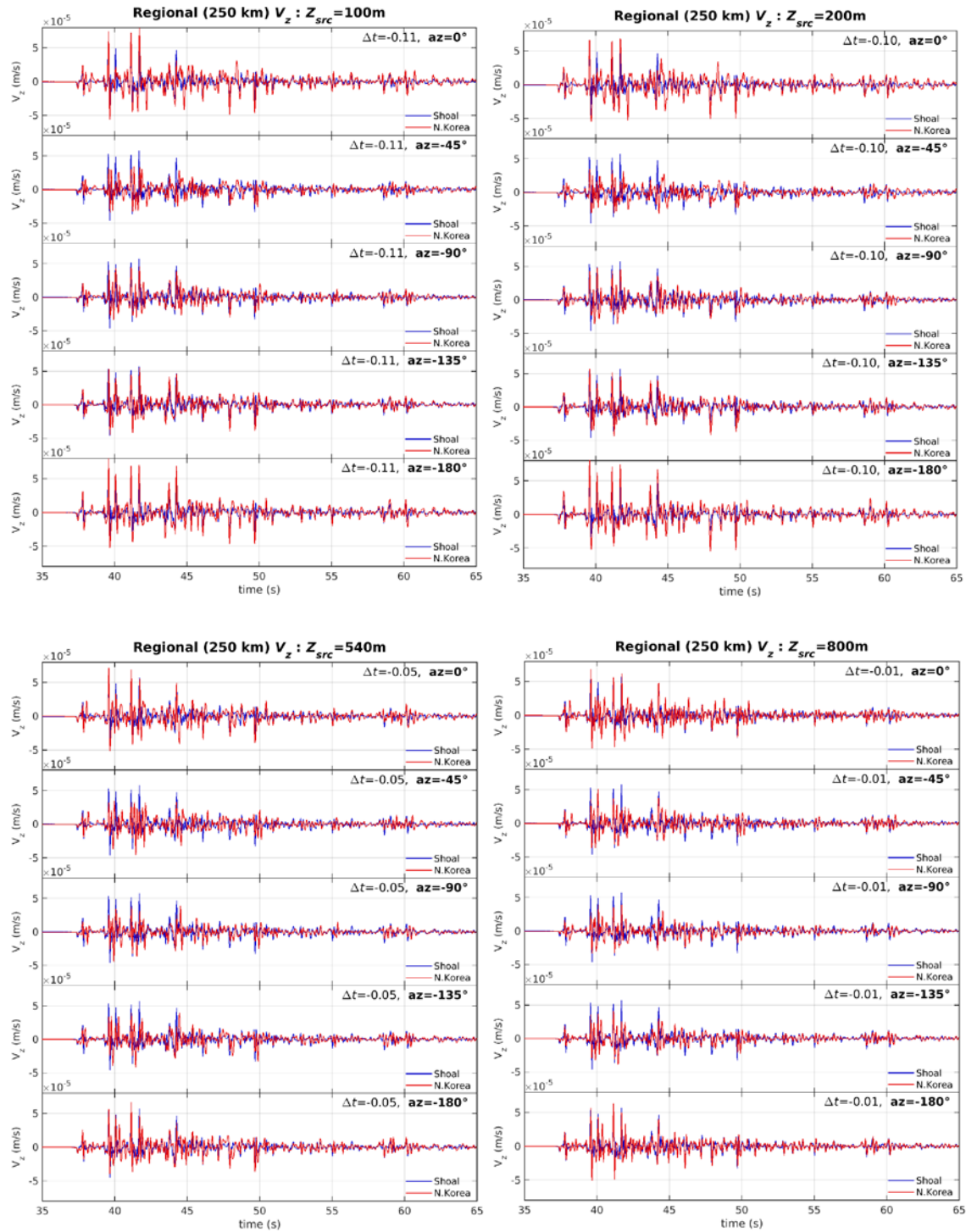


Figure 56. Full-waveform vertical velocity at 250 km and azimuths of 0, -45, -90 -135 and -180 degrees from the North Korea simulations with source depths of 100, 200, 540 and 800m (red) and the Shoal simulations at 367 m below a flat surface (blue). *NK travel times were reduced by amounts indicated at the top right of each frame to attain time alignment with the Shoal waveforms. This figure shows the early part of the Figure 55 waveforms.*

4.4.4 Surface Waves

In this section we show comparisons of long period fundamental mode surface waves (Rayleigh and Love) at 2000 km distance from the Shoal and North Korea calculations, again all propagated with the North Korea structure listed in Table 5. Note that there is only a single Shoal calculation at 370 meters depth, so it does not change with the depth of the North Korean calculations. Figure 58, Figure 59 and Figure 60 show the broadband fundamental mode surface wave for the radial, tangential and vertical components, respectively. Figure 61, Figure 62 and Figure 63 show the same waveforms low-pass filtered at 15 seconds. As with the regional waveforms, the azimuth shown is true azimuth measured clockwise from North (Figure 41). Figure 57 shows M_s calculated from the vertical component for all surface waves. At the shallowest depth, there is considerable variability with azimuth. Surface waves from deeper events show amplification with a peak at the 540 meter depth. This is most likely because the pressure and horizontal stress at a depth beneath the top of a mountain are lower than at the same depth in a flat structure.

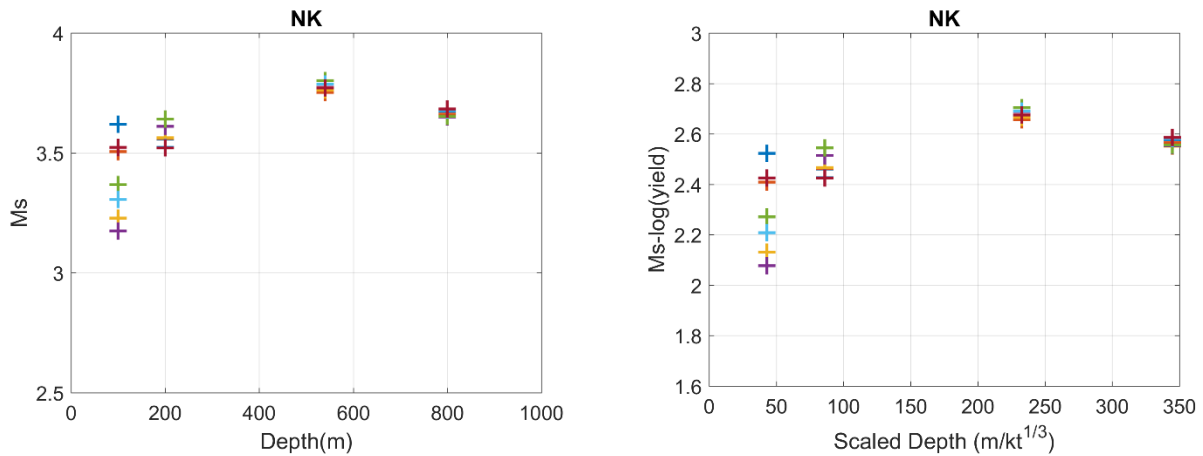


Figure 57. Left: M_s vs depth for calculated surface waves. Right: $M_s - \log(\text{yield})$ vs. scaled depth.

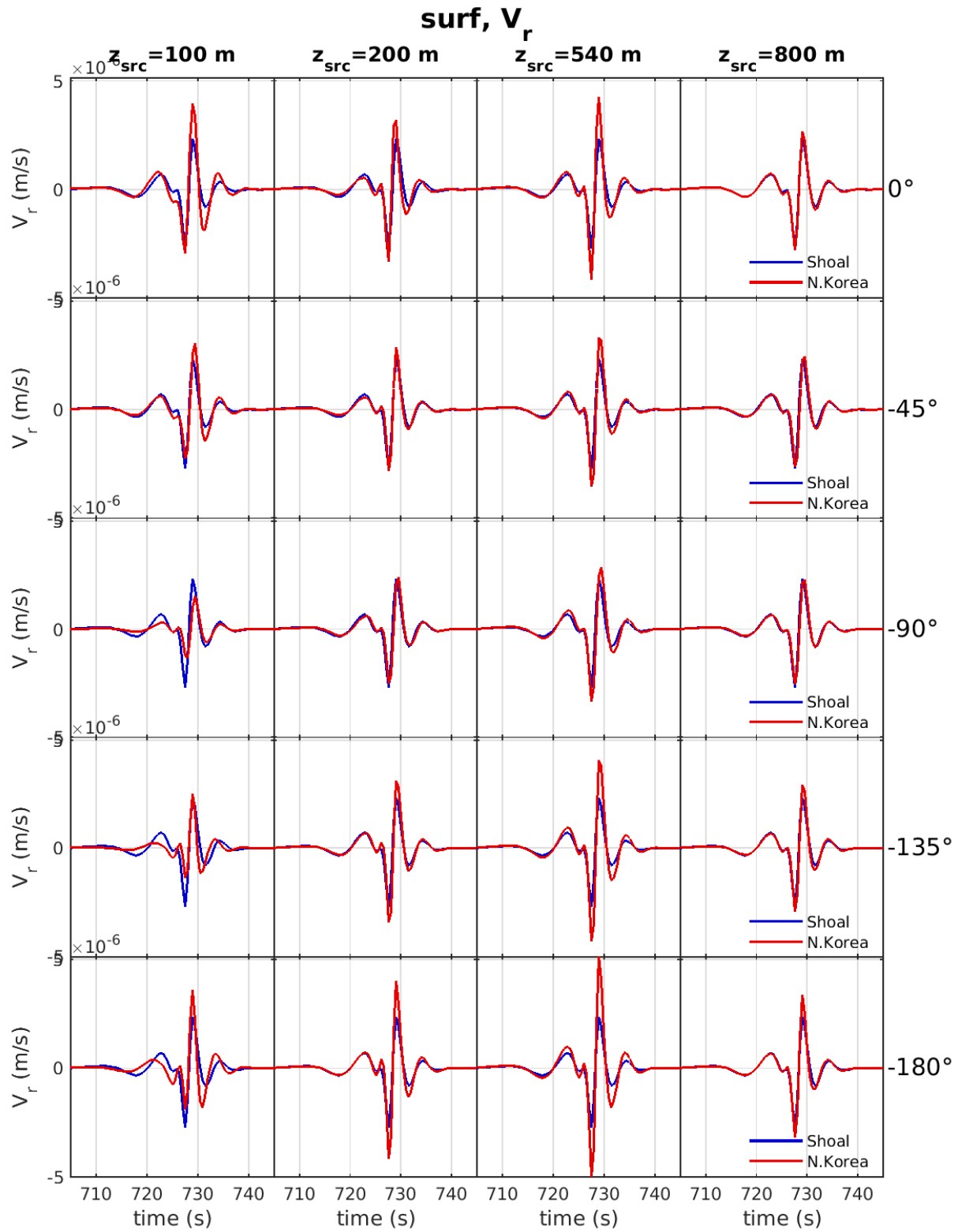


Figure 58. Surface wave radial velocity at 2000km.

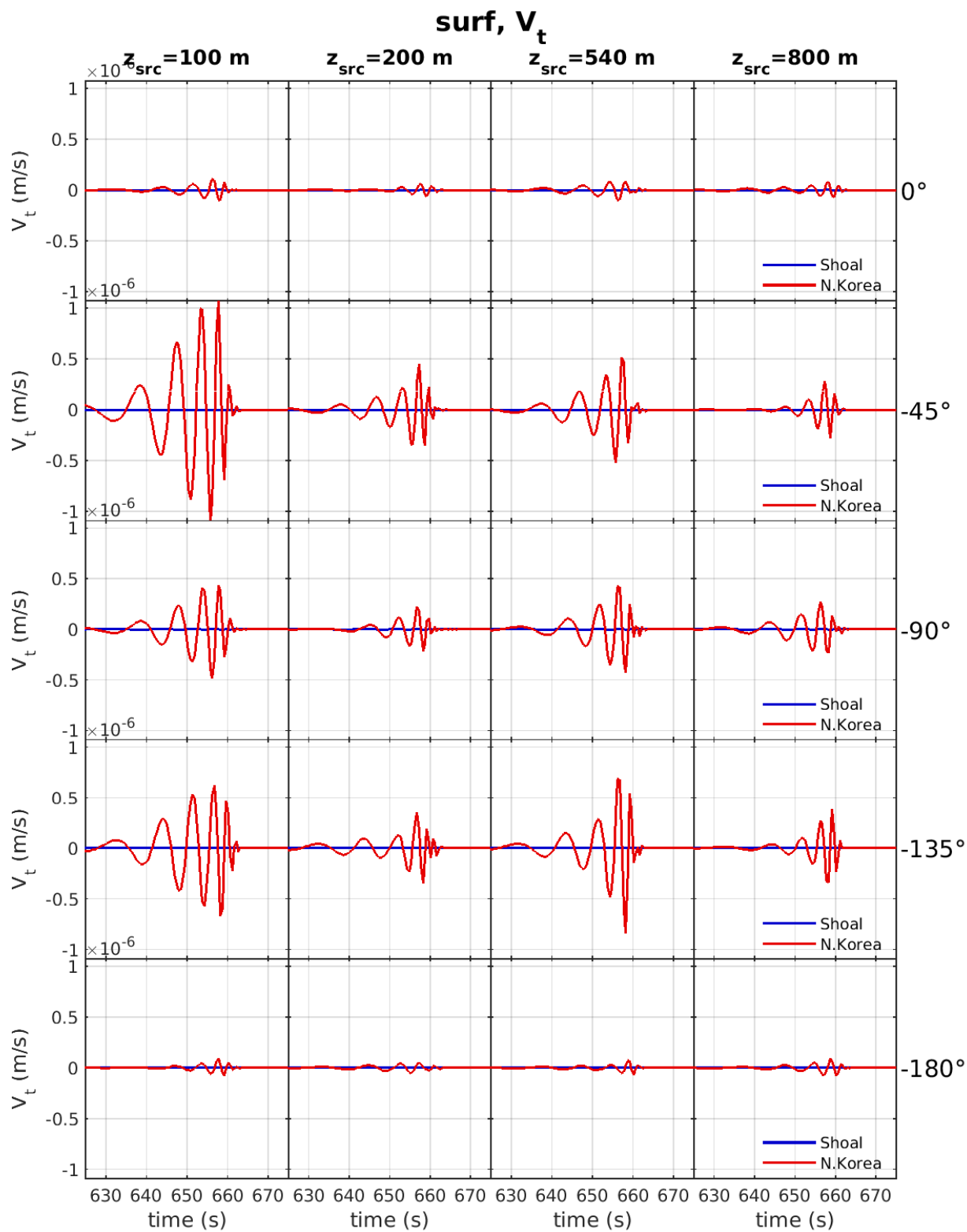


Figure 59. Surface wave tangential velocity at 2000km.

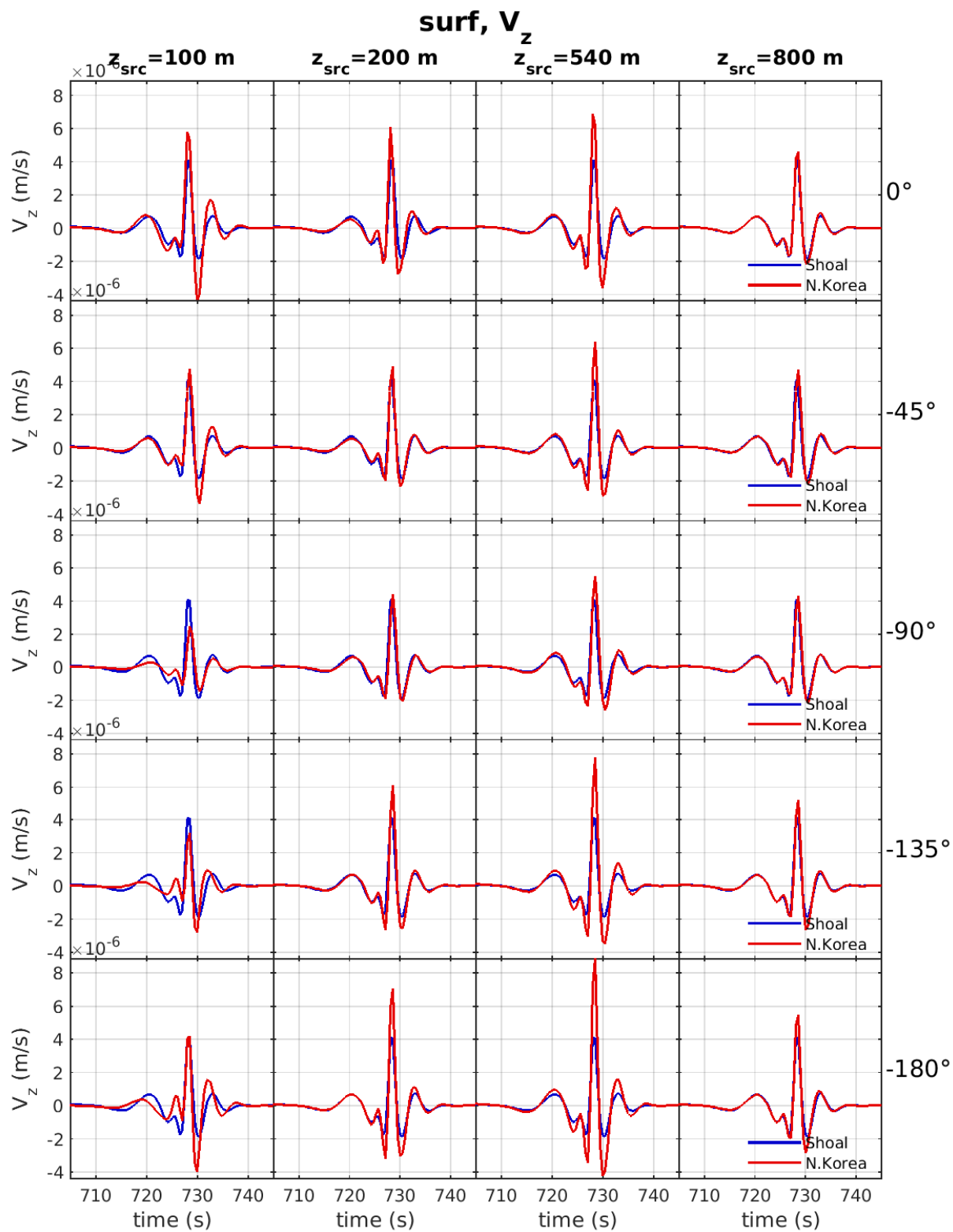


Figure 60. Surface wave vertical velocity at 2000km.

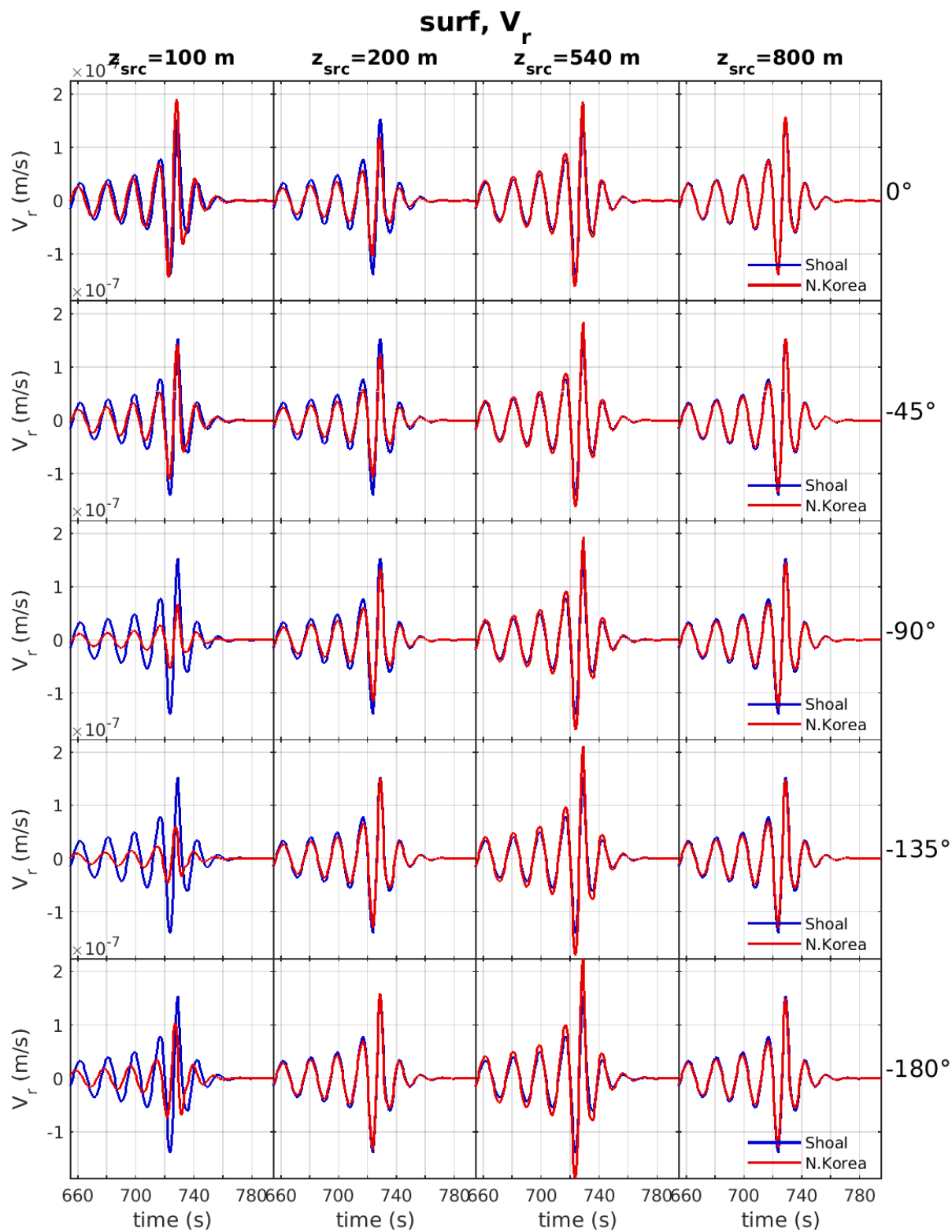


Figure 61. Surface wave radial velocity at 2000km, low-pass filtered at 15 sec.

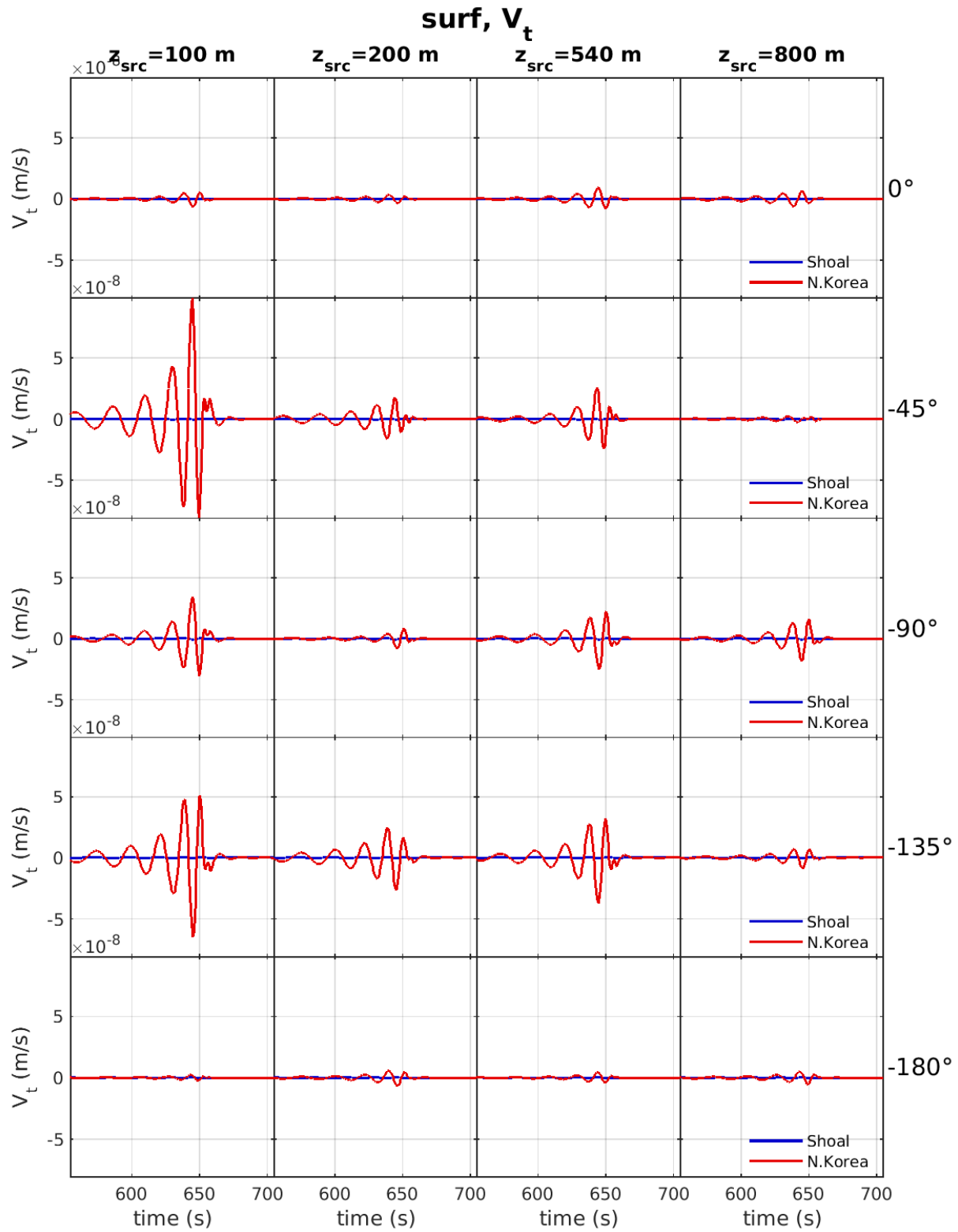


Figure 62. Surface wave tangential velocity at 2000km, low-pass filtered at 15 sec.

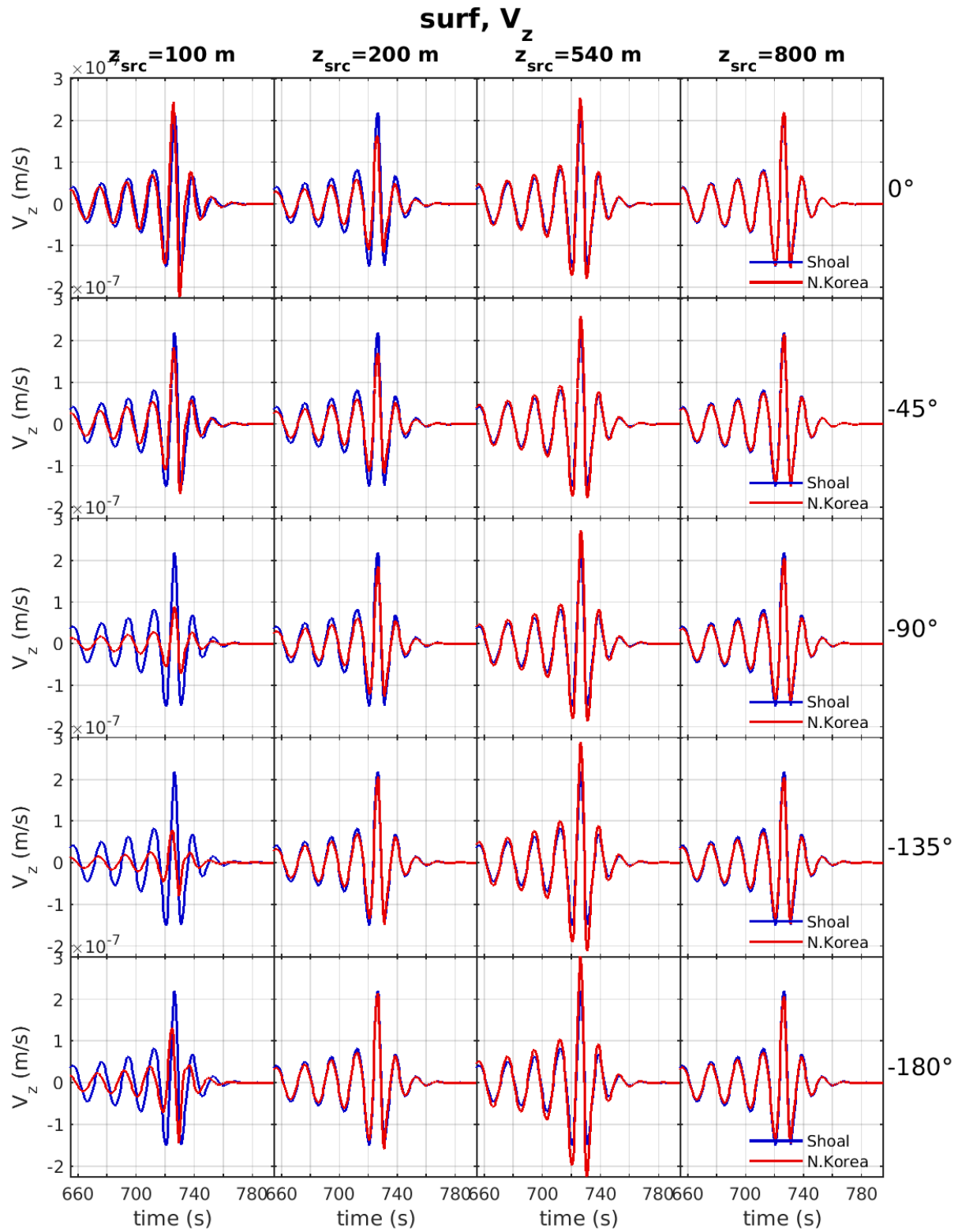


Figure 63. Surface wave vertical velocity at 2000km, low-pass filtered at 15 sec.

4.4.5 Body Waves

In this section we show far field P and S body waves from the Shoal and North Korea simulations, calculated for the regional structure of Table 5 at 1000 km from the source. In each figure, waveforms are plotted for each source depth along rows and for azimuths from north counter clockwise to south in steps of 45 deg. All waves were computed for a takeoff angle of 20°. P-waves for the North Korea simulations were time advanced to approximate alignment with the main Shoal arrival, by a moveout equivalent to the travel time through the NK-Shoal difference in source depth relative to the 1-D surface level at a slowness of 1/2000m/s.

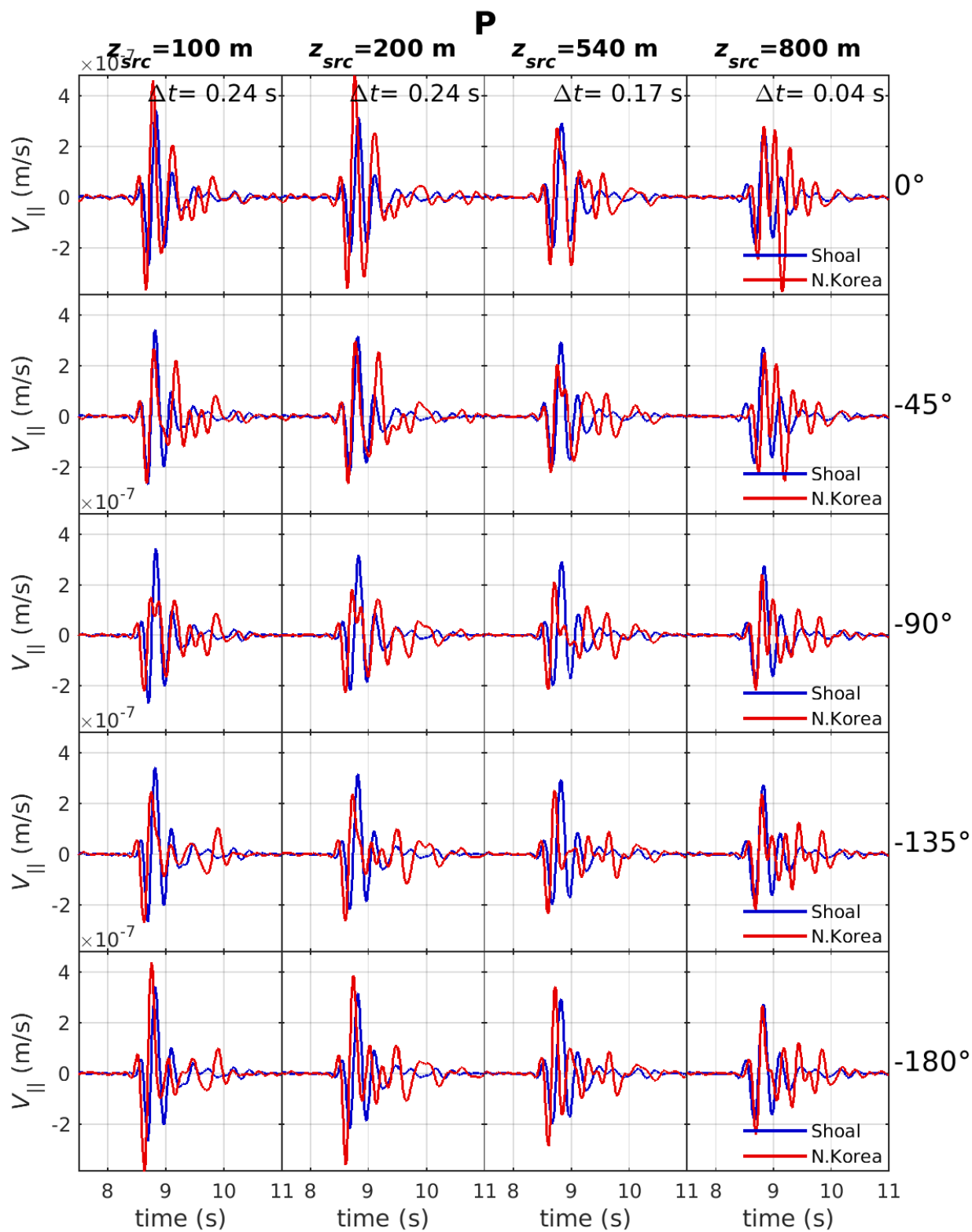


Figure 64. Far-field P-wave at 1000km for Shoal and North Korea simulations

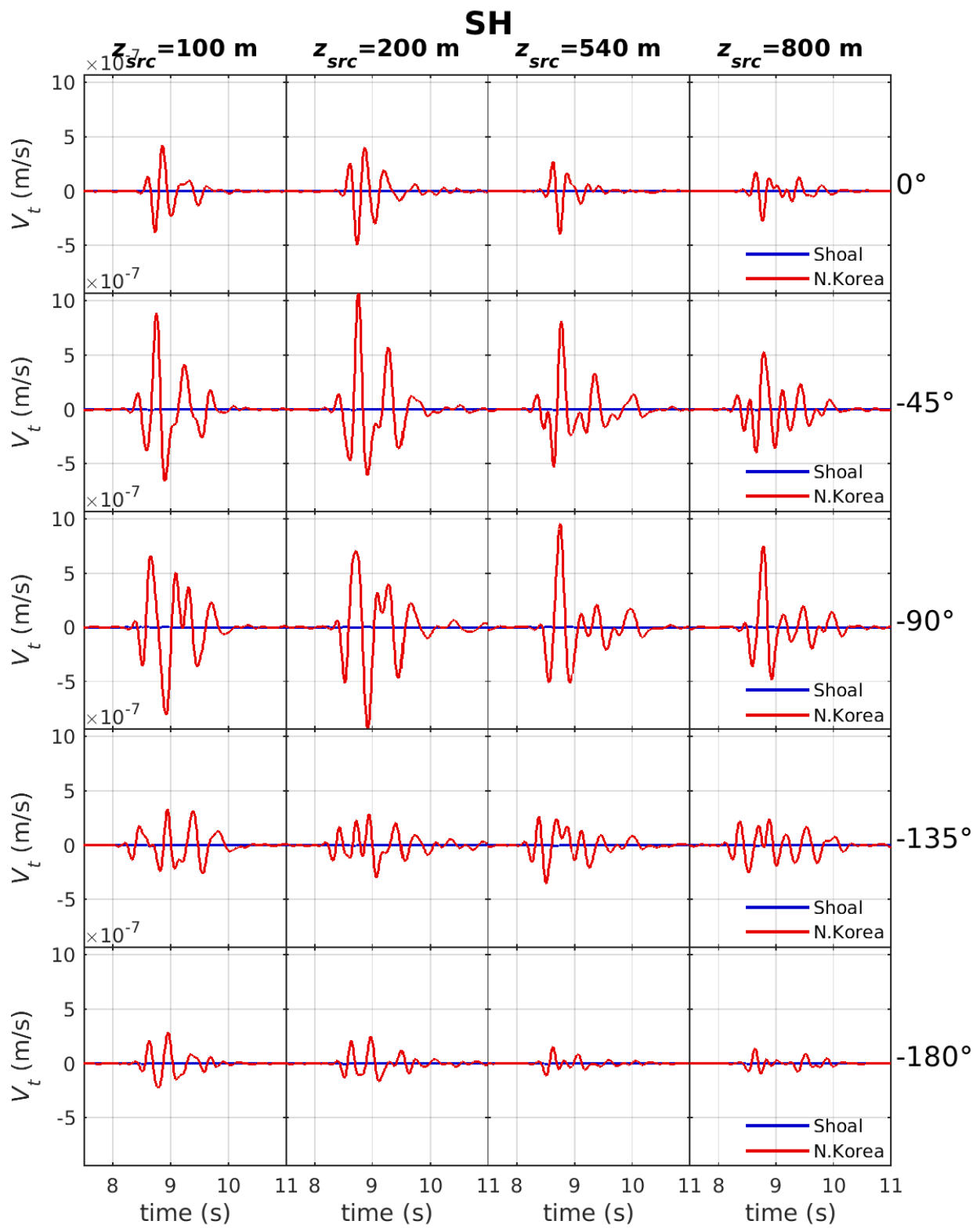


Figure 65. Far-field SH-wave at 1000km for Shoal and North Korea simulations

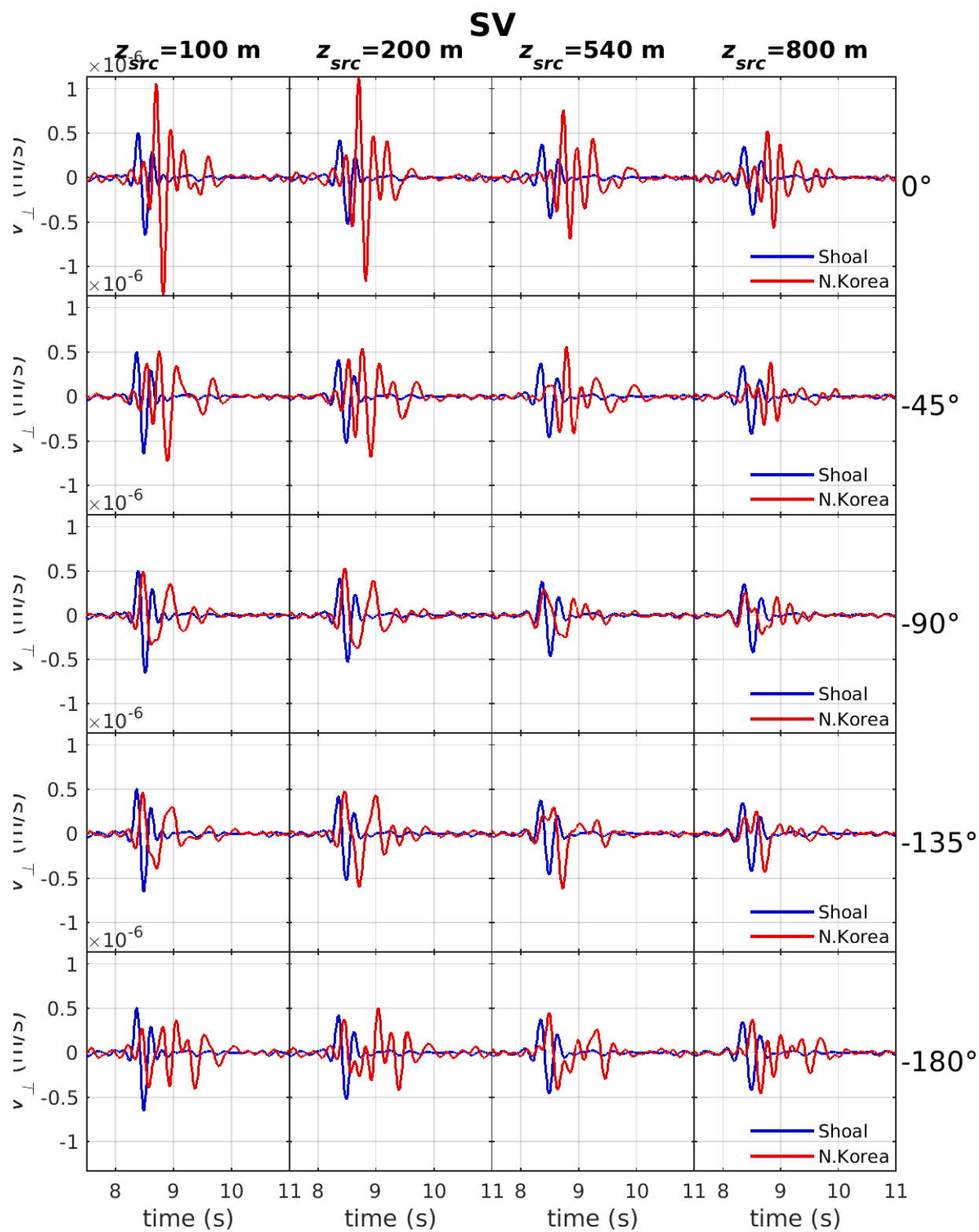


Figure 66. Far-field SV-wave at 1000km for Shoal and North Korea simulations

4.5 Decomposition of the Seismic Source

Seismic waves from explosions are affected by material properties at and near the source, depth and overburden pressure, tectonic stresses and topography. We discussed topography in the previous chapters. Here we look at the effects of depth, material properties and tectonic stress state. To do this, we have performed nonlinear axisymmetric calculations at 13 depths ranging from 150 meters to 1000 meters, in four earth structures with distinctly different material properties, and we have performed each calculation with no tectonic stresses and with tensile and compressive stresses (Figure 67), a total of 156 calculations. Calculations were performed for explosion yields of either 10 kilotons or 12.5 kilotons. Normal containment depth for these explosions is about 300 meters, so the calculations range from approximately $\frac{1}{2}$ normal containment depth to more than 3 times normal containment depth. We also performed one dimensional, spherically symmetric calculations corresponding to each axisymmetric calculation, using the material properties and overburden pressure corresponding to each depth.

The earth structures and material properties used were chosen to illustrate the physical phenomena that contribute to variations in near source deformation and ground motion. These properties include elastic moduli, density, porosity and shear strength. Shear strength increases as a function of pressure (Figure 68). Porous media has a crush curve that describes the change in porosity and elastic moduli as pores are crushed by the pressure from the explosion. Of particular importance is the reduction in strength after failure. This is modeled in two ways: 1) using a damage model that decreases strength as a function of nonlinear shear strain; and 2) using the effective stress model which reduces strength as pores are crushed out. In the effective stress model the strength is determined by the difference between the pressure and the pore pressure. These become equal when the pores are crushed out so the strength of the material is determined by the zero pressure point in Figure 68.

The first two structures are a Degelen Mountain structure and a Climax Stock structure. In both cases the material used in the nonlinear calculations was granite, with a compressional velocity of 5175 m/s, a shear velocity of 3026 m/s and density of 2600 kg/m³. The granite models initially have the same strength, however after failure the Climax Stock granite is modeled as crushed rock with a dynamic coefficient of friction of 0.017, while the Degelen granite has a post-failure coefficient of friction of 0.2, so the Climax Stock granite is weaker after failure. Strength reduction starts when a cell reaches a nonlinear strain of 0.001 and is fully reduced at a nonlinear strain of

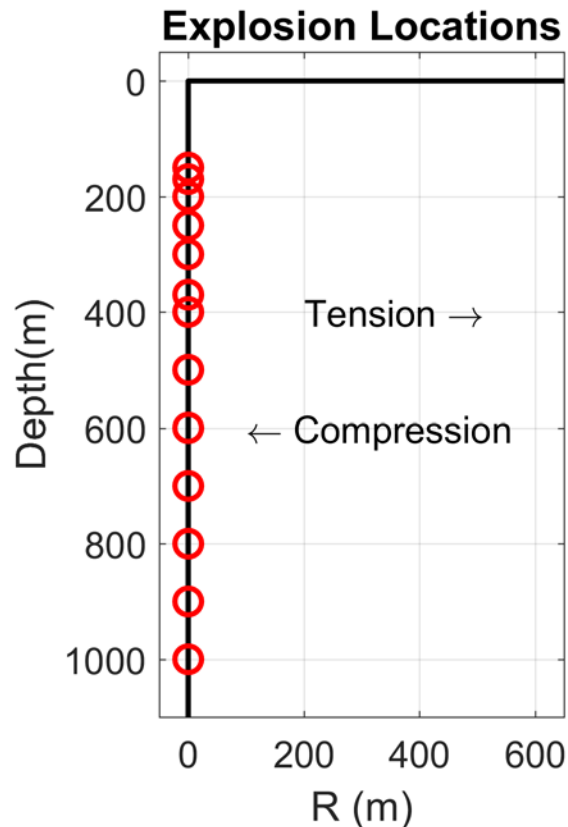


Figure 67. Explosions were calculated at the depths shown from 150m to 1000m (axisymmetry). *Tectonic stresses were simulated by adding a radial tensile or compressive stress.*

0.06. Shear modulus is also reduced after failure from 23.8 GPa to 10 GPa for Climax Stock granite and 5 GPa for Degelen granite. Both of these models were developed based on modeling of near-field data by Stevens et al. (2003). In that study, we had an extensive set of near field data from Degelen Mountain explosions as well as material properties for Degelen Mountain provided by scientists at the Institute for the Dynamics of the Geospheres in Moscow, Russia. The Climax Stock model was more recently used to model the explosion Shoal (Stevens and Thompson, 2015), so these two models are labeled “Degelen” and “Shoal”. These models assume that the pore space is negligible and so do not include pore crushing.

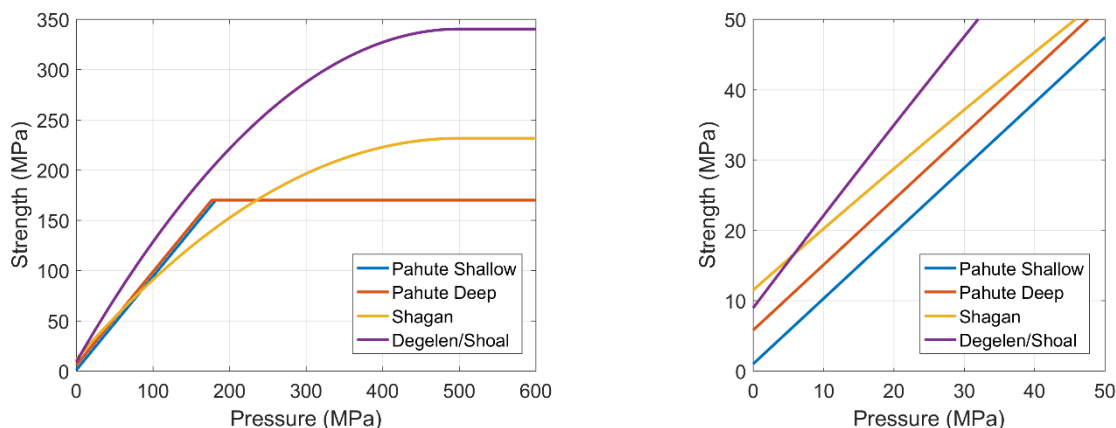


Figure 68. Strength of materials used in this study. Right: expanded view of low pressure part of strength curves. *Strength is determined by stress invariants as defined by Peyton (1983). Strength shown in these figures is approximately equal to shear stress divided by 2.35.*

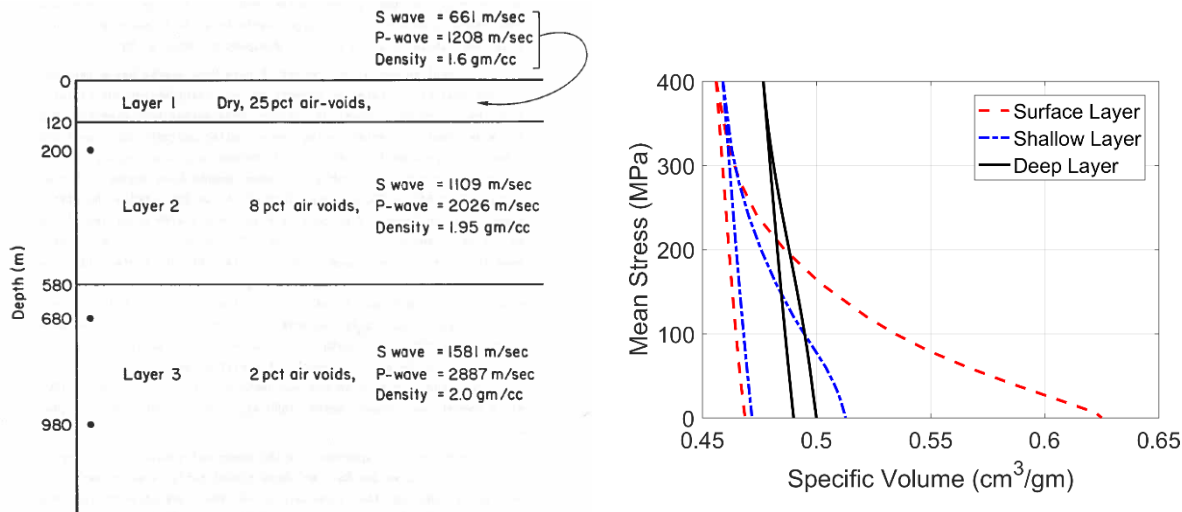


Figure 69. Left: Pahute Mesa structure used in depth of burial study (Day et al, 1986) and used over a wider range of depth in the current study. Right: Load/Unload curves for the three layers. *The other two structures are based on the depth of burial study performed by Day et al. (1986). These are models for a three-layered Pahute Mesa structure and Shagan River granite. Both of these models include pore crushing and used the effective stress model for strength reduction. The Pahute Mesa structure and crush curves for each layer are shown in Figure 69. The Shagan River structure was uniform granite with a compressional velocity of 5018 m/s, shear velocity of 2788 m/s, porous density of 2700 kg/m³, and 1% porosity.*

4.5.1 Earth model with prestress

Calculations were performed for regions in both tensile and compressive prestress. We assume that the water table is close to the surface and calculate the stress state corresponding to equilibrium for sliding on normal and thrust faults, respectively in a medium with a coefficient of friction of 0.6 (Zoback, 2010). Note that this affects only the horizontal stress field; the vertical stress corresponds to the weight of the material above. The frictional equilibrium state is given by:

$$\frac{S_1 - P_f}{S_3 - P_f} = \left(\sqrt{\mu^2 + 1} + \mu \right)^2$$

Where S_1 and S_3 are the horizontal and vertical principal stresses as discussed below, P_f is the pore pressure and μ is the coefficient of friction. For $\mu=0.6$, the expression on the right hand side is 3.12, so the stress difference can be quite large. In a tensile stress state (normal faulting), S_1 is S_v , the vertical stress and S_3 is S_{hmin} , the minimum horizontal stress. In a compressive stress state (thrust faulting), S_1 is S_{Hmax} , the maximum horizontal stress and S_3 is S_v . Figure 70 shows the calculated stress field as a function of depth for the granite models. Since we are doing axisymmetric calculations, the stress is uniform in all horizontal directions ($S_{xx}=S_{yy} \neq S_{zz}$), but the horizontal stress is less than the vertical stress in regions of extension (normal faulting) and greater than the vertical stress in regions of compression (thrust faulting). S_{zz} is equal to S_v , the vertical stress determined by the weight of the material above.

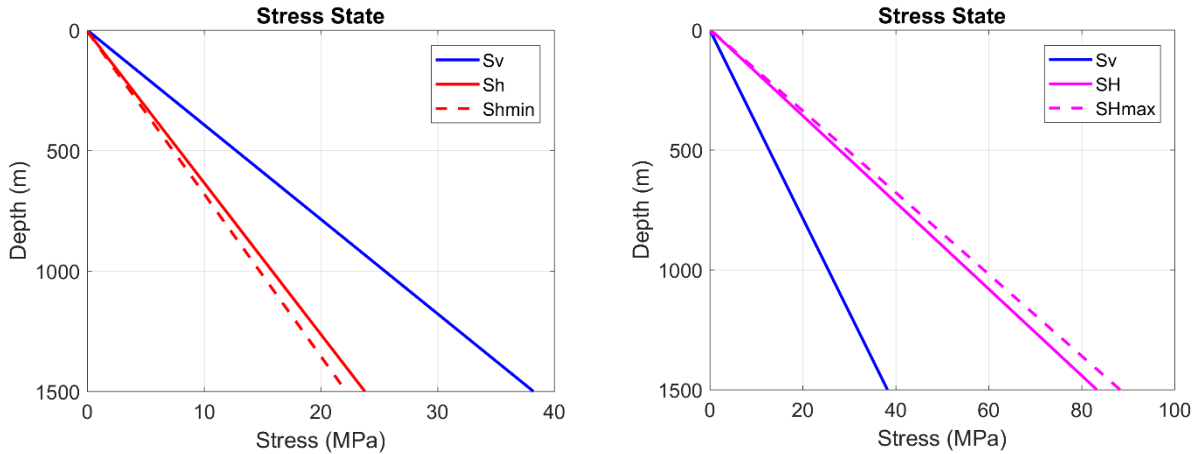


Figure 70. Left: tensile stress state corresponding to a state in balance with normal faulting with a coefficient of friction of 0.6. Right: compressive stress state in balance with thrust faulting with a coefficient of friction of 0.6. *Dashed lines are the limiting stress; solid lines are the stress used in the calculations.*

4.5.2 Near field nonlinear deformation

Shallow explosions generate a nearly conical region of nonlinear deformation around the explosion and up to the surface while deeper explosions generate a more spherical region of nonlinear deformation around the explosion plus some near-surface spall. Figure 71 through Figure 74 show the region of nonlinear deformation for the four structures at depths of 150, 300, 600 and 1000 meters.

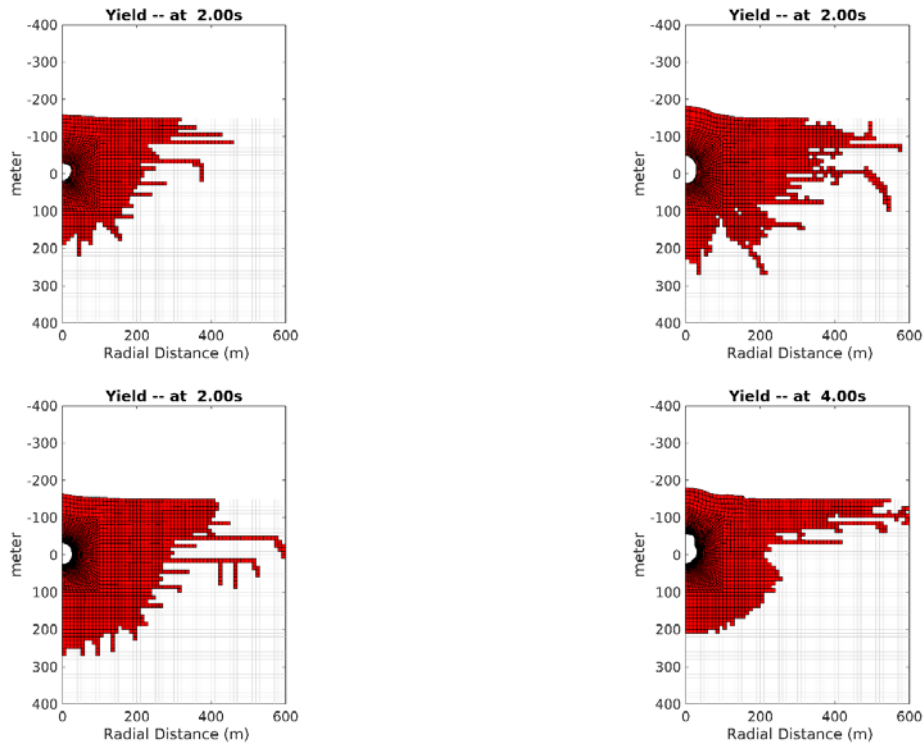


Figure 71. Region of nonlinear deformation for an explosion at 150 meters depth. Top left: Degelen; top right: Shoal; bottom left: Shagan; bottom right: Pahute. *The Degelen explosion was 10 kt; the other three 12.5 kt.*

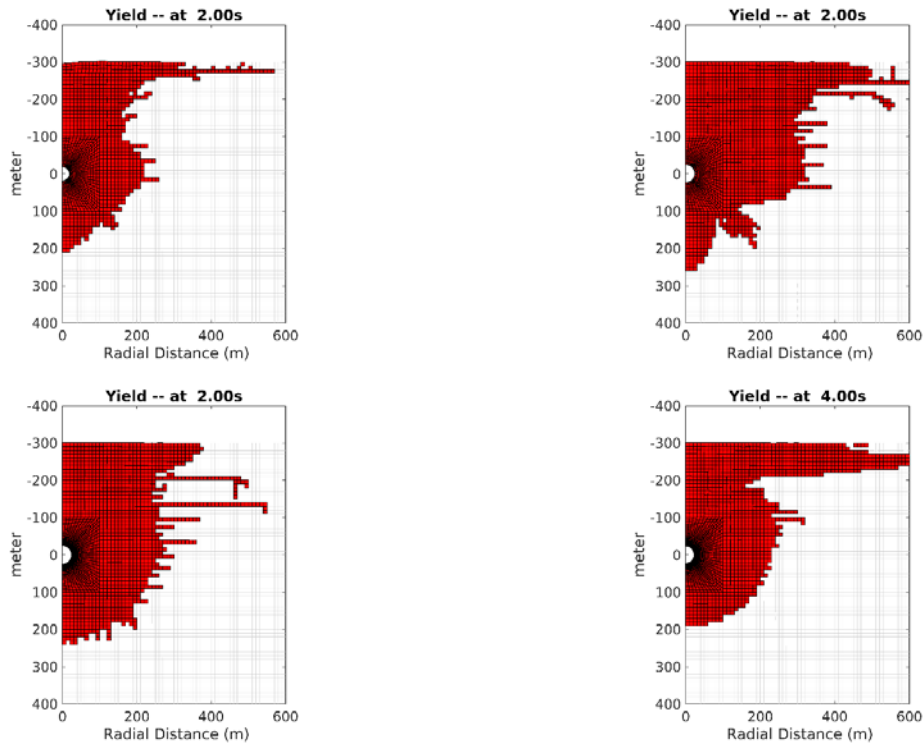


Figure 72. Region of nonlinear deformation for an explosion at 300 meters depth. Top left: Degelen; top right: Shoal; bottom left: Shagan; bottom right: Pahute.

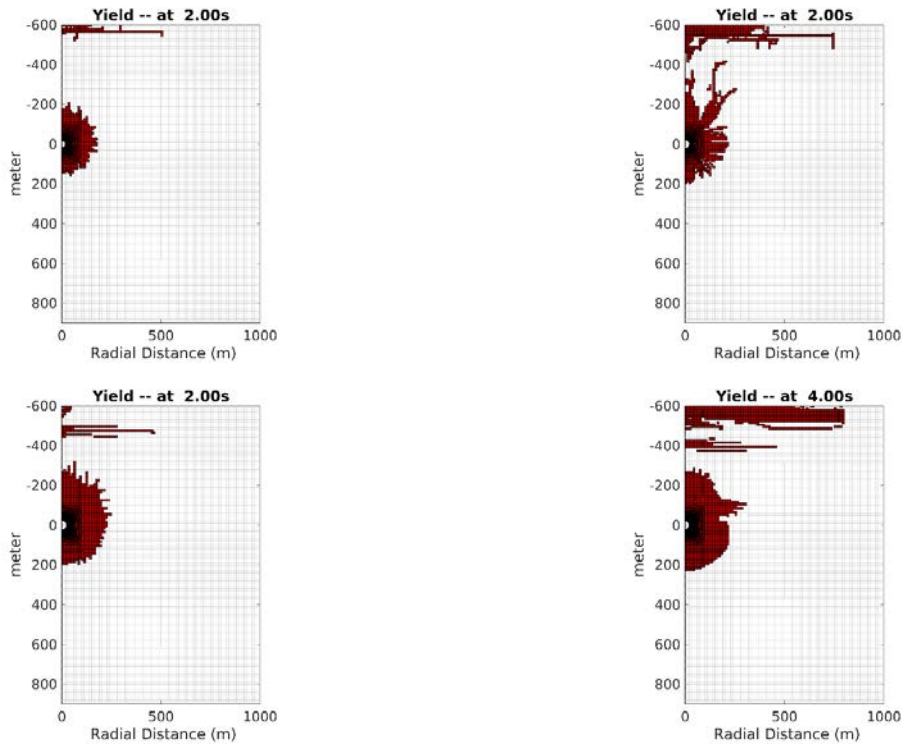


Figure 73. Region of nonlinear deformation for an explosion at 600 meters depth. Top left: Degelen; top right: Shoal; bottom left: Shagan; bottom right: Pahute.

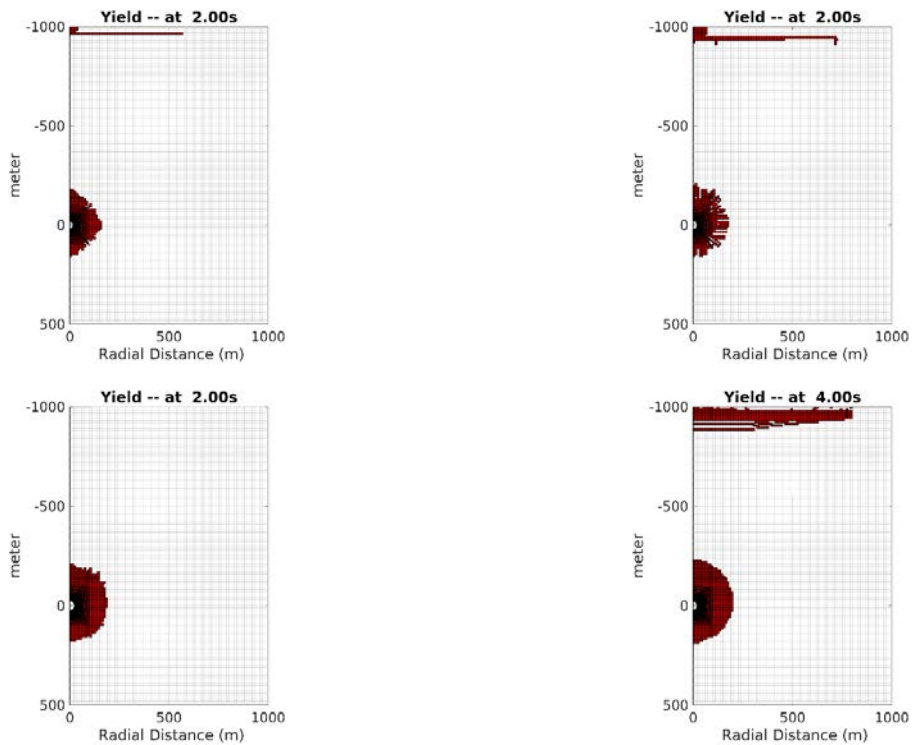


Figure 74. Region of nonlinear deformation for an explosion at 1000 meters depth. Top left: Degelen; top right: Shoal; bottom left: Shagan; bottom right: Pahute.

4.5.3 Near field nonlinear deformation in a tectonic stress field

Figure 75 to Figure 77 show the near field nonlinear deformation for explosions at depths of 150m, 300m and 600m in compressive and tensile stress fields. In all cases there is more deformation in tensile stress fields and less in compressive stress fields. There are two effects operating here: 1) both compressive and tensile stress fields increases the shear stress; and 2) the compressive stress field increases the pressure thereby increasing strength while the tensile stress field decreases the pressure and so decreases strength.

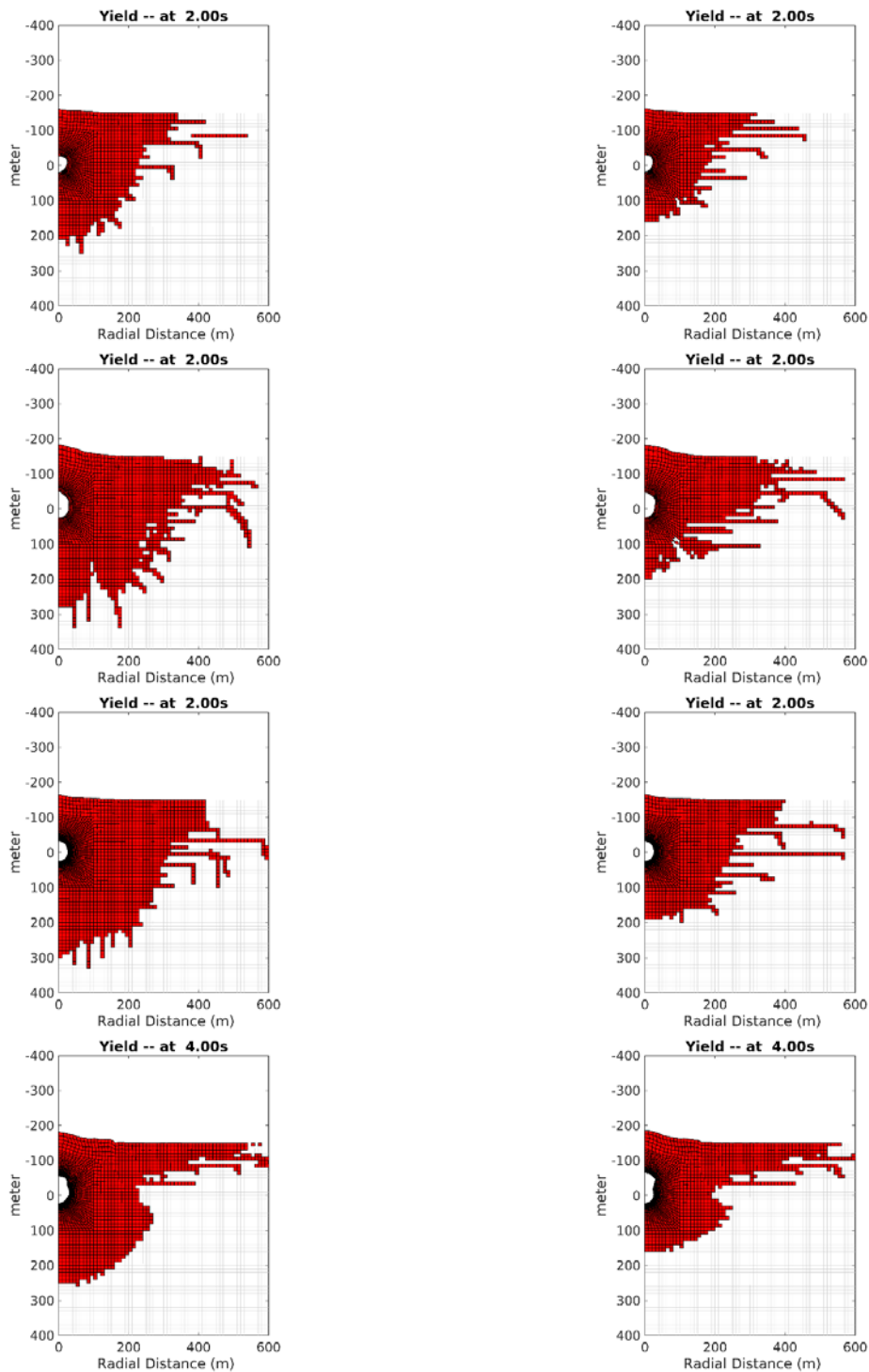


Figure 75. Region of nonlinear deformation for an explosion in a prestress field at 150 meters depth. Left figures are tensile stress fields, right figures are compressive stress fields. Top row: Degelen; second row: Shoal; third row: Shagan; bottom row: Pahute.

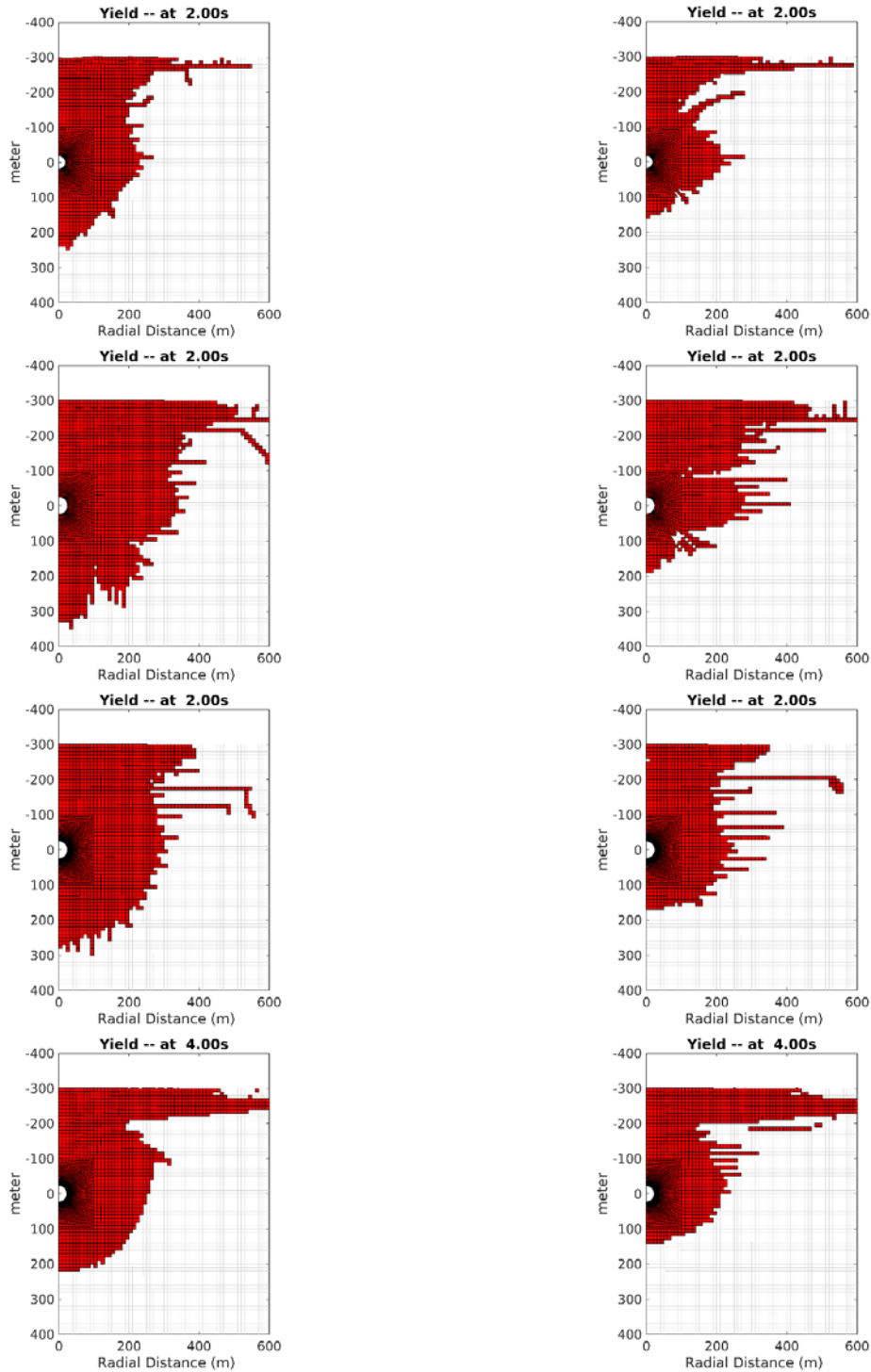


Figure 76. Region of nonlinear deformation for an explosion in a prestress field at 300 meters depth. Left figures are tensile stress fields, right figures are compressive stress fields. Top row: Degelen; second row: Shoal; third row: Shagan; bottom row: Pahute.

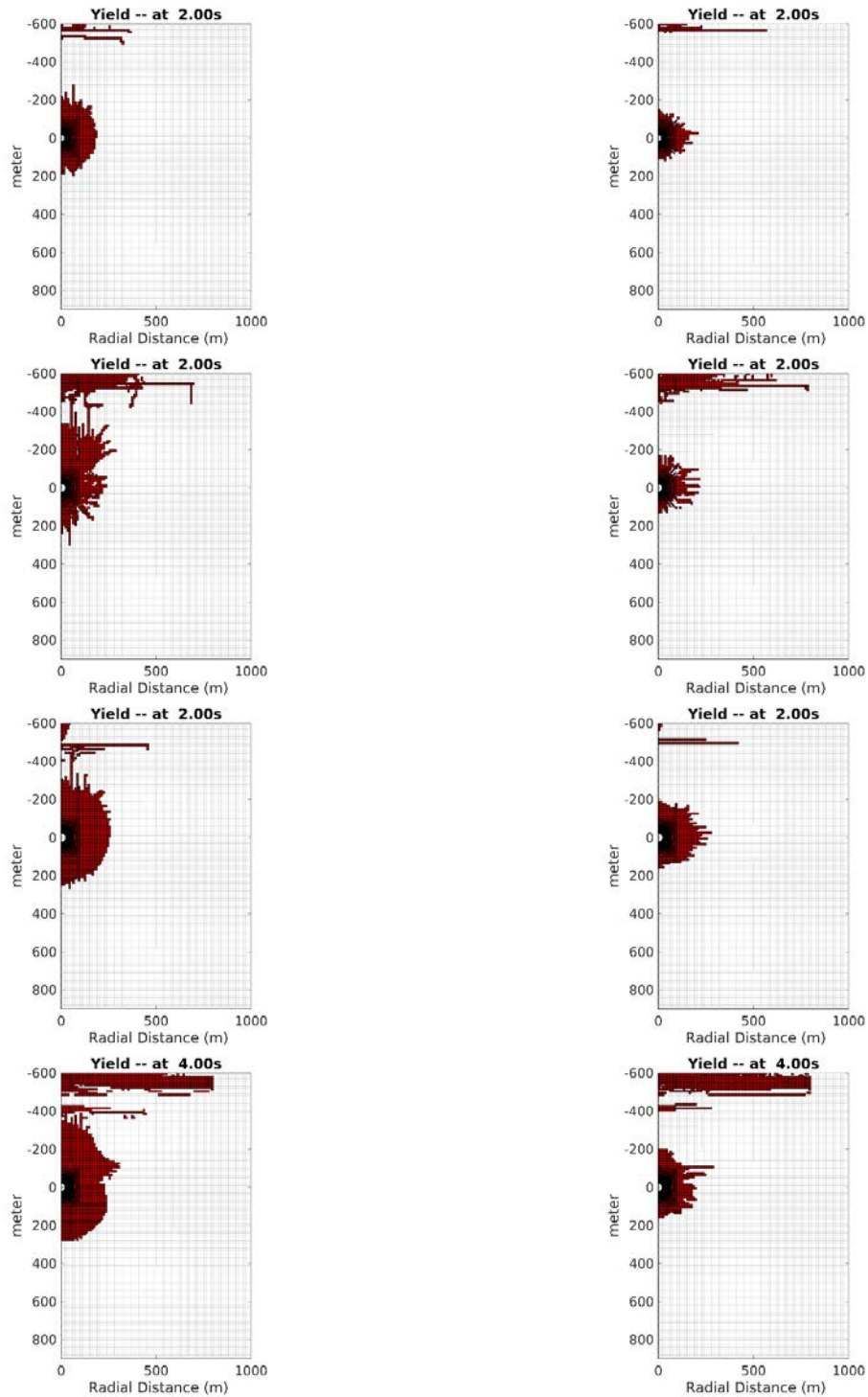


Figure 77. Region of nonlinear deformation for an explosion in a prestress field at 600 meters depth. Left figures are tensile stress fields, right figures are compressive stress fields. Top row: Degelen; second row: Shoal; third row: Shagan; bottom row: Pahute.

4.5.4 Propagation using the representation theorem

The representation theorem was used to calculate surface waves at 2000 km, regional phases at 250 km, and far-field body waves from each calculation. An equivalent point source calculation was made for each using the reduced velocity potential (RVP) convolved with a plane-layered Green's function for each phase. These were compared to determine the effect of the nonlinear interaction with the free surface compared to an elastic calculation. The earth structures used for calculations of regional phases and surface waves are shown in Figure 78. These are regional structures for each site with the material properties of the nonlinear calculations in the upper part of the structure. For the Pahute structure, the two slow, shallow layers were removed and the properties of the third layer used all the way to the surface. The nonlinear calculations also merged into this structure outside of the source region. The Degelen and Shagan structures used the earth model for that region derived from surface waves by Stevens et al (2008). They differ only in the material properties of the top layer, which is lower velocity for Shagan than for Degelen. The Pahute and Shoal structures are derived from an earth model for the Nevada Test Site.

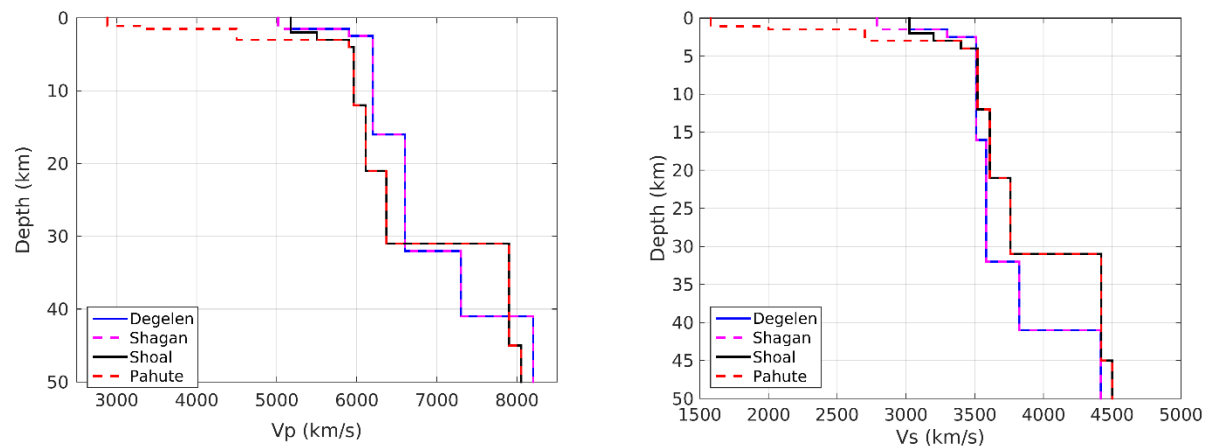


Figure 78. Vp and Vs vs. depth for the four structures used in the calculations.

4.5.5 Surface wave results

Surface waves were calculated as discussed above for each axisymmetric calculation in each of the four structures, and also for the equivalent point source calculation at each depth. We first summarize the results in Figure 79 and Figure 80 and then show some waveform examples. We find that surface waves from one-dimensional spherically symmetric calculations and two-dimensional axisymmetric calculations agree fairly well and show a slow decrease with depth for depths greater than about 300 meters, however at shallower depths the free surface interaction causes a sharp decrease in the surface wave amplitude. Surface waves are reduced by compressive tectonic strain release and increased by tensile tectonic strain release, with compressive being the stronger effect. The shallower calculations in the Climax stock (Shoal) granite calculation, with compressive tectonic strain release are polarity reversed. Surface waves from the Pahute calculation are more complicated because of the high porosity unsaturated media that reduces amplitudes for depths less than 580 meters.

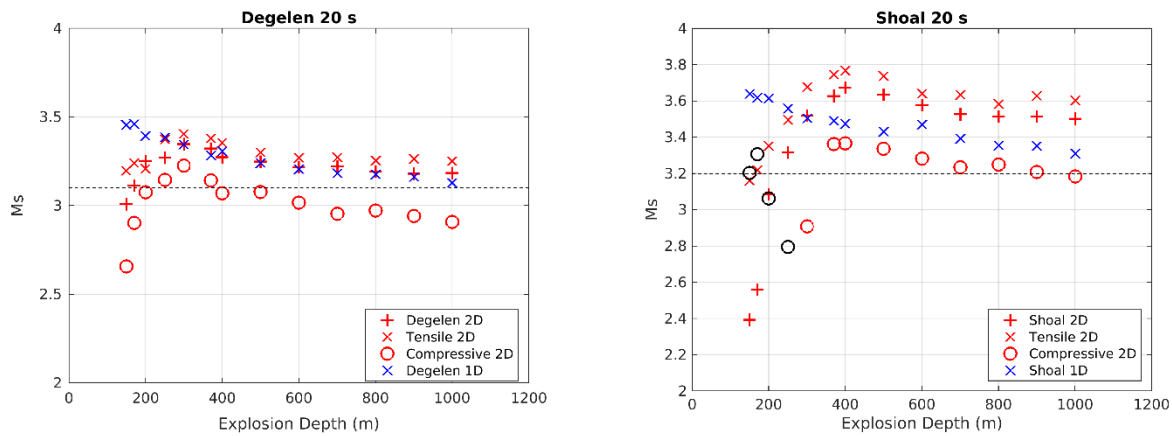


Figure 79. 20 second surface wave magnitudes from all axisymmetric and spherically symmetric calculations. Left: Degelen granite; Right: Climax stock granite. *Black circles indicate surface waves with polarity reversals.*

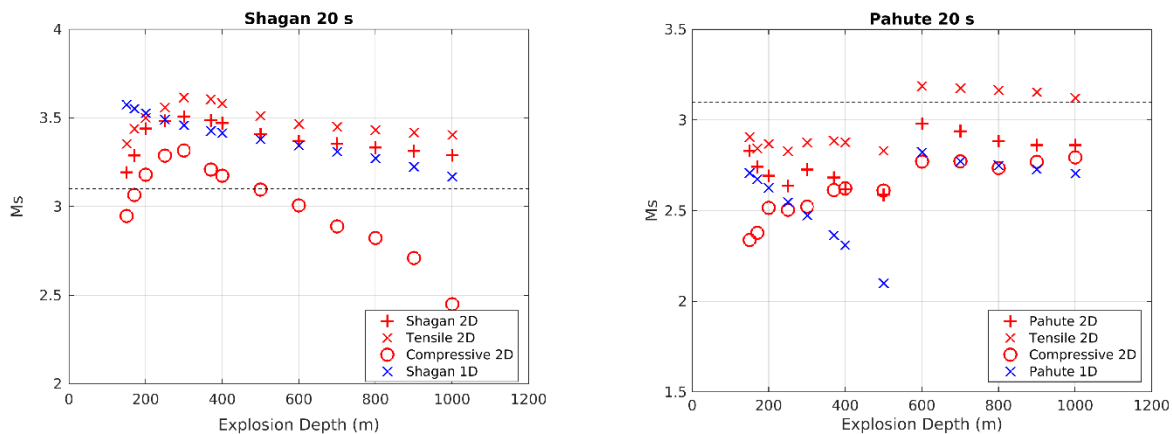


Figure 80. 20 second surface wave magnitudes from all axisymmetric and spherically symmetric calculations. Left: Shagan River granite; Right: Pahute Mesa Rhyolite.

Figure 81 and Figure 82 show the surface waves for the point source calculation and the axisymmetric calculation at explosion depths of 150 and 300 meters in the four structures. All are reduced in amplitude substantially at 150 meters, and the Pahute calculation while not actually reversed, is clearly phase shifted. At 300 meters the point source and axisymmetric calculations are much more similar, particularly for the Degelen and Shagan models. Amplitudes are slightly reduced by the free surface interaction for the Shoal and Pahute models.

A reduction in surface wave amplitude due to near-surface damage was proposed by Patton and Taylor (2008) and Patton (2016). These calculations support that conclusion for shallow explosion sources, with the reduction starting at about normal containment depth. However tectonic strain release also has a strong effect that can both increase and decrease surface wave amplitudes for tensile and compressive stresses, respectively. Increasing depth also decreases surface wave amplitudes due to increasing overburden pressure, so the combination of the near-surface decrease and depth decrease causes a peak surface wave amplitude at a depth near normal containment depth.

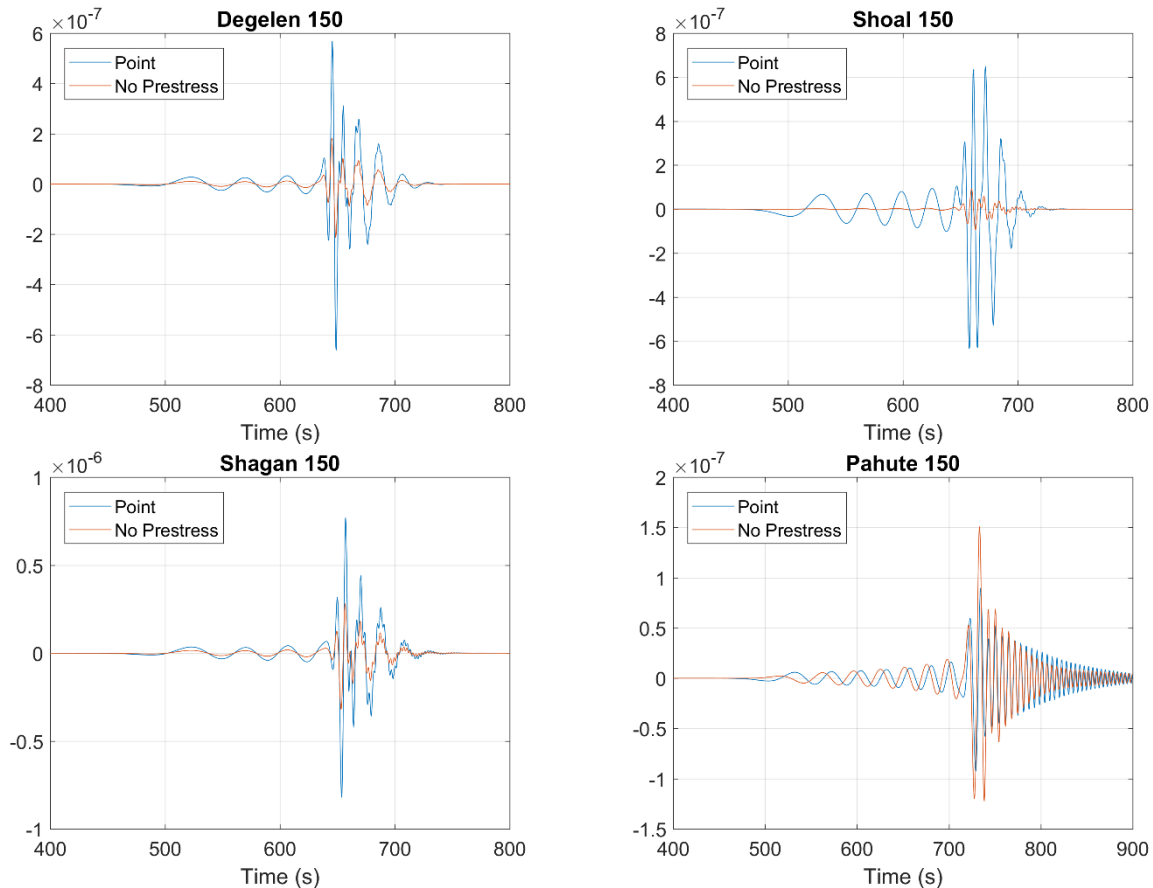


Figure 81. Surface waves for an explosion depth of 150 meters in four structures. *Figures show point source seismograms in blue and axisymmetric calculation without prestress in blue.* Top left: Degelen, top right: Shoal, lower left: Shagan, lower right: Pahute.

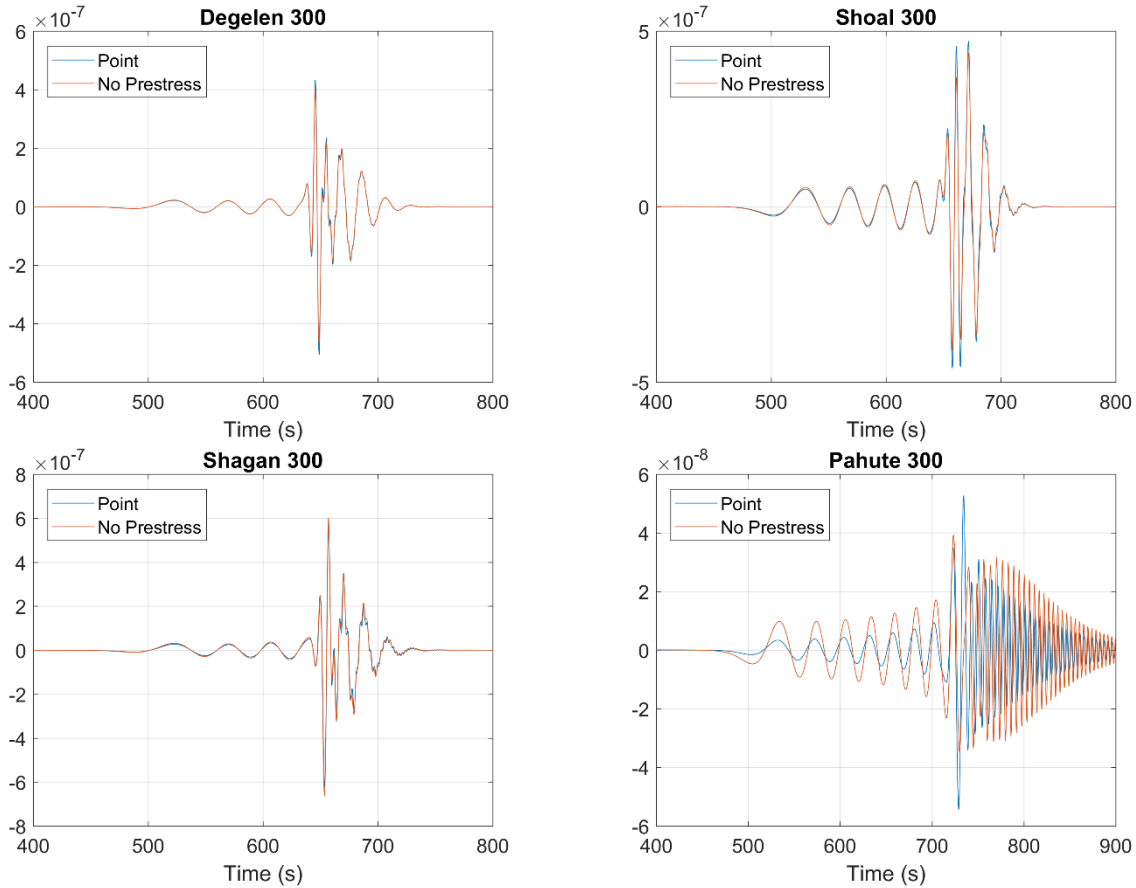


Figure 82. Surface waves for an explosion depth of 300 meters in four structures. Figures show point source seismograms in blue and axisymmetric calculation without prestress in blue. Top left: Degelen, top right: Shoal, lower left: Shagan, lower right: Pahute.

Surface waves are generated primarily by the static horizontal displacements caused by the explosion. Figure 83 - Figure 85 show the final horizontal displacement at depths of 200, 370 and 800 meters, respectively, in the Degelen and Shoal structures and in tensile, no and compressive prestress. In all cases tensile stress increases the horizontal displacement and compressive stress decreases it. In the 200 meter Shoal case with compressive stress, the horizontal displacement is negative, leading to the Rayleigh wave reversals shown in Figure 79.

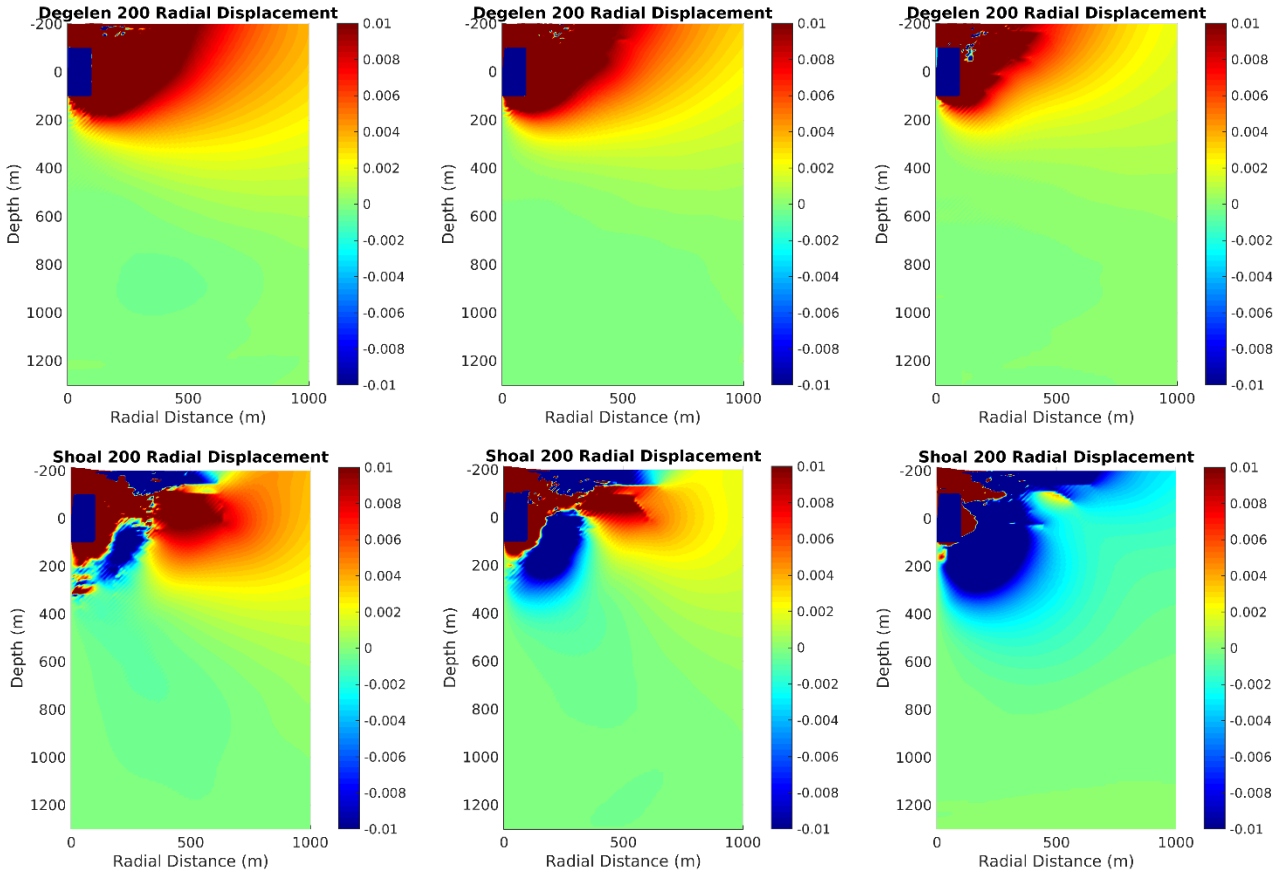


Figure 83. Final horizontal displacement at 200m depth. Left: tensile prestress. Center: no prestress. Right: compressive prestress. Top: Degelen; bottom: Shoal. The horizontal displacement with Shoal in compression is almost entirely negative, leading to the Rayleigh wave reversals shown in Figure 79.

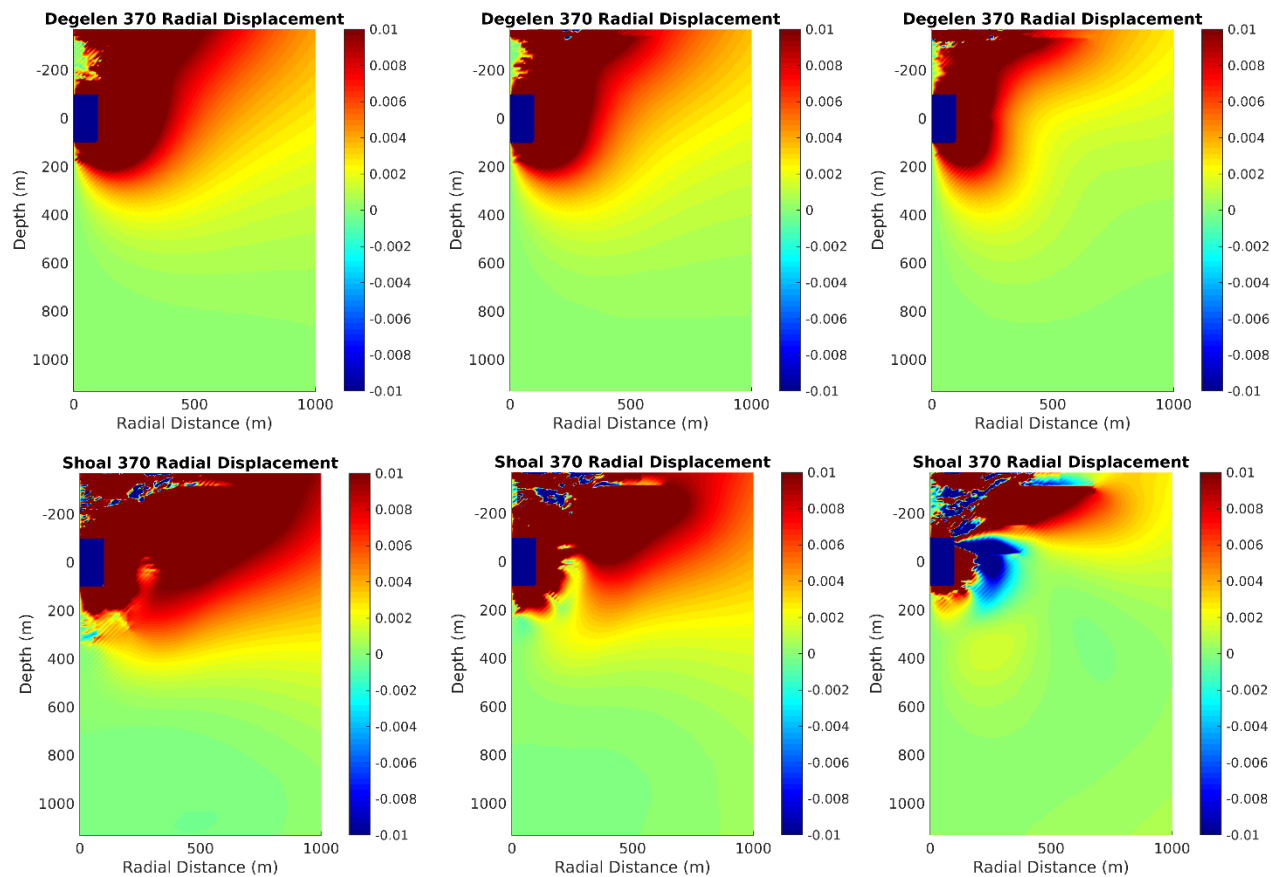


Figure 84. Final horizontal displacement at 370m depth. Left: tensile prestress. Center: no prestress. Right: compressive prestress. Top: Degelen; bottom: Shoal.

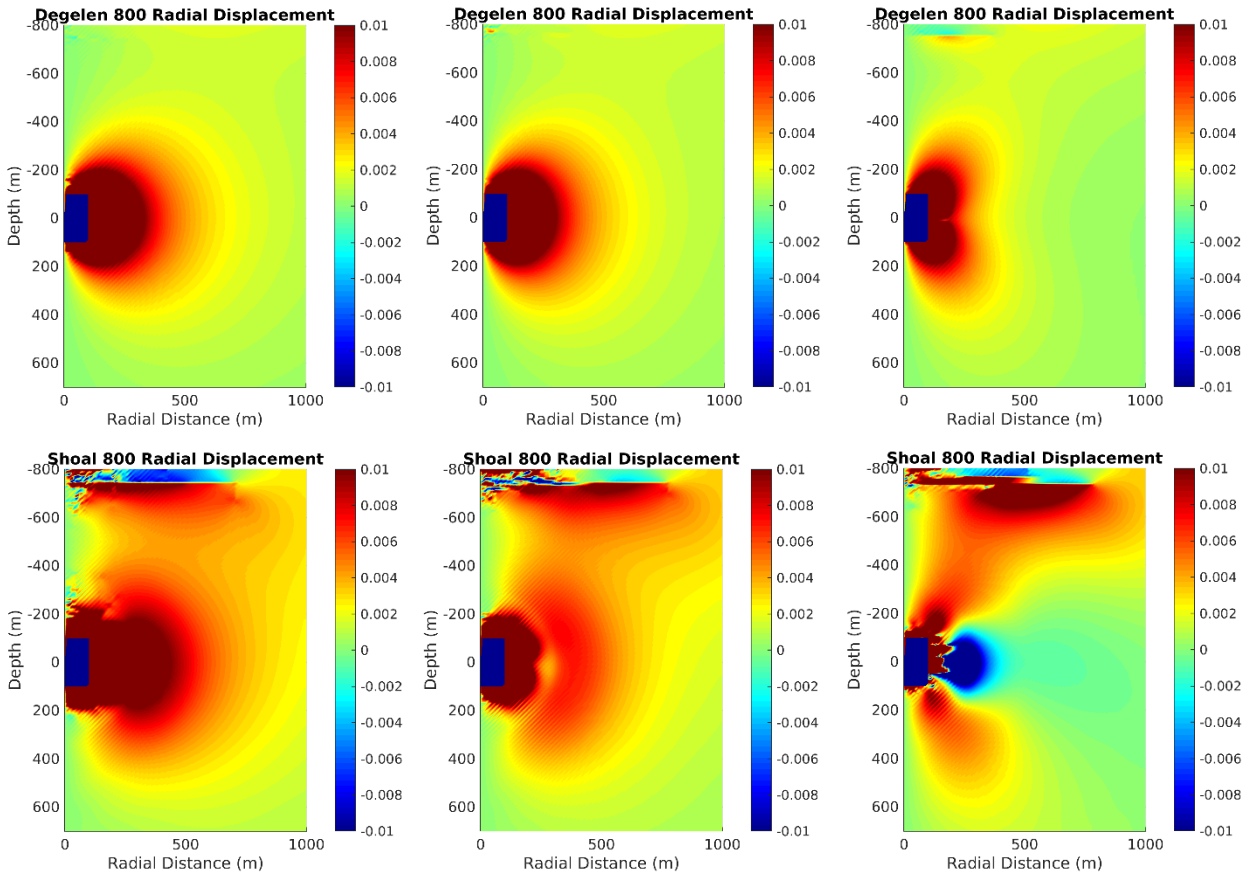


Figure 85. Final horizontal displacement at 800m depth. Left: tensile prestress. Center: no prestress. Right: compressive prestress. Top: Degelen; bottom: Shoal.

To find out why the near surface amplitude reduction occurs, we ran an additional set of calculations in the Degelen model, but with the strength increased enough that no nonlinear deformation occurred (referred to as the “Hard” calculation), so the problem is purely elastic. We then compared the results of that calculation with the Degelen and Shoal calculations.

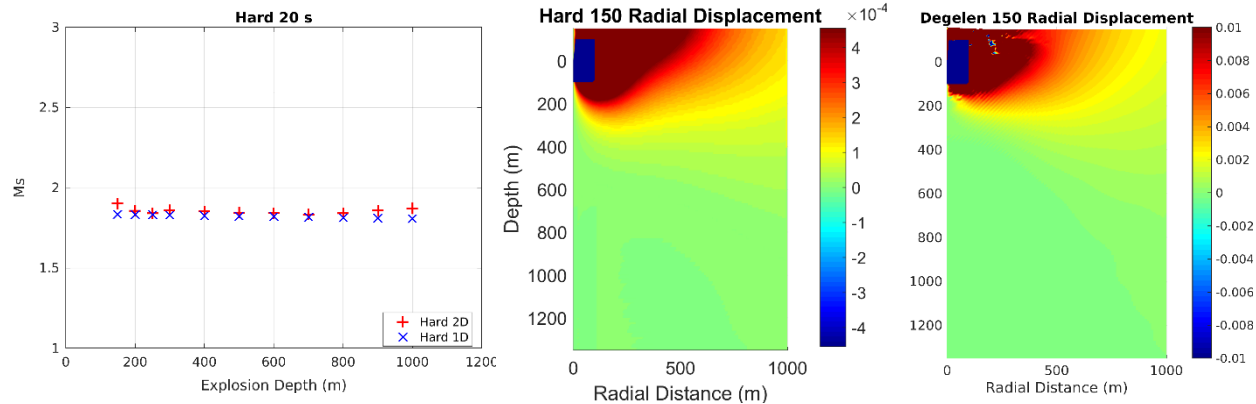


Figure 86. Left: Ms from 1D and 2D “Hard” calculation. Middle: Hard model radial displacement. Right: Degelen Model radial displacement. Both for 150 meters depth.

Figure 86 shows the calculated surface wave amplitudes for the hard model and the radial displacement for the Hard and Degelen models, with the scale on the hard model increased by a factor of 22. Now as expected the surface waves show no depth dependence for either the 1D or

2D models. The patterns of radial displacement are very similar, but there is a reduction in horizontal displacement that increases toward the surface in the Degelen model. We can see this more clearly by examining the difference between the two final displacement fields, which are shown in Figure 87. Above the source the displacement difference is upward and outward where the material is pushed up and away from the explosion. However a short distance out the displacement difference changes to inward and downward, almost as if there were a thrust fault extending from the explosion to the surface. This is similar to the mechanism proposed by Masse (1981), who suggested that induced thrust faulting above the explosion was responsible for Rayleigh Wave reversals and other effects attributed to tectonic strain release.

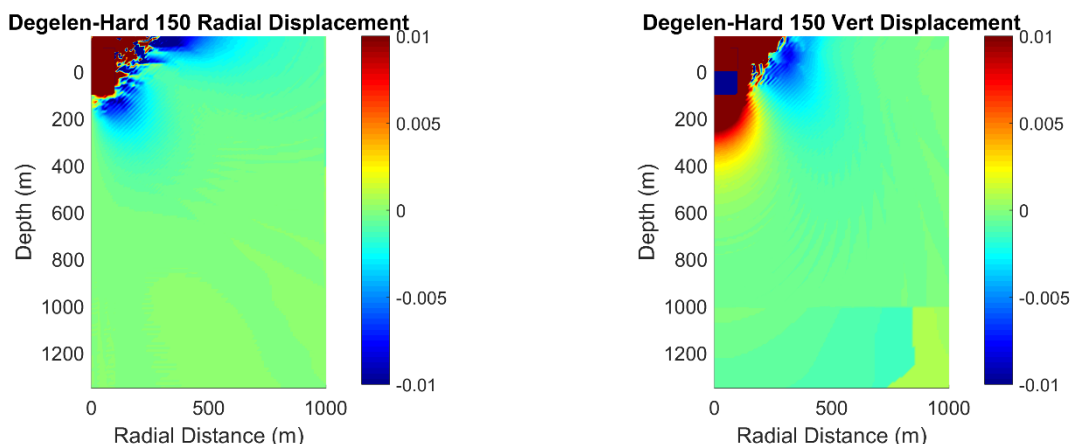


Figure 87. Radial (left) and Vertical (right) displacement field difference between the Degelen and (scaled) Hard models for an explosion at 150 meters depth.

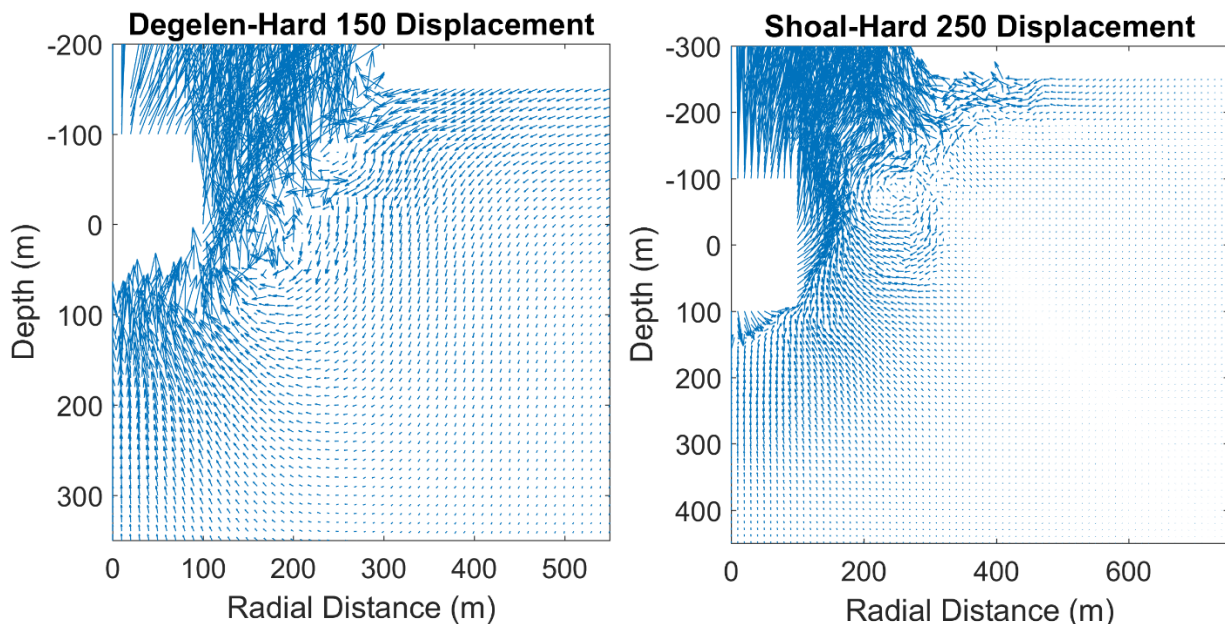


Figure 88. Vectors of displacement difference. Left: Degelen at 150m depth. Right: Shoal at 250m depth.

The shallowest explosions appear to be quite consistent with the Masse model, but deeper explosions have more complex displacement fields. Figure 88 shows vectors of displacement difference between the Degelen and Hard explosions at 150 meters depth and between the Shoal and Hard explosions (scaled by 27.5). At 250 meters there is a “whirl” of displacement to the right of the cavity and inward motion along the surface.

4.5.6 Full Wave Regional Waveforms

We calculated full waveform seismograms for all of the calculations at a distance of 250 km using the earth models described earlier. Example seismograms from the source at 300 meters depth (without tectonic release) are shown in Figure 89. Each figure shows a waveform from the nonlinear calculations propagated using the representation theorem, and also a waveform from a point source plane-layered medium convolved with the RVP from the corresponding spherically symmetric calculation.

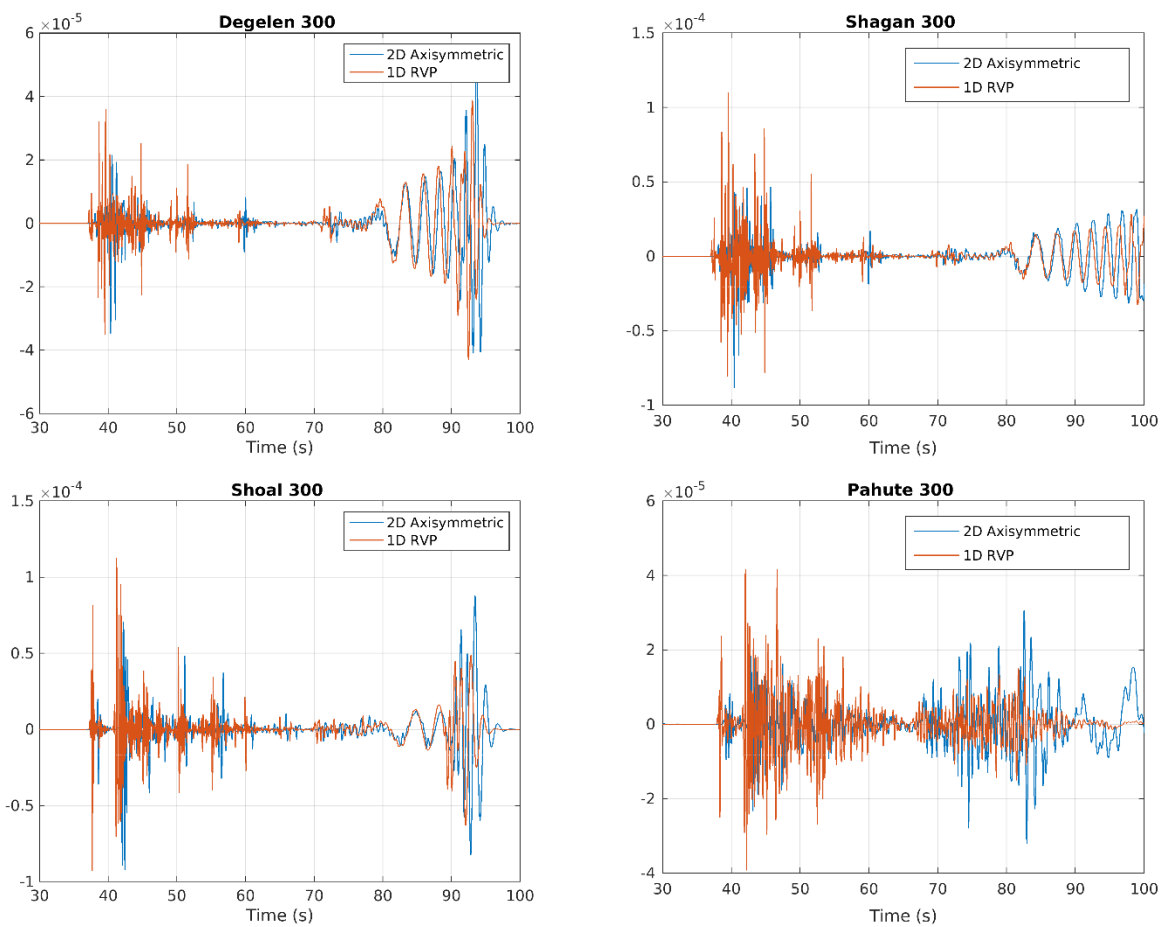


Figure 89. Example full waveform seismograms for the four earth models. *Seismograms labeled 2D Axisymmetric are generated from the nonlinear axisymmetric calculations using the representation theorem. Seismograms labeled 1D RVP are point source plane-layered full waveform seismograms convolved with an RVP for the source.*

We are interested in how the nonlinear interaction with the free surface and tectonic release affect regional phase amplitudes. To do this, we filtered each seismogram with a 3 pole two-pass Butterworth filter with a passband of 0.6 to 3.0 Hz, then found the peak amplitude within arrival time windows of 35-55 seconds (4.5-7.1 km/s) for P-waves, 55-65 seconds (3.8-4.5 km/s) for S-

waves, and 65-78 seconds (3.2-3.8 km/s) for Lg. Measurements for all calculations are shown in the following figures.

Figure 90 shows regional P-wave amplitudes for all calculations. There is a slow decrease in amplitude with depth caused by the increasing overburden pressure. The 2D and 1D calculations for the three granite structures are very similar and tectonic stresses appear to have little effect on the P-waves. The Pahute structure also shows little effect on P-waves from tectonic stresses. The 1D Pahute calculations have higher amplitudes than the 2D calculations, however the 1D calculations were embedded in the structure without the two surface layers, so the 1D and 2D Pahute calculations may not be directly comparable.

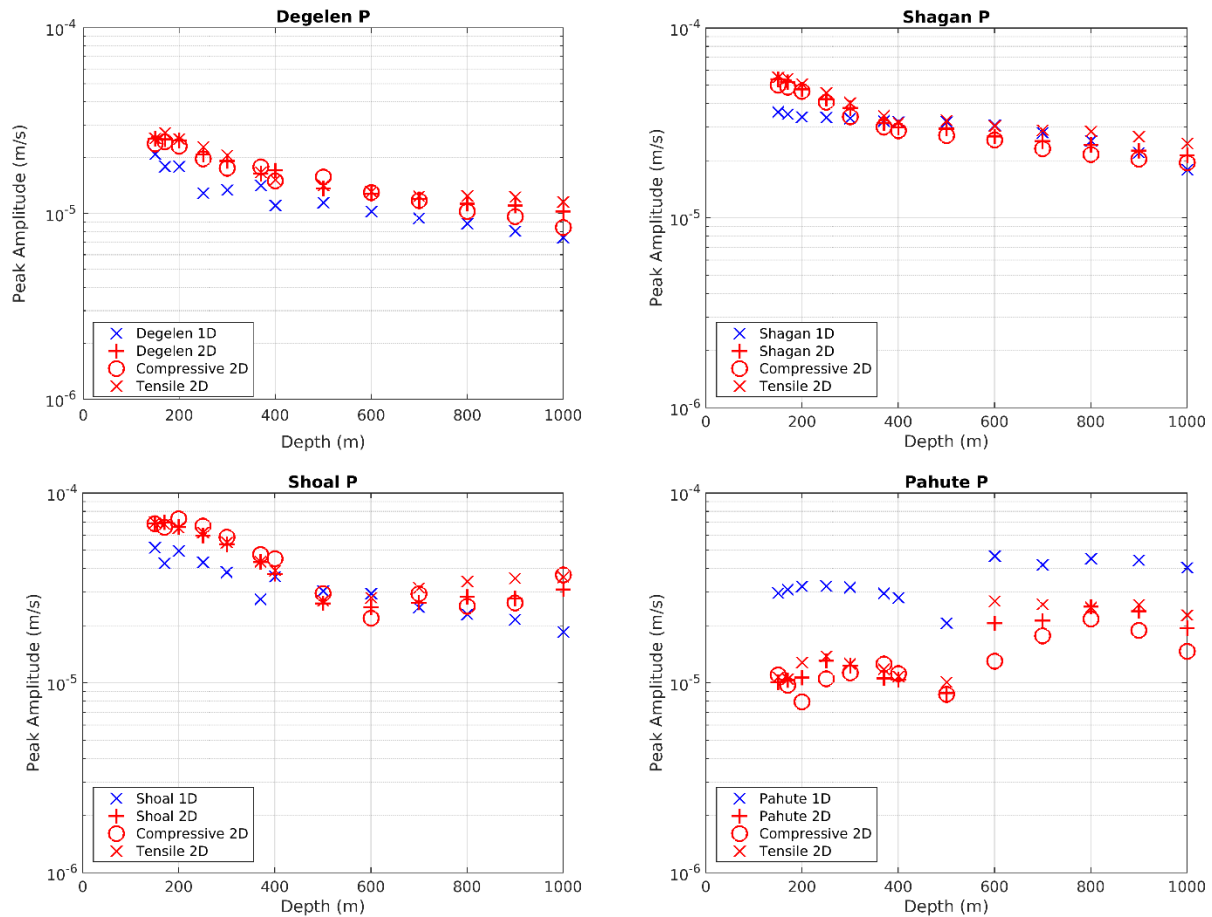


Figure 90. P-wave amplitudes for each structure. Blue points are the 1D calculation, Red points are the 2D axisymmetric calculations with and without tectonic release.

Figure 91 shows regional S-wave amplitudes for all calculations. Now the effect of the nonlinear interaction with the free surface is much more apparent. In all of the granite structures at shallower depths the surface interaction generates substantially more S-waves compared to the point source, which only generates S-waves through pS reflection.

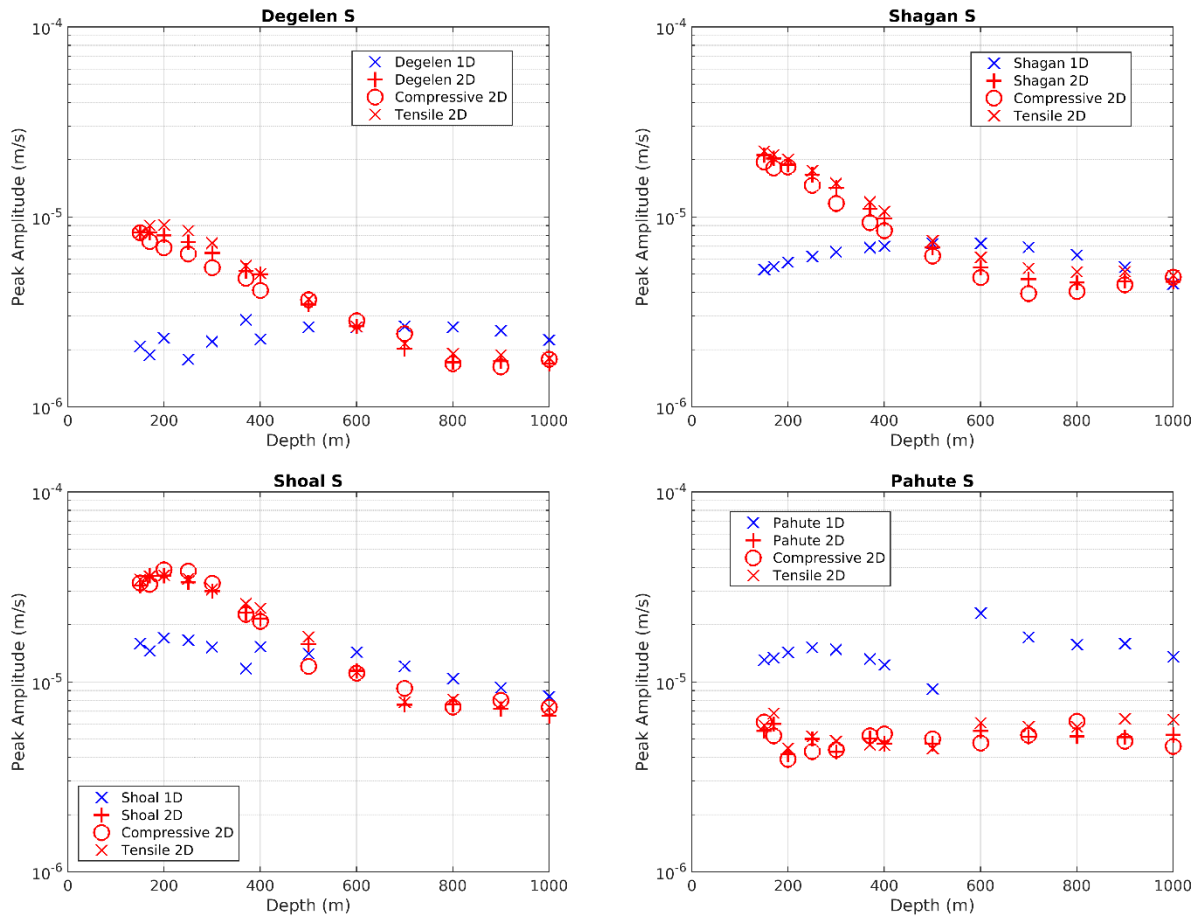


Figure 91. S-wave amplitudes for each structure. *Blue points are the 1D calculation, Red points are the 2D axisymmetric calculations with and without tectonic release.*

Figure 92 shows Lg amplitudes for all calculations (with the caveat that any enhancement of Lg due to scattering is not included). The free surface interaction has surprisingly little effect on Lg, with the Degelen and Shoal structures showing a small near-surface decrease similar to the fundamental mode surface waves. For deeper sources, tectonic release does affect the Lg amplitudes, and does so opposite the effect on fundamental mode surface waves with compression increasing Lg and tension decreasing it.

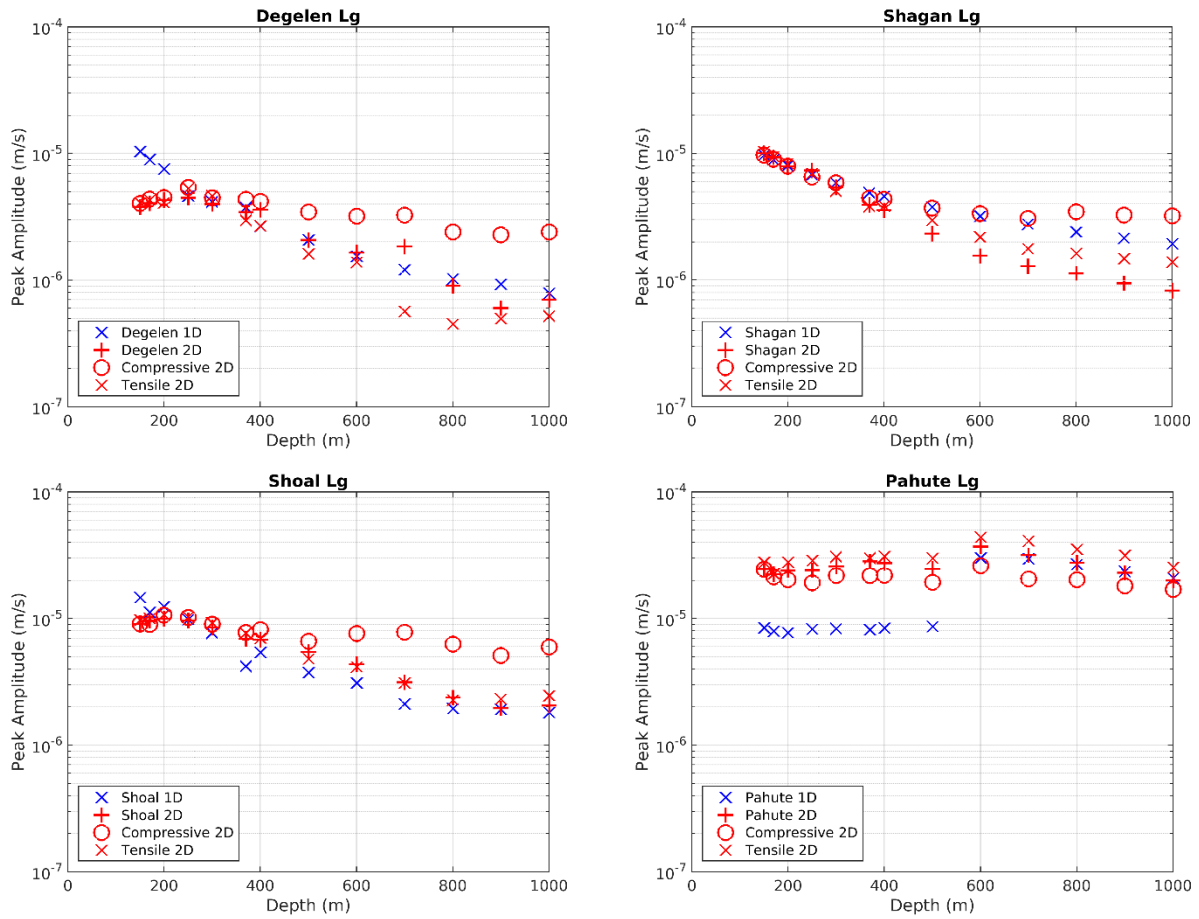


Figure 92. Lg amplitudes for each structure. *Blue points are the 1D calculation, Red points are the 2D axisymmetric calculations with and without tectonic release.*

4.5.7 Far-field Body Waves

Far-field P and SV waves were calculated for all of the nonlinear calculations using the representation theorem. Because we are interested in the effects of the nonlinear interaction with the free surface rather than crustal reflections, we use only the part of each structure above 1530 meters and calculate the P and SV waves as they leave the base of the structure. P waves are calculated at a takeoff angle of 10° , SV waves at 20° . Example waveforms for a depth of 250 meters are shown in Figure 93. The main physical effect operating here is the degradation of the pP and pS phases by the nonlinear interaction with the free surface. The initial P-wave amplitude is very similar between the 1D and 2D calculations because the initial downgoing P-wave is unaffected by the free surface, however subsequent reflected phases are decreased in amplitude, distorted and spread out in time. The Pahute SV waveforms are complex because of reflections within the low velocity surface layers. The waveforms shown in Figure 93 are low-pass filtered at 10 Hz, and in the frequency band the pP tends to increase the P-wave amplitude. That combined with the larger RVP for shallow events causes the 1D amplitudes to increase at shallow depths, while the P-wave amplitudes from the 2D calculations remain almost constant with depth.

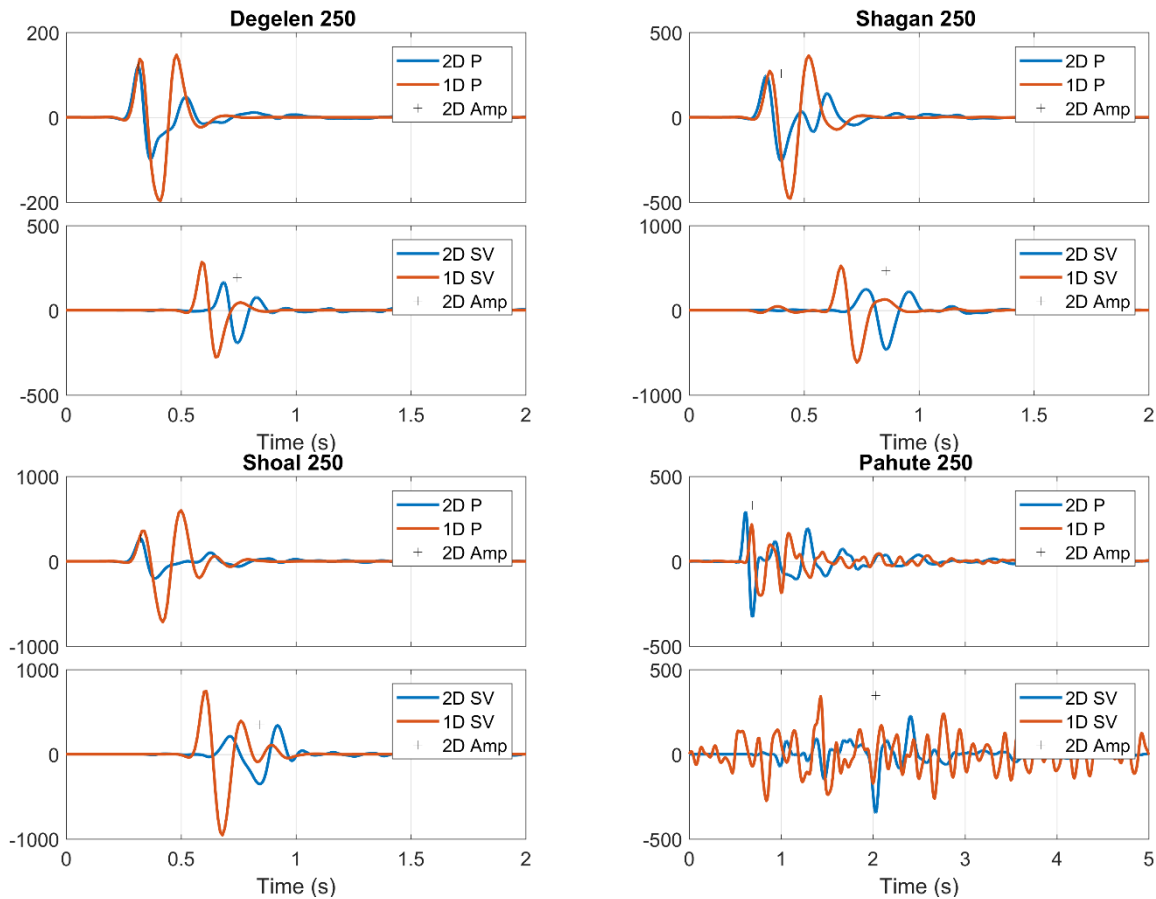


Figure 93. Far-field P and SV waves from 1D and 2D calculations at a depth of 250 meters in the four earth structures. *No tectonic stresses. Mark shows measured amplitude for the 2D waveform. All waveforms are low-pass filtered at 10 Hz.*

Figure 94 and Figure 95 show the amplitude measurements for all P and SV waveforms for all depths, with and without tectonic stresses in the four structures.

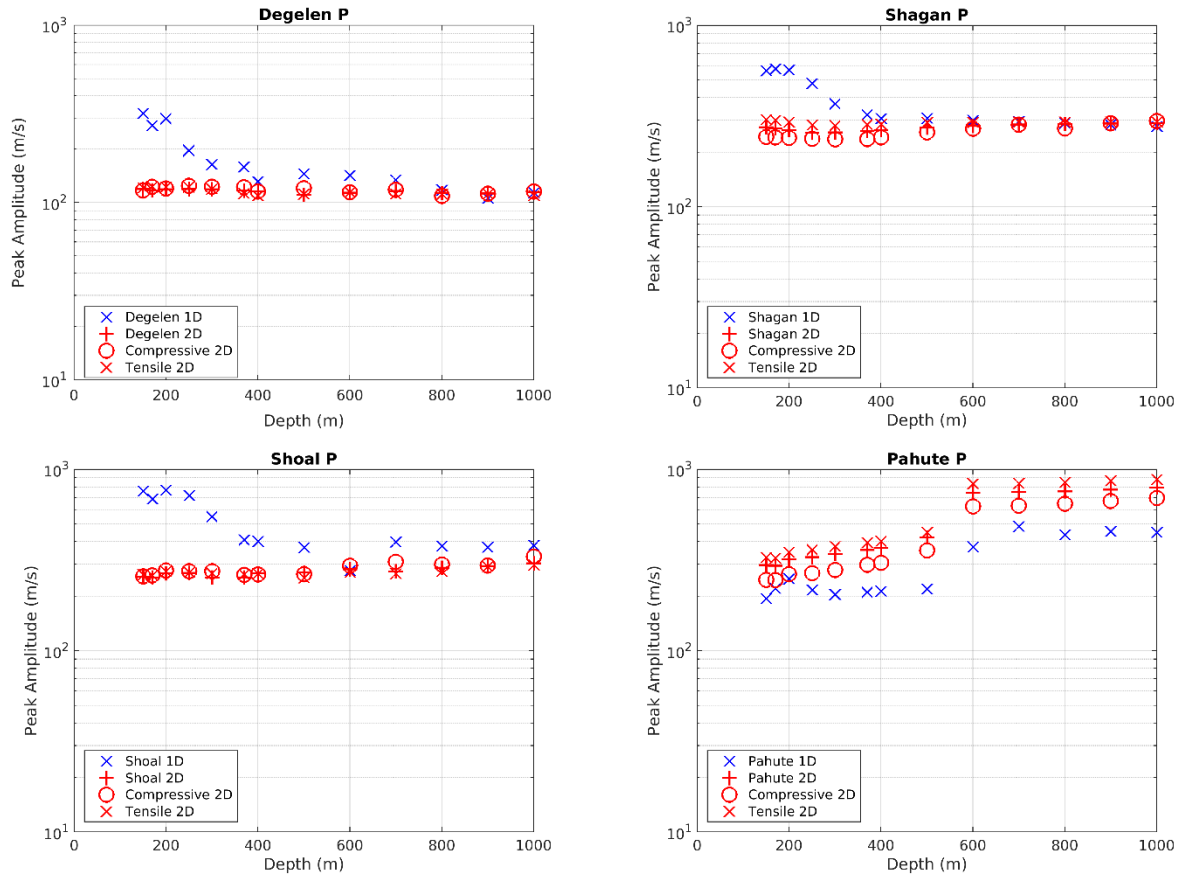


Figure 94. Far field P-wave amplitudes for each structure. *Blue points are the 1D calculation, Red points are the 2D axisymmetric calculations with and without tectonic release.*

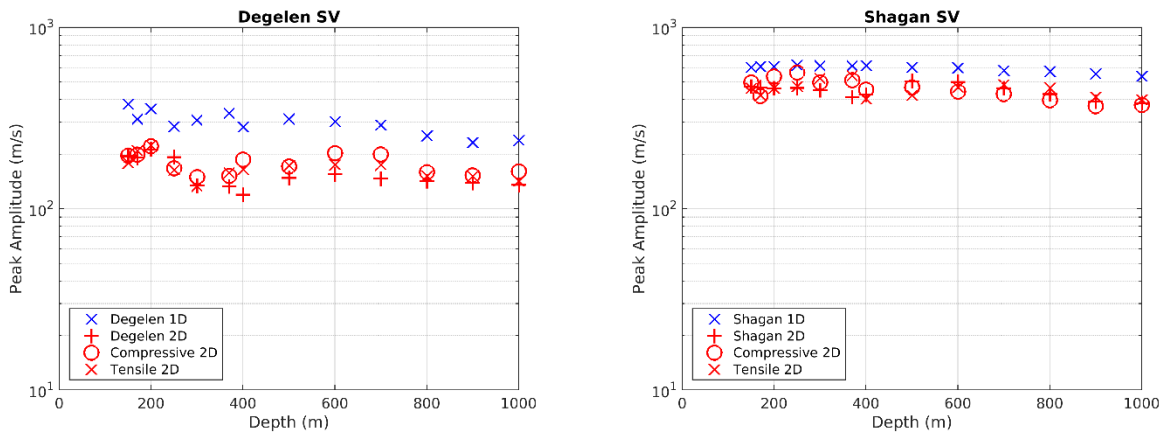


Figure 95. Far field SV-wave amplitudes for each structure. Blue points are the 1D calculation, Red points are the 2D axisymmetric calculations with and without tectonic release.

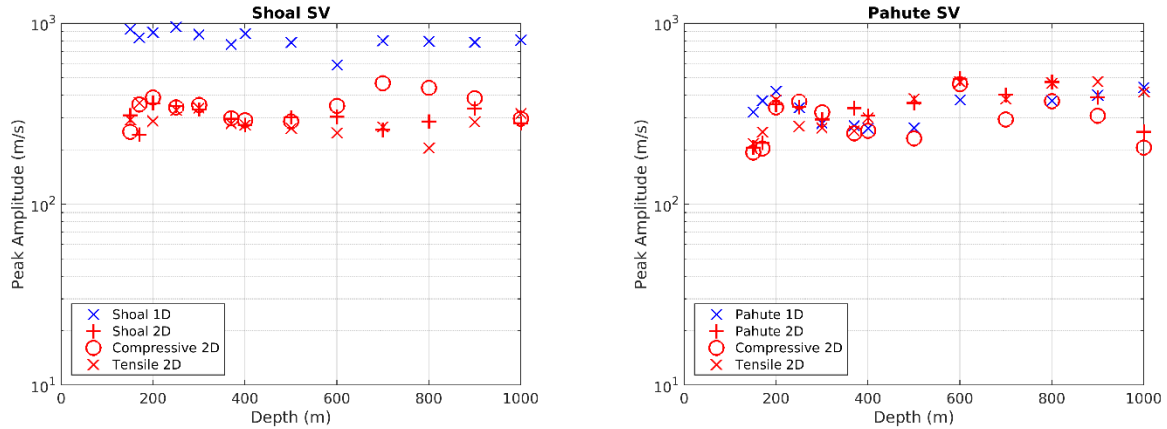


Figure 95 (continued). Far field SV-wave amplitudes for each structure. *Blue points are the 1D calculation, Red points are the 2D axisymmetric calculations with and without tectonic release.* The results described above change at lower frequencies as the direct P and pP destructively interfere at low frequencies. The effect of this is to reduce the P-wave amplitudes in the 1D calculations that increased at the higher frequencies, making the 1D and 2D amplitudes more consistent and almost independent of depth. Example waveforms are shown in Figure 96.

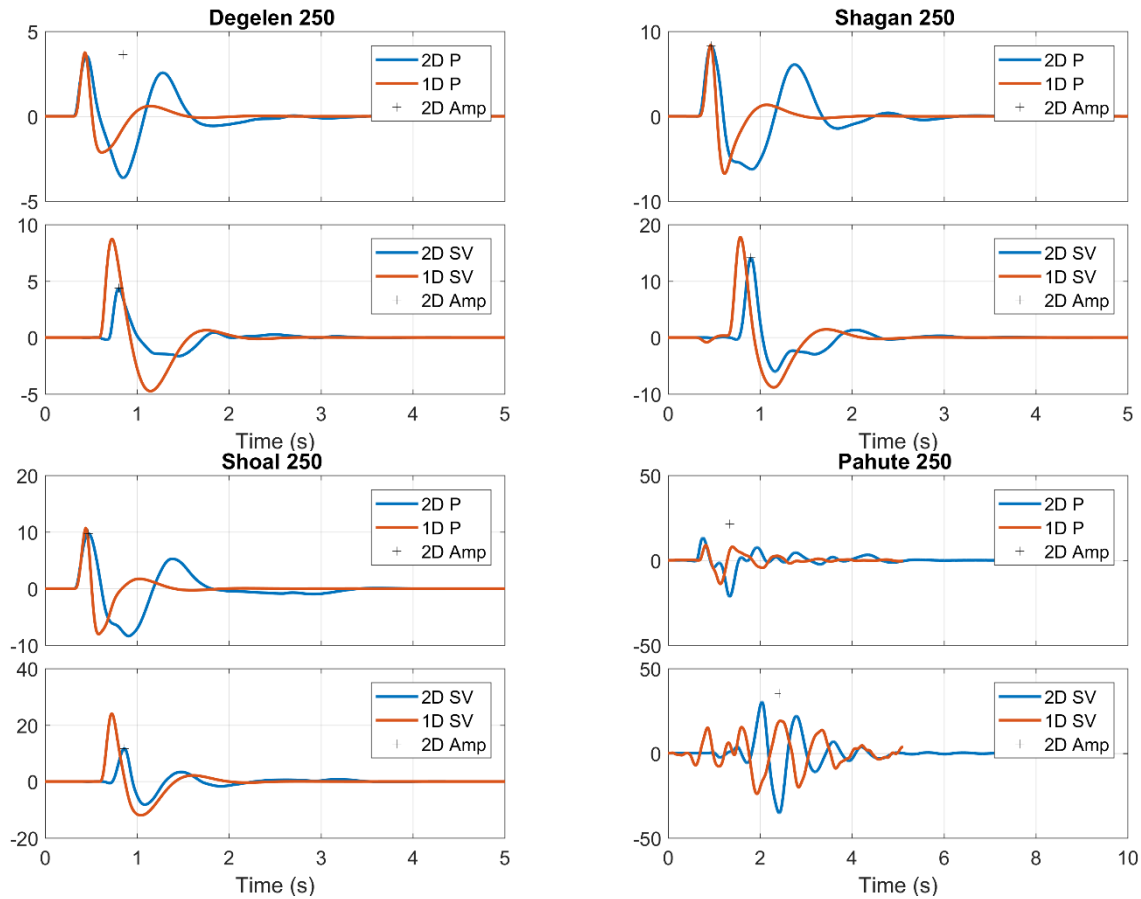


Figure 96. Same waveforms as Figure 93 lowpass filtered at 1 Hz.

Figure 97 and Figure 98 show the amplitude measurements for all P and SV waveforms filtered at 1 Hz for all depths, with and without tectonic stresses in the four structures

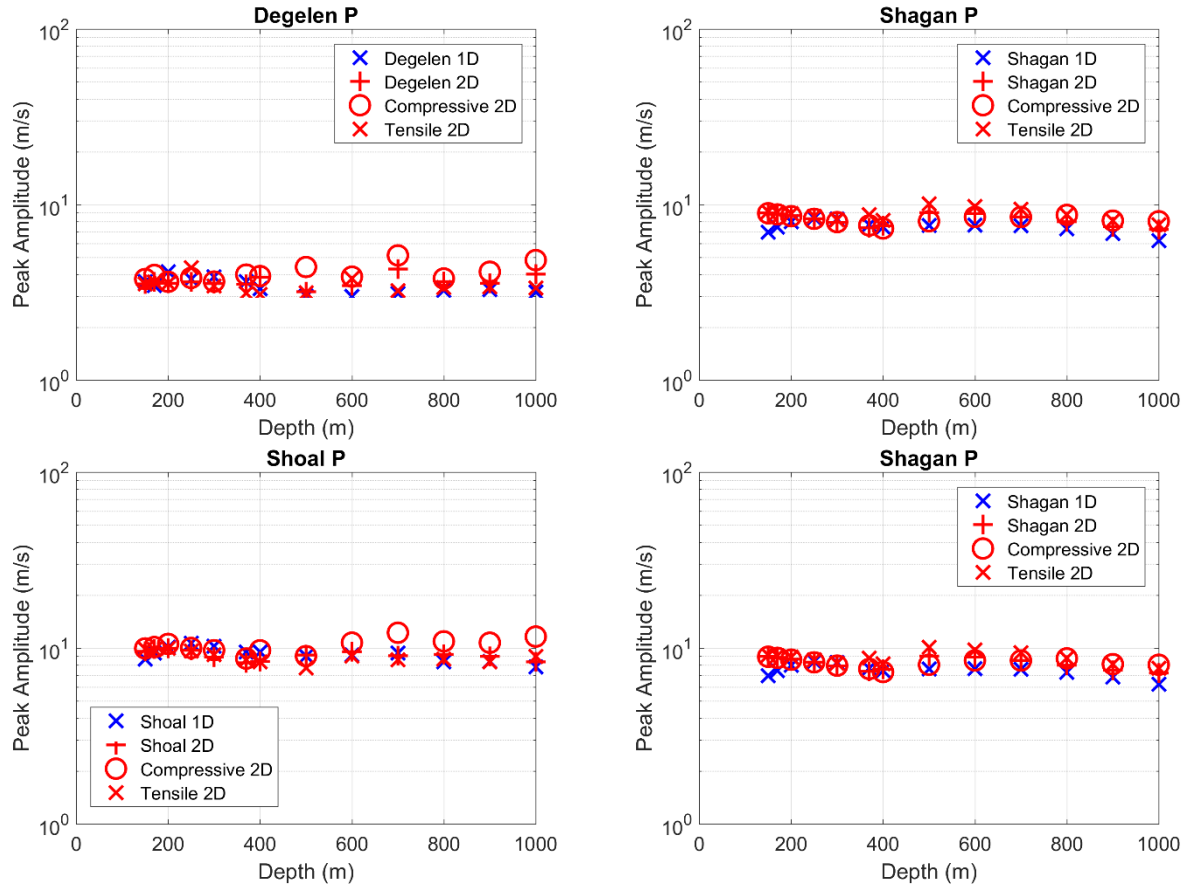


Figure 97. Far field P-wave amplitudes, low-pass filtered at 1 Hz, for each structure. *Blue points are the 1D calculation, Red points are the 2D axisymmetric calculations with and without tectonic release.*

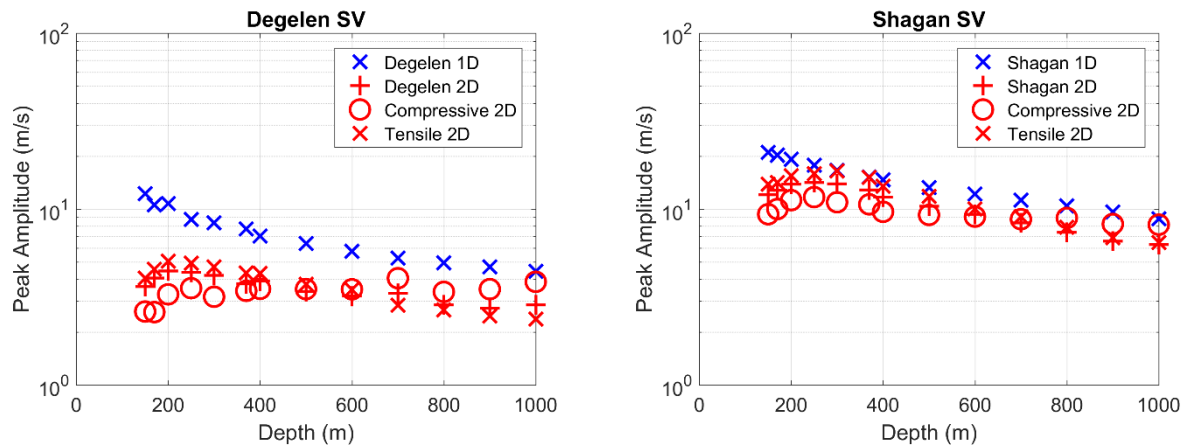


Figure 98. Far field SV-wave amplitudes, low-pass filtered at 1 Hz, for each structure. *Blue points are the 1D calculation, Red points are the 2D axisymmetric calculations with and without tectonic release.*

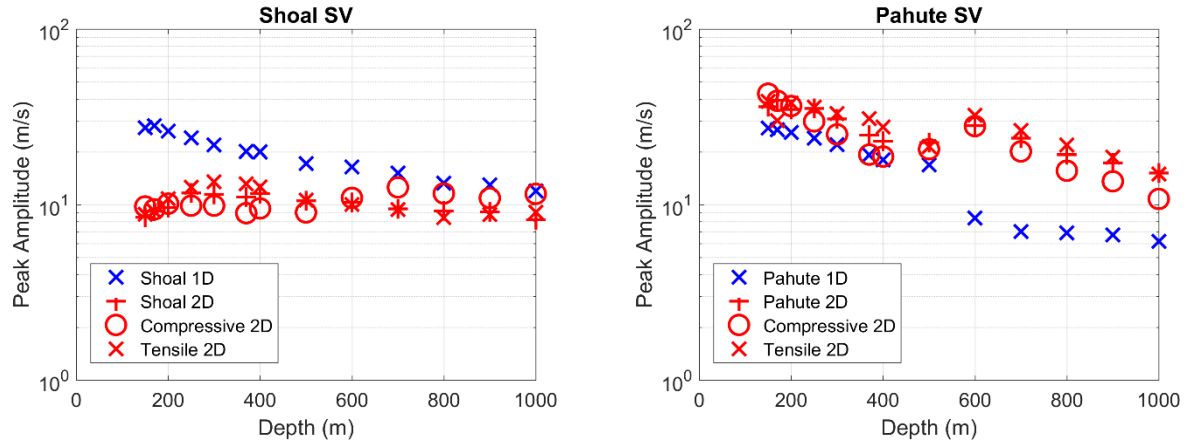


Figure 98 (continued). Far field SV-wave amplitudes, low-pass filtered at 1 Hz, for each structure. *Blue points are the 1D calculation, Red points are the 2D axisymmetric calculations with and without tectonic release.*

4.5.8 Conclusions from Seismic Source Decomposition Analysis

Figure 99 shows the M_s measurements from East Kazakh explosions and calculations of M_s with and without compressive and tensile tectonic release. The East Kazakh M_s values are in good agreement with the calculations, particularly with compressive tectonic release. The North Korean M_s values are still very high relative to the calculations, however, even for tensile tectonic release. Assuming the yields are correct for these events (they are estimates derived from P-waves), there are several possible explanations for this. As noted in the previous sections on 3D calculations with topography, there is an amplification effect for explosions near the base of a mountain, and the North Korean events all appear to be near the base of a mountain. Another possible explanation is underestimation of the effect of tectonic strain release. The tectonic stresses were derived from equilibrium with frictional sliding, however the granite strength model is stronger than frictional sliding, so accounting for frictional slip would increase the effect of tectonic release. Finally, as noted in Figure 100, a weaker granite model such as that used for modeling Shoal, generates larger surface waves than the stronger Degelen model.

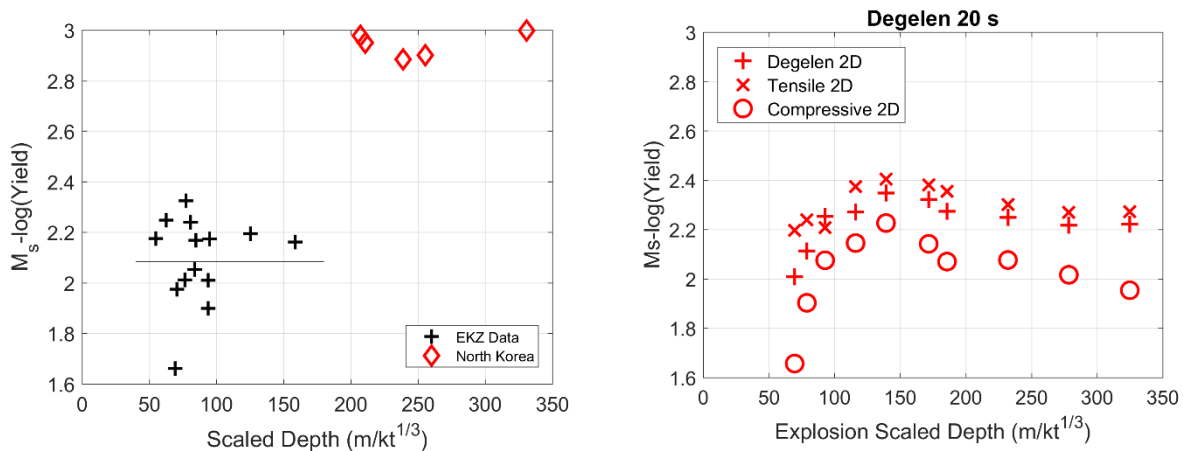


Figure 99. M_s -log(Yield) vs. scaled depth. Left: Measurements from East Kazakh and North Korean Data. Right: Calculations for Degelen structure.

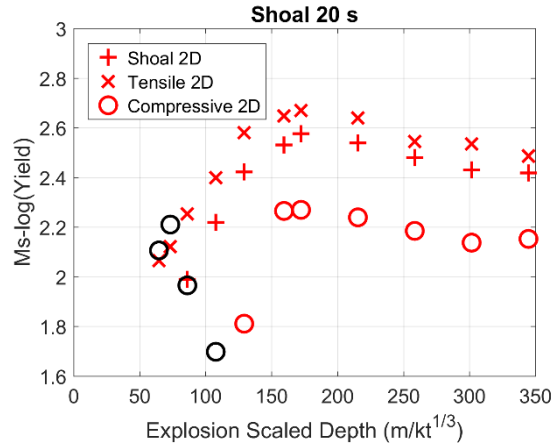


Figure 100. Calculations for Shoal structure. *Black circles indicate polarity-reversed Rayleigh waves.*

5. Improvements to CRAM3D Codes

Accelerated Equilibrium Calculation

The longest part of a CRAM3D simulation with topography is the computation of an equilibrium starting grid. There are two reasons for this. First, uncompensated topographic effects that are left for the simulation to resolve are large in space and mass, resulting in correspondingly large oscillatory grid motions that take proportionally longer to die out, up to several times more simulation time than for most of the energy from an explosion to exit or be absorbed by the grid. Second, numerical stability requires the size of simulation time steps to be proportional to the smallest separation between any two nodes in the grid. The nodes in the inner grid at the source cavity boundary are typically ~ 0.5 m apart, compared to $O(10\text{m})$ in the outer grid. In the first $1/10^{\text{th}}$ second of the explosion simulation, the cavity can grow by many times, separating those nodes laterally, and after the main shock has passed we can merge layers of zones around the cavity, thereby increasing the minimum node separation and speeding the rest of the simulation. Neither applies to establishing the equilibrium, where the cavity and grid must remain intact.

To speed the equilibrium computations, we have implemented the ability to compute and apply topographic overburden pressures that are in isostatic equilibrium. This is based on an axisymmetric solution for gravitational equilibrium beneath a sloping surface (Stevens et al, 1990) that also provides good equilibrium in 3D. In this solution, the topography above the base surface level (that of the plane-layer earth surrounding the grid) contributes only $1/3$ to the overburden pressure. The contributions are easily summed for the outer grid. The inner grid state is approximated by that of a full outer grid. As discussed earlier, we also break the equilibrium calculation into two parts, first with the inner grid replaced with outer grid zones so that we do not have the tiny zone problem discussed above, followed by a shorter calculation with the inner grid included.

In addition, we have improved the process by which motions are damped out during the equilibrium simulation. In the past, we have reduced grid velocity by a small factor at each time step, with the goal of short circuiting large grid oscillations that would otherwise result if starting with a large uncompensated topographic mass. But the schemes for selecting the damping have

been rudimentary and their performance not well characterized. We have adopted a new scheme wherein the net grid motion is calculated at each step and damping only applied when the grid is already slowing, i.e., the net acceleration is opposite the net velocity. We performed simulations with large uncompensated topographic loads and varied the damping factor to characterize the scheme. The results are illustrated in Figure 101. Each plots the maximum grid velocity with simulation time for a given value of the damping. The green curve is undamped, displaying grid oscillations that continue for many simulation seconds. In contrast, grid motion is down to an almost negligible level after only 2 seconds of simulation time with the additional damping.

With these improvements, we have reduced equilibrium simulation times by a factor of as much as 5. For runs that previously took several days to complete, this is a very significant change.

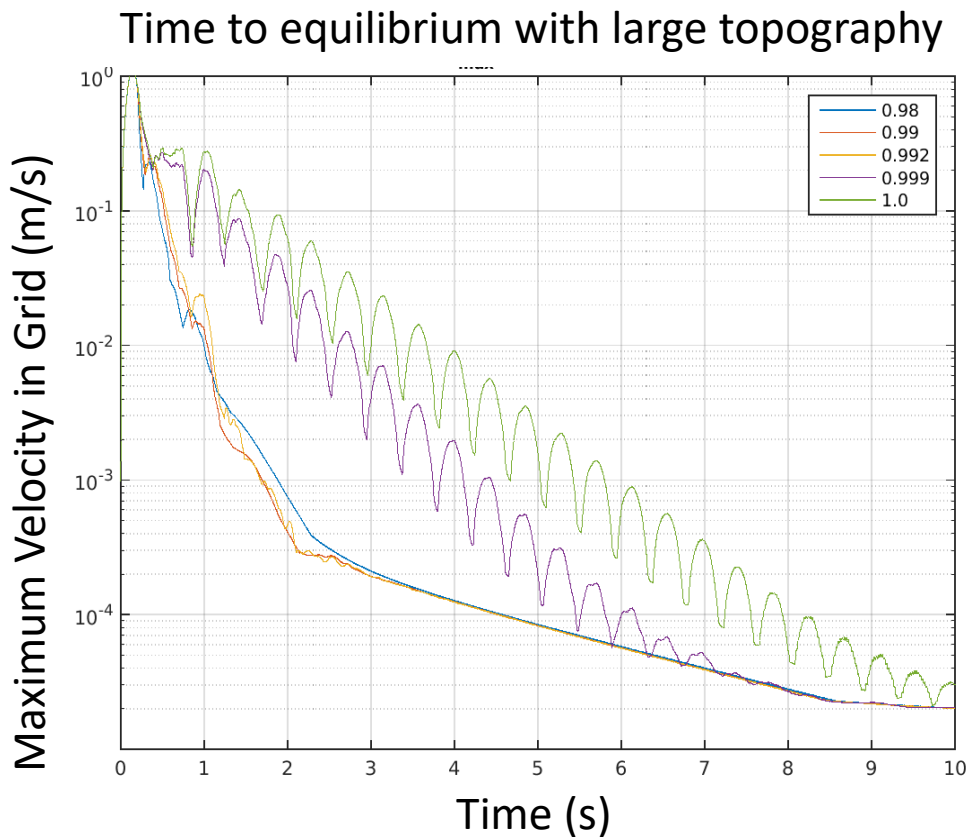


Figure 101. The effects of a dynamically varied damping in reducing simulation time for attaining grid equilibrium. *The green curve is undamped.*

6. Conclusions

We retrieved data from small Semipalatinsk (Shagan River and Degelen) explosions at Borovoye and measured M_s for events as small as 1.4 kilotons. We find that M_s :yield is very consistent with M_s measured from larger events, with a slope of 1.0, and very consistent with the global M_s :yield distribution curve (Stevens and Murphy, 2001), and they are very inconsistent with M_s vs. estimated yield for the three North Korean explosions, which lie almost a full magnitude unit above the Semipalatinsk curve. This shows that the high M_s of the North Korean explosions is not the result of a nonunity M_s :yield curve, and that there is something very different about generation of surface waves from the North Korean explosions and the Semipalatinsk explosions. We have previously hypothesized that this difference could be due to differences tectonic stress state and tectonic release by the explosions (Murphy et al, 2013), and this remains a likely explanation. We also find in this study an amplification of surface waves for explosions near the base of a mountain with steep topography.

We examined the effect of depth beneath a mountainside or other steep slope on seismic waves by performing three 3D nonlinear calculations of an explosion beneath a steep slope. The first, Slope 1, is placed beneath the mountain; the second, Slope 2, is higher and inside the mountain; while the third, Slope 3, is inside the mountain with the yield increased by a factor of 4. We then did four additional 3D calculations using the actual topography of the North Korean test site.

We find that generation of long period surface waves is strongly dependent on location relative to the slope. Long period surface waves are generated almost entirely by the static horizontal displacement in the upper few hundred meters below the surface. If the explosion is inside the mountain and close enough to the free surface that stress is relieved by the sides of the mountain, then subsurface horizontal displacement is reduced and surface wave amplitudes are reduced dramatically. However, for explosions that are near the base of the mountain, long period surface waves are increased in amplitude by as much as a factor of 2.

In contrast, regional P and S phases are slightly larger for the explosion in the mountain than beneath it, especially for paths that go across the mountain. Otherwise, there is little difference in regional phases between the flat (Shoal) and topographic (Slope 1 and Slope 2) calculations. The North Korean calculations show variability in regional P and S phase amplitudes as a function of azimuth and as a function of depth, however the average changes are small.

For the Slope calculations, far field P body waves are slightly enhanced by the presence of the mountain due to reduction of the pP interference. That is, the pP phase with the mountain present interferes less with the direct P than it does for a flat surface. For Slope 1 this occurs primarily for the cross-slope direction, while for Slope 2 it occurs in all directions. Far field SV body waves are reduced in amplitude relative to the flat case because the pS phase which is very strong for a flat surface is reduced in amplitude for the mountain. Far field SH waves which do not exist for the flat surface are comparable in amplitude to SV for the mountain cases. Results for the North Korea calculations are similar except that the P-wave amplitudes are more consistent and show minimal effect from either topography or source depth. SV waves are also more consistent than in the Slope calculations, probably because the NK mountain is larger than the mountain used in the Slope calculations and the surface variation occurs over a larger area.

In addition to the 3D calculations, we performed a large number of 2D axisymmetric calculations for four earth structures, with and without tectonic release and covering a range of depths from 150m to 1000m to examine the effects of depth, material properties and tectonic stress state. We find that P-waves are relatively insensitive to these effects because the initial downgoing P-wave is unaffected by interaction with the free surface. Surface waves, however, are strongly affected by all of these effects. Surface waves decrease in amplitude at shallow depths where there is strong interaction with the free surface, and they are decreased by compressive tectonic release. Surface waves are also decreased by increasing depth. Tensile tectonic stresses amplify surface waves, although the effect of compressive stresses to decrease surface waves is stronger. Surface waves are largest for explosions at or slightly below normal containment depth where the interaction with the free surface is moderate and the increasing pressure with depth does not reduce them. This effect is amplified by topography where surface waves from explosions within the mountain are reduced for the reasons explained earlier, and explosions near the base of the mountain are increased because the pressure and horizontal stress are less than at comparable depth in a region without topography. The North Korean events appear to be optimally located for surface waves: they are near the base of the mountain and in a region believed to have tensile tectonic stress. However, even under these optimum conditions, calculations do not produce surface waves quite as large as those observed. A possible explanation is underestimation of the effect of tectonic strain release. The tectonic stresses were derived from equilibrium with frictional sliding, however the granite strength model is stronger than frictional sliding, so accounting for frictional slip would increase the effect of tectonic release.

References

- Apsel, R. J. and J. E. Luco, (1983), "On the Green's Functions for a layered half-space, Part II," *Bull. Seismol. Soc. Am.*, 73, pp. 931-951.
- Bache, T. C. and D. G. Harkrider, (1976), "The body waves due to a general seismic source in a layered earth model," *Bull. Seismol. Soc. Am.*, 66, pp. 1805-1819.
- Bache, T. C., S. M. Day, and H. J. Swanger, (1982), "Rayleigh wave synthetic seismograms from multi-dimensional simulations of underground explosions," *Bull. Seismol. Soc. Am.*, 72, pp. 15-28.
- Day, S. M., N. Rimer, T. G. Barker, E. J. Halda, and B. Shkoller, (1986), "Numerical Study of Depth of Burial Effects on the Seismic Signature of Underground Explosions," S-Cubed Technical Report to the Defense Nuclear Agency, DNA-TR-86-114, March.
- Luco, J. E. and R. J. Apsel, (1983), "On the Green's Functions for a layered half-space, Part I," *Bull. Seismol. Soc. Am.*, 73, pp. 909-929.
- Masse, R. P., (1981), "Review of Seismic Source Models for Underground Nuclear Explosions," *Bull. Seism. Soc. Am.*, 71, pp. 1249-1268.
- Murphy, J. R., (1977), "Seismic Source Functions and Magnitude Determinations for Underground Nuclear Detonations," *Bull. Seism. Soc. Am.*, pp. 135-158.
- Murphy, J. R., (1995), "Types of seismic events and their source descriptions," in *Monitoring a Comprehensive Test Ban Treaty*, ed. E. Husebye and A. Dainty, Kluwer Academic Publishers, Boston, MA, pp. 225-245.
- Murphy, J. R., J. L. Stevens, B. C. Kohl, and T. J. Bennett, (2013), "Advanced seismic analyses of the source characteristics of the 2006 and 2009 North Korean nuclear tests," *Bull. Seism. Soc. Am.*, 103, No. 3, pp. 1640-1661, doi: 10.1785/0120120194.
- Patton, H. J. and S. R. Taylor, (2008), "Effects of shock-induced tensile failure on mb-Ms discrimination: Contrasts between historic nuclear explosions and the North Korean test of 9 October 2006," *Geophysical Research Letters*, **35**, L14301, doi:10.1029/2008GL034211.
- Patton, H. J., (2016), "A physical basis for Ms-yield scaling in hard rock and implications for late-time damage of the source medium," *Geophys. J. Int.*, **206**, pp. 191-204, Doi: 10.1093/gji/ggw140.
- Peyton, S., (1983), "A new representation for the failure surface of granular materials," S-Cubed Technical Report SSS-R-83-6051 submitted to DNA SPSS, March.
- Russell, D. R., (2006), "Development of a time-domain, variable period surface-wave magnitude measurement procedure for application at regional and teleseismic distances, part I: theory," *Bull. Seism. Soc. Am.*, 96, pp. 665-677, doi: 10.1785/0120050055.
- Stevens, J. L., T. G. Barker, E. J. Halda, J. R. Murphy, and N. Rimer, (1990), "Simulation of Teleseismic Body Waves from Underground Explosions Beneath Sloping and Flat Surfaces Using Nonlinear Axisymmetric Finite Difference Calculations," *Maxwell*

Technologies, Technical Report to Defense Nuclear Agency DNA-TR-91-5, December.

- Stevens, J. L., K. L. McLaughlin, B. Shkoller, and S. M. Day, (1993), "2-D axisymmetric calculations of surface waves generated by an explosion in an island, mountain, and sedimentary basin," *Geophysical Journal International*, v. 114, pp. 548-560.
- Stevens, J. L., N. Rimer, H. Xu, G. E. Baker, and S. M. Day, (2003), "Near field and regional modeling of explosions at the Degelen Test Site," DTRA-TR-03-3, SAIC-02/2050, SAIC, San Diego, CA, January.
- Stevens, J. L., D. A. Adams, G. E. Baker, M. G. Eneva, and H. Xu, (2005), "Improved Surface Wave Dispersion Models, Amplitude Measurements and Azimuth Estimates," DTRA01-01-C-0082, SAIC, San Diego, CA, March.
- Stevens, J. L., H. Xu, J. W. Given, and G. Eli Baker, (2008), "Development of surface wave dispersion and attenuation maps and improved methods for measuring surface waves," AFRL-RV-HA-TR-2008-1106, SAIC, San Diego, CA, May.
- Stevens, Jeffry L., Heming Xu, Michael O'Brien, Walter Nagy and Norton Rimer, (2011), Wave propagation from complex 3D sources using the representation theorem, AFRL-RV-HA-TR-2011-1019, SAIC, San Diego, CA, March.
- Stevens, J. L. and J. R. Murphy, (2001), "Yield Estimation from surface wave amplitudes," *Pure and Applied Geophysics*, 158, pp. 2227-2251, doi: 10.1007/PL00001147.
- Stevens, J. L. T. W. Thompson, and M. O'Brien, (2014), "Seismic Wave Generation and Propagation from Complex 3D Explosion Sources," AFRL-RV-PS-TR-2014-0084, Leidos, San Diego, CA, April.
- Stevens, J., L., M. O'Brien, H. Xu, and N. Rimer (2014a), "User Manual for the CRAM3D Finite Element Code, Version 2.0," Leidos-14/3002, Leidos, San Diego, CA, April.
- Stevens, J. L. and T. W. Thompson, (2015), "3D Numerical Modeling of Tectonic Strain Release from Explosions," *Bull. Seism. Soc. Am.*, 105, pp. 612-621, doi: 10.1785/0120140125.
- Zhang, M. and L. Wen, (2013), "High-precision location and yield of North Korea's 2013 nuclear test," *Geophysical Research Letters*, 40, pp. 1-6, doi:10.1002/grl.50607.
- Zoback, M. D., (2010), *Reservoir Mechanics*, Cambridge University Press, UK.

Appendix - CRAM3D Update and Deliverable

These are Release Notes for the Leidos 2017-05 release of source code for the CRAM3D and related programs under AFRL contract FA9453-14-C-0257

CHANGES:

CRAM3D

=====

1. Added Parameters:

iso_comp (switch)

A factor between 0 and 1 that specifies the degree to which the initial stresses account for the topography isostatically vs. material strength

2. Updated initial pressure calculation with isostatic topographic loading

- 1/3 weighted topo load in mu recursion
- axial stresses in outer/inner grid
- stresses in inner grid are not accurate with multiple materials
- also allows for dynamic compensation also

3. Improved damping scheme for equilibrium run

- application of damping based on $v_{avg} \cdot (dv/dt)_{avg}$ over grid

4. Improved process logging.

5. Saves zone masses to disk

6. cram_plot_dump

- adds ability to plot vertical stress, radial displacement, volumetric strain
- simplified usage
- fix for new colorbar behavior in R2015a
- replaces pcolor with surf in response to new behavior in R2015a
- fixes symbol plotting by replacing scatter with scatter3
- Improved exception handling in various of plotting routines.

INSTALLATION:

Untar dist.tar in an empty target directory and follow the build/test instructions in the README

List of Symbols, Abbreviations, and Acronyms

AFRL	Air Force Research Laboratory
AFSPC	Air Force Space Command
AFWA	Air Force Weather Agency
NPE	Non-proliferation Experiment
TOA	Take-off Angle

DISTRIBUTION LIST

DTIC/OCF	
8725 John J. Kingman Rd, Suite 0944	
Ft Belvoir, VA 22060-6218	1 cy
AFRL/RVIL	
Kirtland AFB, NM 87117-5776	2 cys
Official Record Copy	
AFRL/RVBYE/Dr. Frederick Schult	1 cy

This page is intentionally left blank.